Atomistic Spin Simulations of Heat Assisted Magnetic Recording Media

Răzvan-Vasile Ababei

Doctor of Philosophy

University of York
Physics

July 2019

Abstract

The continuous developing of magnetic recording requires to understand the physical properties of the magnetic media in detail in order to maximise the performance of this application. In this thesis, we investigated different paradigms of magnetic recording media by using atomistic spin dynamics model.

The inter-granular exchange is important for maintaining the stability of stored information in magnetic recording media. Therefore, we investigated the exchange coupling between neighbouring magnetic grains where magnetic impurity atoms are assumed to migrate into the non-magnetic grain boundary. Tri-layer and multi-grain system have been proposed to be studied where we found that a lower concentration of magnetic impurity reduces the inter-granular exchange coupling, respectively the exchange energy between the grains. Different angular dependence of the exchange energy is found for the multi-grain system compared to the tri-layer system, where an additional term of the exchange energy needs to be considered in order to describe the angular dependence.

Another problem of magnetic recording particularly to the heat-assisted magnetic recording is given by the design of the recording grains. Exchange-coupled composite media is found to give optimal performance due to low energy barrier at elevated temperature demonstrated energetically using Monte-Carlo simulations. Dynamic simulations show an acceleration of the switching due to spring effect being determined by several factors. One factor is the Gilbert damping which plays a significant role in magnetic reversal processes and determines the timescale of the switching. For a bilayer Fe/FePt medium we found an anomalous increase of the switching time with increasing soft layer damping constant. The reversal occurs via a high-temperature exchange spring, this phenomenon being delicately balanced in that the switching time increase occurs only in fields close to the coercivity.

Lastly, we investigated a new model of exchange interaction in $L1_0$ FePt following Ruderman-Kittel-Kasuya-Yosida function. An obvious similarity can be observed between first principle calculations of the exchange constant as a function of the distance between neighbours atoms and the function proposed by Ruderman-Kittel-Kasuya-Yosida which allows us to reproduce the magnetic properties of $L1_0$ FePt using the last mentioned function as first principle calculations require extremely long computational time.

Table of contents

List of figures **ix**

List of tables **xiii**

1 Introduction and motivation for research **1**

1.1 Brief History of Recording Media Evolution 1

1.2 Current Limitations of Magnetic Recording 3

1.3 Thesis Outline 5

2 Theory and Methods **9**

2.1 Basics of Magnetism 9

2.2 Extended Heisenberg Hamiltonian 12

2.2.1 Exchange Energy 13

2.2.2 Anisotropy Energy 15

2.2.3 Zeeman and magnetostatic energy 16

2.3 Atomistic Spin Model and Langevin Dynamics 16

2.3.1 Equation of Motion 18

2.3.2 Langevin dynamics. Noise mechanism 20

2.4 Implementation and integration methods 22

2.4.1 Heun and Semi-implicit scheme 23

2.4.2 Monte-Carlo and Constrained Monte-Carlo methods 28

2.5 Conclusion and further work 30

3 Investigation model of inter-granular exchange interaction **33**

3.1 Introduction 34

3.2 Heisenberg and biquadratic model of the exchange interaction. Theory of the intergranular exchange. 36

3.3 Tri-layer system 39

3.3.1 Model of the tri-layer system 39

3.3.2 Calculations of inter-granular exchange of tri-layer system 41
3.4 Multi-grain system simulations 45
3.4.1 Model of the hexagonal distribution of CoPt grains 45
3.4.2 Angular dependence of torque 46
3.4.3 Dependence of inter-granular exchange on separation, doping rate and temperature 48
3.5 Conclusions and further work 52

4 Atomistic simulations of exchange-coupled composite (ECC) media 55
4.1 Introduction 56
4.2 Atomistic properties of ECC media 58
4.2.1 Theoretical Fe/FePt bilayer model 58
4.2.2 Equilibrium properties of ECC media 60
4.3 Coercivity studies 69
4.3.1 Thermal reduction of the coercivity. 69
4.3.2 Dependence of the coercivity on thickness and interface coupling. Critical thickness. 74
4.4 Investigation of dynamical switching 76
4.4.1 Single particle switching and the Kikuchi law. 77
4.4.2 Switching mechanism of ECC media. 79
4.4.3 The impact of Gilbert damping on the reversal time. Conventional and high field regime. 80
4.5 Conclusions 85

5 RKKY model of exchange interaction in FePt 87
5.1 Exchange interaction models of FePt. 87
5.1.1 First principle calculations of exchange interactions in FePt 87
5.1.2 RKKY parametrization based on Mryasov model 90
5.2 Comparison of Tc distributions 92
5.3 RKKY finite size anisotropy scaling 99
5.4 Computational performance and new perspectives 103
5.5 Conclusions and further work 104

6 Conclusions and further work 107

Nomenclature 111

References 115

Appendix A Landau-Lifshitz-Gilbert equation 127

Appendix B The formalism of RKKY interaction 129

List of figures

1.1 Illustration of heat assisted magnetic recording (HAMR) 3
1.2 The road map of magnetic recording 4
1.3 Illustration of *quadrilemma* of heat-assisted magnetic recording 5

2.1 Hydrogen atom 10
2.2 Schematic representation of the hysteresis loop 11
2.3 Schematic representation of multi-scale calculation methods. 17
2.4 Schematic representation of LLG equation 19
2.5 The dependence of time step on mean magnetization for different reduced temperatures for the Heun integration scheme[1] 25
2.6 The dependence of time step on mean magnetisation for different reduced temperatures for the semi-implicit integration scheme 27
2.7 Schematic illustration of the three types of trial moves: (a) spin flip; (b) Gaussian and (c) random [1] 29

3.1 Experimental measurements of the coupling exchange energy as a function of thickness of the doping layer [2]. 35
3.2 Schematic represention of the cross section for two semi-infinite ferromagnets F1 and F2 with unit moments $\mathbf{m}_1$ and $\mathbf{m}_2$ separated by a non-magnetic spacer of thickness w. 38
3.3 A visualisation of the bilayer system made of two identical ferromagnets separated by a dilute oxide layer with a doping concentration of 25% of impurity atoms in this case. The width and height of each ferromagnet are 5 nm. 39
3.4 Calculated restoring torque as a function of the angle between magnetic layers for different inter-layer thicknesses. 42

3.5 The profile of magnetisation for bi-layer system during the switching of top layer for two different separation layer (a) 0.25nm and (b) 2.25nm with doping concentration of 30% 43
3.6 Calculated exchange coupling energy dependence on the inter-layer thickness for a doping constant of 30% at 100 K 44
3.7 Visualization of the hexagonal distribution of the grains for an inter-layer doping density of 30% with periodic boundary conditions on **z**-direction. . . 45
3.8 Schematic illustration of a typical rotation process of the central grain . . . 46
3.9 The angular dependence of the torque acting on the central grain for three different separations of the inter-layer (a) 0.50nm, (b) 0.75 nm, and (c) 1.00nm respectively for a doping density of 20%. 48
3.10 The temperature dependence of the effective inter-granular exchange constant for three different thickness of the interlayer (a) 0.50m, (b) 0.75nm, and (c) 1.00nm a low density. 50
3.11 The dependence of the effective exchange energy as a function of inter-layer thickness for anysotropy and non-aisotropy case at 300K 51
3.12 The angular dependence of free energy (a) and the torque(b) when the central grain has neighbours constrained with $m_z = +1$ and 3 neighbours with $m_z = -1$ 52
3.13 A visualisation of a complex structure of 5 ECC grains coupled by a non-magnetic layer with a doping density of 15% 53

4.1 3D illustration of ECC media 60
4.2 $M(T)$ curve for Fe using Kuz'min and classical fit expression [3] 62
4.3 Curie temperature of Fe and FePt within ECC media 63
4.4 Simulated torque energy curve of ECC media performed with constrained Monte-Carlo methods in reversal fields for different temperatures 65
4.5 The layer-resolved magnetisation of ECC media during the rotation within CMC simulation 66
4.6 The simulated free energy curves of ECC media in reversal magnetic fields at different temperatures. 68
4.7 The dependence of the energy barrier on the strength of the reversal field for ECC media at 50 K 70
4.8 The simulated temperature dependence of the coercivity for ECC media for an interface exchange $J_{\text{int}} = 1.5 \times 10^{-21}$ J. 72
4.9 The layer-solved magnetisation of ECC media during the hysteresis loop for (a) 0 K, (b) 300 K, and (c) 500 K 73

4.10 The dependence of coercive field on Fe thickness of ECC media for an exchange coupling constant at the interface $J_{\mathrm{int}} = 3 \times 10^{-21}$ J 75

4.11 Coercivity-temperature dependent of 10nm height ECC media for different exchange coupling values at the interface. 77

4.12 Switching mechanism for a range of damping values of Fe particle at zero Kelvin with an reversal field of 0.5 T. 78

4.13 The reversal mechanism of ECC media for different damping constants at different exchange coupling values at the interface on a reversal magnetic field of 1 T 81

4.14 The profile of magnetisation during the reversal mechanism of ECC media for two different values of exchange coupling at the interface and damping constant of Fe 82

4.15 Reversal time as a function of damping. Graph (a) shows the dependence for two different exchange coupling at the interface where graph (b) shows the dependence of reversal time for different values of the reversal field 83

4.16 The dependence of reversal time as a function of Fe thickness at different values of Fe damping in a reversal field of 3 T 84

5.1 Models of crystal structure of FePt. Image (a) shows a FCC structure which corresponds to $L1_0$ phase and image (b) shows a simplified model used by Mryasov *et al.* 88

5.2 The RKKY fit of Mryasov *ab initio* data. The extracted fermi vector is $k_f = 0.98\,\mathrm{nm}^{-1}$ 92

5.3 M(T) curves for different values of Fermi wave vector k_f of 10 nm height FePt cylinder using RKKY function and first principle claculation data. . . 94

5.4 M(T) curves for different radii of cut-off for 10 nm height FePt cylinder using RKKY function and first principle calculation data. 95

5.5 M(T) curves for different truncations and radii of the 10 nm height FePt cylinder using Mryasov values for the exchange interaction list 96

5.6 Magnetisation as a function of temperature for different diameters of FePt cylinder and different cut-off ranges using RKKY model of exchange. . . . 97

5.7 The size distribution of Curie temperature for different ranges of cut-off. The solid lines stands for the fitting using equation (5.12). Graph (a) shows the size distribution using DFT-based Hamiltonian , respectively graph (b) corresponds to RKKY model. 98

5.8 Plot of the free energy curves for a 10 nm height FePt cylinder as a function of the polar angle θ for two different cases of exchange interaction: (a) DFT data and (b) RKKY function 101
5.9 Typical snapshots of the spins configuration during the switching mechanism at different polar angles θ for a cylindrical grain of FePt with 10nm height and 10nm basal diameter at a temperature of 200K. 102
5.10 The calculated temperature dependence of $L1_0$ FePt in log-log plot of the reduced anisotropy and magnetisation using RKKY function for two cases: single ion contribution and tow-ion contribution 103
5.11 Scaling exponent of anisotropy as a function of diameter of the $L1_0$ FePt cylinder using RKKY function with two-ion contribution 104
5.12 Runtime for different ranges of RKKY function as a function of number of atoms. The time has been measured for each simulation which perform 100000 Monte-Carlo steps at each system size. 105

List of tables

2.1 Table of constants 23

3.1 Atomistic parameters used for the bilayer system which correspond to CoPt alloy. 40

4.1 Atomistic parameters of Fe and FePt in both cases isolated and interacting through the J_{ij} interface. 59

5.1 The bulk T_C and critical exponent ν for both model at different ranges of cut-off. The values have been obtained by fitting the graphs from figure 5.7 using equation (5.10) 98

Acknowledgements

First of all, I wish to acknowledge my supervisors Professor Roy W. Chantrell and Doctor Richard F. L. Evans for their continuous support and guidance over the past four years of my Ph.D. without whom this thesis would not be possible. I would also like to thank my former supervisor Professor Alexandru Stancu for introducing me in this fascinating world of magnetism. Besides this, I want to dedicate special thanks to my friend and colleague, Matt Ellis, for the fruitful collaboration.

I want to express my gratitude to my colleagues: Sergiu Ruta, Sam Westmoreland, Andrea Meo, Sarah Jenkins, Lewis Atkinson, Mara Strungaru, Roberto Moreno, Daniel Meilak, Ewan Rannala, Luke Elliot. Besides this, I am thankful to my table tennis friends from York who made my time more enjoyable succeeding to win many medals and trophies in team and individual competitions. Particular thanks to my sparring partners Ben Lockyer, Ryan Hood, Tom Thorp, Adam Exley, Arthur Sorley, Dave Smith, Feng Yankui, Jack Taylor, and Jack Kelly.

Nevertheless, I would like to thank my parents and my sister for their love, constant support and encouragement. Lastly, I am grateful to Advanced Storage Technology Consortium (ASTC) for the funding of my project.

Declaration

I hereby declare that the work presented in this thesis is my own work, except for the previous acknowledged contributions. This work has not previously been submitted or presented for an award at this, or any other, University. The calculations have been done by the author using the atomistic spin dynamics software package VAMPIRE, developed by my supervisor Dr. Richard F. L. Evans.

This thesis contains results presented at various conferences by the author and is based on two published articles in collaboration with others as follows:

- Razvan-V. Ababei, Matthew O. A. Ellis, Richard F. L. Evans, and Roy W. Chantrell, "Anomalous damping dependence of the switching time in Fe/FePt bilayer recording media", Phys. Rev. B **99**, 024427

- Matthew O. A. Ellis, Razvan-V. Ababei, Roger Wood, Richard F. L. Evans, and Roy W. Chantrell, "Manifestation of higher-order inter-granular exchange in magnetic recording media", Appl. Phys. Lett. **111**, 082405 (2017);

Răzvan-Vasile Ababei
July 2019

În memoria înaintaşilor ale căror idei nu au rămas să se sleiască ...

Chapter 1

Introduction and motivation for research

1.1 Brief History of Recording Media Evolution

Magnetism is a fascinating branch of science and has a long history. First magnetic materials were discovered in 6th century BC near to the ancient city Magnesia, Greece [4][5]. Nowadays, we cannot imagine the progress of technology without the applications of the magnetism, having a wide range of applications in industry. One of these applications is represented by magnetic recording [6] whose purpose is to store information on magnetic materials such as ferromagnetic materials. The first theoretical studies done on magnetic recording belong to Oberlin Smith in 1888 [7] and ten years later this idea was applied for the first Telegraphone [8], the first recording device based on a magnetic memory.

Magnetic recording has been developed significantly in the last decades, massive research has been done to increase the performance of this application. However, there are significant physical limitations of this application once the grain sizes must be reduced in order to achieve a great areal density, the main challenge being to overcome the three physical limitations of recording media comprised in the *trilemma* of magnetic recording [9]. These three limitations are related to increasing the areal density of data, which implies a decrease in the grain volume whilst maintaining good thermal stability. High anisotropy materials are needed for recording media, in order to ensure the thermal stability since the rate of magnetisation decay is given by the Arrhenius-Néel law: $\tau = \tau_0 \exp(K_u V/k_B T)$, where K_u is the anisotropy energy, V is the volume, k_B is the Boltzmann constant, and T is the temperature. If the exponential factor is greater than 60, the storage time is estimated at 10 years[10]. Therefore, reducing the sizes of the grains will affect thermal stability. Consequently, small grains must have high uniaxial anisotropy, determining a more difficult writing process as the writing field increases with decreasing the sizes according to Sharrock equation [11, 12]: $H_{\mathrm{wr}}(t) = H_k \left\{1 - \left[\frac{k_B T}{K_u V} \ln\left(\frac{f_0 t}{\ln 2}\right)\right]^n\right\}$, where H_k is the anisotropy field, f_0 is the attempt frequency of the material, and n is the shifting exponent. Many techniques and magnetic materials have been tested and huge progress also has been achieved[13], the limit of the areal density being estimated around $1\,\mathrm{Tb/in^2}$ [14] for PMR at that time.

One of the first methods for recording media was longitudinal recording where the media is magnetised parallelly to the plane. It confers a high areal density (AD) and a good signal to noise ratio (SNR) as long the layers have high anisotropy, and lower thickness [15]. In order to minimize the demagnetisation effects and stray fields with respect to increasing the AD, the longitudinal recording was replaced by perpendicular recording, polarising the bits in the perpendicular plane. Here, the bits can be parallel or anti-parallel oriented representing in binary system 1, respectively 0 [16]. A remarkable improvement of PMR was the introduction of a soft underlayer underneath the recording layer, which generates larger write fields.

One of the most promising technologies to solve the *trilemma* of magnetic recording is heat assisted magnetic recording (HAMR) [17, 18], allowing a decrease in the anisotropy by heating the bit to the Curie temperature. In this way, the *writability* problem has been solved by temporary decrease of the coercivity allowing to write information with a conventional magnetic field up to 1 T which is the maximum that can be achieved with the current technology of an electromagnet embedded into a writing head. After the cooling, the anisotropy is restored back to the ambient temperature value, maintaining long-term stability. Here, the heating can be performed with a localised laser pulse having two different approaches such as pulsed spot and continuous spot [19]. Both methods use a laser for heating, positioned before the writing coil as shown in figure 1.1 allowing to heat prior to applying the field.

An improvement of recording techniques can alternatively be done with microwave-assisted magnetic recording (MAMR) which was proposed by Zhu *et al.*[21] representing a feasible technology for magnetic recording. This technique utilises ferromagnetic resonance in order to induce a precessional switching of the magnetisation which is predicted to be achieved at lower fields without involving heat. Besides the switching field applied along easy axis, an alternating field is applied orthogonally to the easy axis in order to trigger the precession reducing the coercivity of the grains. In theory, MAMR can achieve a large AD being in competition with HAMR.

In both techniques, the architecture of the recording medium matters. To increase the AD, bit patterned media (BPM)[22–24] was proposed to replace the traditional recording medium where the area necessary for a single bit can be drastically reduced. In BPM, a single bit is stored on a single nano-dot whose area is much lower than in the continuous media where a group of grains create a single bit. Prior to improving the AD in BPM, several lithography

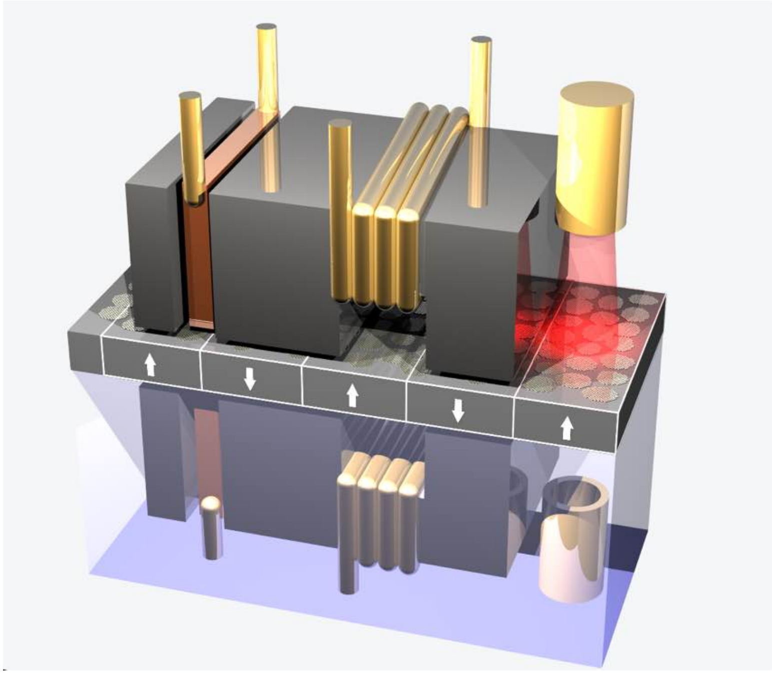

Fig. 1.1 Illustration of heat assisted magnetic recording process. This image is taken from reference [20]

methods are tested[25]. Here, electron beam (EB) lithography is found suitable to reduce the spacing between islands [26] due to self-assembling effect of block copolymer. In reference [27] is shown that BPM can support an AD of $5\,\mathrm{Tb/in^2}$ if the dispersion is highly controlled excluding the thermal effects. Despite this promising AD, there are many challenges to implement this technique. The manufacturing and utilization of patterned media disk drives require a new understanding of science at the nano-scale level and offer exciting opportunities to explore this nano-scale world.

1.2 Current Limitations of Magnetic Recording

The HAMR technique reaches high performance in terms of reducing the sizes of the grains, being able to move the limit beyond $1\,\mathrm{Tb/in^2}$ as shown in figure 1.2. So far, HAMR is a very promising technology for the next generation of hard-disk drives (HDD) being able to push the AD beyond $5\,\mathrm{Tb/in^2}$. To do that, this technique must solve the *trilemma* of recording media where the decreasing of the grain volume requires an increase in the anisotropy constant K for thermal stability and also sufficient fields are required to achieve the *writability* problem. Besides these three requirements, Evans and his co-workers [28] showed that HAMR comes with an additional problem. This is related to the thermal errors

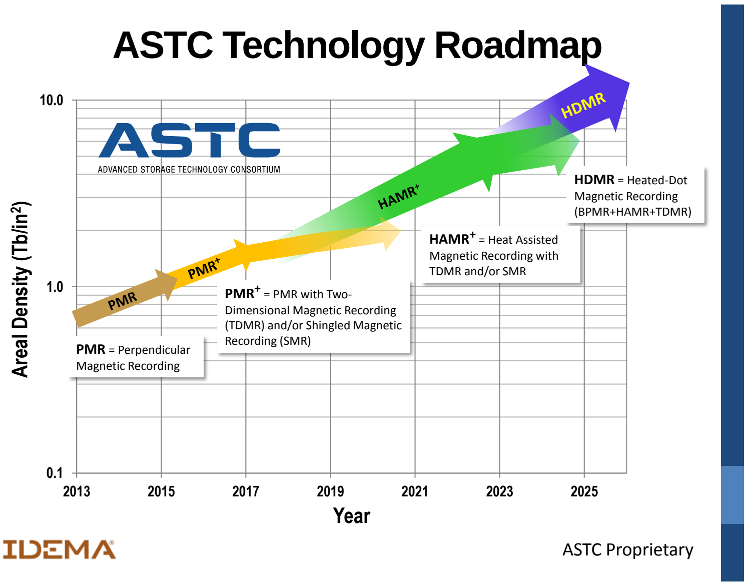

Fig. 1.2 The road-map of recording media. This picture has been taken from *www.idema.org*

which occur due to the heating in the HAMR process. Evans *et al.*[28] showed a strong dependence of the error rates with the temperature. Although the writing field is greater than coercivity, this is not sufficient to ensure the switching due to thermal fluctuation which affect the writing process. In reference [28] this problem is shown the rate of errors depends on the temperature following bit error rate (BER), defined as:

$$\mathrm{BER} = \exp\left(-\frac{2\mu_0 V M_s H_{\mathrm{wr}}}{k_B T}\right), \tag{1.1}$$

where μ_0 is the magnetic permeability of free space, M_s is the saturation magnetisation. Hence, the solution for this is to use high M_s materials which ensure the thermal writability. Therefore, the problem becomes dependent on four aspects called *quadrilemma* of magnetic recording, shown schematically in figure 1.3.

As shown in the road map figure 1.2, the highest performance of magnetic recording that can be achieved in the next years can be a combination of HAMR with BPM. To do that we need an innovative design of the magnetic grains capable to achieve the above-mentioned problem, the *quadrilemma* of magnetic recording. Multiple designs of the grains have been tested such as coupled granular continuous (CGC) [29] but the performance of this design has been demonstrated as being poor, especially for HAMR where the writing field is not sufficient to ensure a stable switching.

Another design was proposed by Zhou *et al.* [30] where the grains are supposed to be aligned with an angle of 45 degrees. In this way, the switching field can be lowered to half of

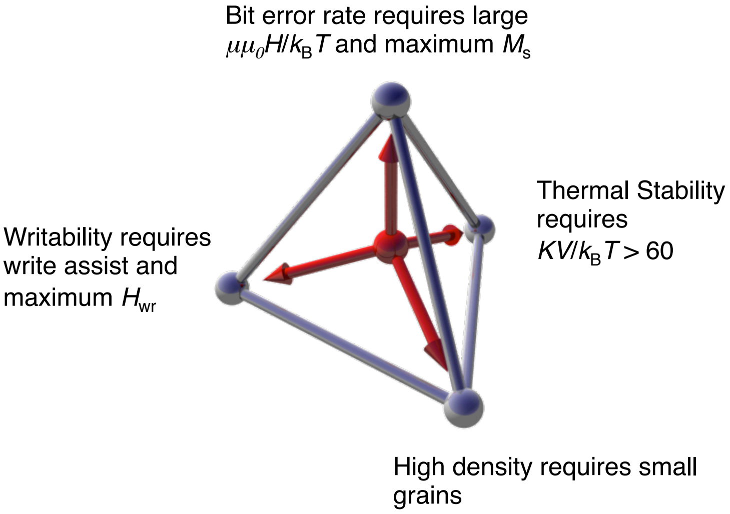
Bit error rate requires large $\mu\mu_0 H/k_B T$ and maximum M_s
Thermal Stability requires $KV/k_B T > 60$
Writability requires write assist and maximum H_{wr}
High density requires small grains

Fig. 1.3 Illustration of *quadrilemma* of heat-assisted magnetic recording. This picture has been taken from reference [28].

the anisotropy field. However, these recording films are very hard to be manufactured for HAMR.

Ultimately, in order to reduce the thermal errors, Suess and Schrefl [31] proposed an innovative design for recording media. This is a combination of two different materials such as soft and hard phase with different Curie temperatures. This design is known as exchange coupled composite (ECC) and it presents considerable advantages over conventional recording media like high uniaxial anisotropy, small sizes of the grains, lower switching field and good performance for HAMR.

In any method presented in this chapter, large M_s and high anisotropic materials are required for magnetic recording. Weller *et al.* summarized the main candidates for magnetic recording in reference [32]. A promising solution is CoPt alloy whose magnetic properties are well balanced with the anisotropy of $2 \times 10^7\,\mathrm{erg/cm^3}$ which is the equivalent of $2 \times 10^6\,\mathrm{J/m^3}$ and a saturation magnetisation of $1100\,\mathrm{emu/cm^3}$ the equivalent of $1100\,\mathrm{kA/m}$ but the most highly anisotropy material is $\mathrm{L1_0}$ FePt alloy whose anisotropy varies between $6.6 \times 10^6\,\mathrm{J/m^3}$ - $1 \times 10^7\,\mathrm{J/m^3}$. This makes FePt one of the most attractive material for recording media getting considerable attention of research[33, 34].

1.3 Thesis Outline

In this thesis we investigated a series of problems related to magnetic recording which gives more insight about reversal mechanisms in magnetic recording. We simulated the switching mechanism at the atomistic scale by employing atomistic spin dynamics (ASD). We investigated three different problems of the reversal mechanism where the exchange interaction plays a crucial role and having different forms depending on the grain sizes and material properties.

In the introduction, we presented the main problems of magnetic recording and the current status of research. The second chapter details the theory and the model used for simulations throughout this thesis. The atomistic spin dynamics (ASD) model and Langevin dynamics are discussed in detail to show the mathematical support of this model. This chapter ends-up with the section of implementation methods where two schemes of numerical integration for Landau-Lifshitz-Gilbert equation have been proposed and a brief presentation is given of Monte-Carlo (MC) and Constrained Monte-Carlo (CMC) algorithms.

The third chapter describes calculations of the exchange interaction between nano-grains being calculated via the CMC method. Two different cases have been analyzed: a system of two ferromagnets separated by an isolating layer and a granular system comprising seven grains distributed into a hexagon, each grain being separated by a non-magnetic layer with magnetic impurities. We study the dependence of inter-granular exchange energy as a function of temperature, separation and doping density by computing the torque of the switching grain.

The fourth chapter presents some investigations done on ECC media. The chapter starts with an introduction where we motivate the utility of this innovative design of the magnetic grains towards HAMR. A fundamental property, the energy barrier is calculated for different temperatures and magnetic fields using the CMC method in order to find out whether this system confers long-term stability. This chapter is continued by dynamical simulations, where the dependence of the coercive field is determined for different temperatures, thicknesses, and interface exchange coupling constants. In the final part of this chapter some simulations related to the switching speed depending on the damping constant of the soft phase at higher and conventional fields are presented.

The fifth chapter is related to a new model of exchange interaction in $L1_0$ FePt based on an oscillatory dependence of the exchange constant on distance similarly to Ruderman-Kittel-Kasuya-Yosida (RKKY) function. In this chapter, we present some comparisons of the Curie temperature distributions between *ab-initio* calculations for exchange and RKKY mechanism for different radii of interactions and sizes of the particles. In addition to this, RKKY proved to reproduce the scaling of anisotropy with temperature according to experimental results. The chapter ends with some scalability tests for different ranges of truncations showing a speed-up of the calculations for a specific range with respect to the physical properties of the $L1_0$ FePt material.

The last chapter summarizes the conclusions of this chapter and the future work that can be done to extend this research. This is followed by a full list of references and two appendices.

Chapter 2

Theory and Methods

2.1 Basics of Magnetism

In the classical theory of electromagnetism, the magnetic field is an effect of a current loop which denotes electrical charge in motion. It can be observed that a distribution of the electrical currents produce a magnetic field which at large distance from the source can be considered a dipolar field. In atoms, the motion of electrons gives rise to a magnetic moment of the atom. Starting with the classical model of the Hidrogen atom, Bohr calculated the magnetic moment of the electron, known in literature as the Bohr magneton, μ_B, assuming that the electron with an elementary electric charge $-e$ has a circular motion around the hydrogen nucleus as shown in figure 2.1. By equating the magnitude of the angular momentum of the electron with the magnetic moment we obtain [35]:

$$\mu_B = \frac{e\hbar}{2m_e} = 9.274 \times 10^{-24}\,\mathrm{J/T}, \tag{2.1}$$

where $\hbar$ is the reduced Planck constant, and m_e is the mass of the electron. Besides the circular motion around the nucleus, the electron has its own intrinsic rotation, called spin $\mathbf{S}$ which gives a magnetic moment of the electron as:

$$\mu = -g\frac{\mu_B(\mathbf{L}+\mathbf{S})}{\hbar}, \tag{2.2}$$

where g is the Landé factor, $\mathbf{L}$ is the orbital momentum and $\mathbf{S}$ is the spin. In more complicated isolated atoms with more electrons, the magnetic moment is given by the unpaired electrons. These unpaired electrons come as a result of different quantum states of the electrons which have a specific order given by the Hund's rule[35].

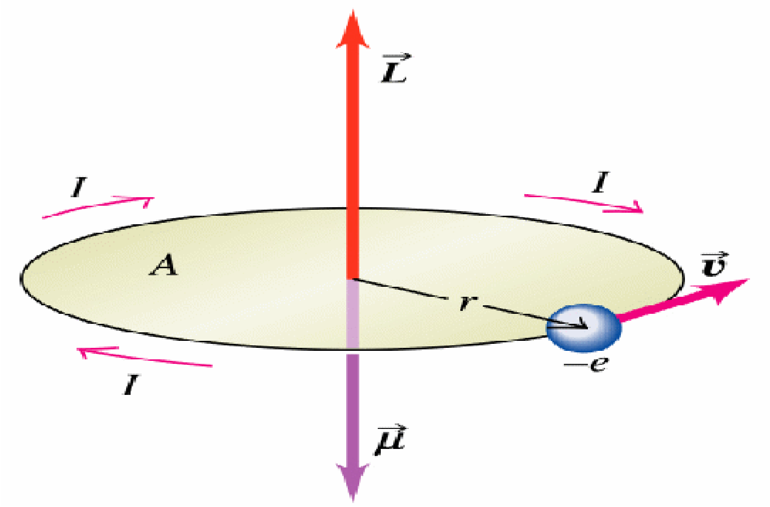

Fig. 2.1 The electron orbiting around a hydrogen nucleus with the radius r and angular velocity v.

The macroscopic characterization of a magnetic material is given by the magnetisation, **M** representing a summation of the atomic magnetic moments per unit volume. The effect of the magnetisation is visible in the presence of a magnetic field, **H** which in many materials varies linearly with the magnetic field as:

$$\mathbf{M} = \chi \mathbf{H}, \tag{2.3}$$

where χ is called magnetic susceptibility of the material. As a function of the magnetic susceptibility, the magnetic materials can be classified as "paramagnetic" if $\chi > 0$, and "diamagnetic" materials if $\chi < 0$. Some materials cannot be fitted by this classification due to non-linearly variation of the magnetisation on field. Such categories are:

1. **ferromagnetic** materials: where the electrons have the magnetic moments aligned to a certain direction in the absence of an external field.
2. **ferrimagnetic** materials: where the total magnetisation exists in the absence of an external field, but unlike ferromagnetic materials within material there are neighbours pairs of the electron spins with opposite orientation.
3. **antiferromagnetic** materials: where the atoms are arranged in a way that each spin is anti-aligned with its neighbour.

Another important quantity is the induction of magnetic field. For a typical ferromagnet for example, the induction of the magnetic field has two contributions: one from the magnetic

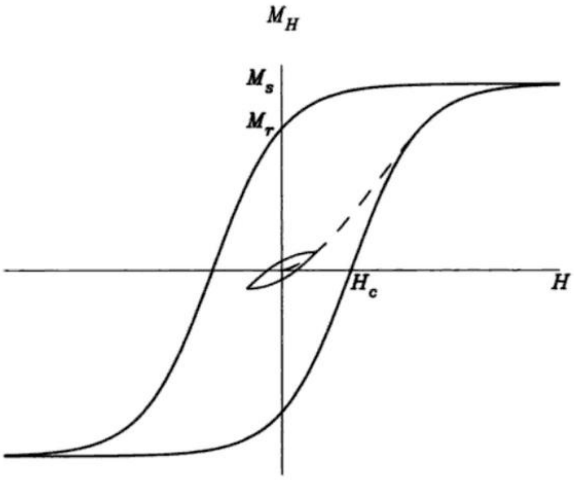

Fig. 2.2 Schematic representation of the hysteresis loop for a ferromagnetic material, showing also the virgin curve illustrated by the dashed line. [37].

field H and the other one from magnetisation[36] being defined as:

$$\mathbf{B} = \mu_0(\mathbf{H}+\mathbf{M}), \tag{2.4}$$

where $\mu_0 = 4\pi \times 10^{-7}\,\mathrm{H/m}$ is the magnetic permeability of the free space. Particular to a ferromagnet, when an external field is applied to a sample, the dependence of the magnetisation is not linear as it is mentioned above. Figure 2.2 shows a characteristic dependence of the magnetisation **M** with the magnetic field **H** specific to a ferromagnet. A couple of particularities can be observed in a hysteresis loop such as the remanence or remanent magnetisation representing the spontaneous magnetisation when the applied field is zero, the saturation magnetisation M_s is the value of the maximum magnetisation when all magnetic moments are aligned to a magnetic field, and the coercive field H_c corresponds to the value of the reversing applied field when the magnetisation is zero. The shape of this loop is indicative of the alignment of the magnetic moments. In particular, a sharp square hysteresis loop will denote a perfect coherent rotation of the moments where all of the magnetic moments are aligned to the field, whereas a round shape of the hysteresis loop will indicate an misalignment between magnetic moments or some reversible component of magnetisation.

Hysteresis loops measured at increasing temperatures reduce their area and change their shape as well. Here, at an increased temperature, the hysteresis loop converges to a line specific to paramagnetic materials. The temperature where beyond this, a ferromagnet becomes paramagnetic material is called the Curie temperature and the law which describes the magnetic susceptibility of a paramagnet as a function of temperature is the Curie-Weiss law [37]:

$$\chi = \frac{C}{T - T_C}, \tag{2.5}$$

where T_C is the Curie temperature of the magnetic material, and C is the Curie constant. Two different temperature regimes can be identified for a typical ferromagnet: above the Curie temperature, where the material does not posses a spontaneous magnetisation, and below Curie temperature where the temperature follows the Weiss law: $M/M_s = (1 - T/T_c)^{\beta}$, where M_s is the saturation magnetisation and β the critical exponent.

2.2 Extended Heisenberg Hamiltonian

In classical mechanics, the energy of the system needs to be found in order to solve the temporal and spatial evolution of a system. Similarly, in magnetism, the time and spatial evolution of the magnetic spins can be calculated by evaluating all types of energies caused by different sorts of magnetic interactions between the magnetic moments. The main types of magnetic energies have been encapsulated in the Heisenberg Hamiltonian which can be written as in equation (2.6) if the magnetostatic energy is excluded.

$$\mathscr{H} = \underbrace{-\sum_{i \neq j}^{N} J_{ij} \mathbf{S}_i \cdot \mathbf{S}_j}_{\mathscr{H}_{\text{exch}}} \underbrace{- k_u \sum_{i}^{N} (\mathbf{S}_i \cdot \mathbf{e})^2}_{\mathscr{H}_{\text{ani}}} \underbrace{- \sum_{i}^{N} \mu_0 \mu_s \mathbf{S}_i \cdot \mathbf{H}_{\text{app}}}_{\mathscr{H}_{\text{app}}}, \tag{2.6}$$

where N is the total number of magnetic spins in the system. J_{ij} is the exchange constant between a pair of spins i and j, k_u is the anisotropy constant per atom, $\mathbf{e}$ denotes the easy axis direction and $\mathbf{H}_{\text{app}}$ is the applied magnetic field vector. This Hamiltonian has an explicit dependence of spin direction $\mathbf{S}_i = \vec{\mu}_i/\mu_i$ and contains three different types of interactions such as: exchange, anisotropy, and Zeeman energy which will be detailed on following. Another importance of the equation (2.6) is given by the canonical equations which can be applied successfully. Hence, the effective field of the spin i can be determined from the partial derivative of the corresponding Heisenberg Hamiltonian with respect to spin as:

$$\mathbf{H}^i_{\text{eff}} = -\frac{1}{\mu_0 \mu_s} \frac{\partial \mathscr{H}}{\partial \mathbf{S}_i}. \tag{2.7}$$

This equation is important for the calculation of spin dynamics as the effective field is required to solve the equation of spin motion described later in this chapter.

2.2.1 Exchange Energy

The largest interaction of the Heisenberg Hamiltonian in magnetic materials is the exchange interaction which establishes the order of the spins. It was proposed by Heisenberg [38] in 1928 in order to evaluate the molecular fields which appears in ferromagnetic materials. For a system of N spins, the exchange energy is:

$$\mathscr{H}_{\text{exc}} = -\frac{1}{2}\sum_{i \neq j}^{N} J_{ij}, \mathbf{S}_i \cdot \mathbf{S}_j, \tag{2.8}$$

where $\mathbf{S}_{i,j}$ denotes the directions of spin i, respectively spin j. J_{ij} is the exchange integral between i-th atom and j-th atom. Here a negative value of the exchange integral will lead to a lowest energy when the spins align anti-parallel determining the anti-ferromagnetism behaviour while a positive value will result in a minimum of energy when the spins are parallel denoting a ferromagnetic state. The magnitude of J_{ij} is very large for the nearest neighbours being three orders of magnitude higher than the dipole interaction [39].

The origin of the exchange interaction arises from quantum mechanics of the fermions where a system of electrons respects the Pauli exclusion principle introduced to explain the multiplicity of atom spectra. Considering two atoms with unpaired electrons are approaching each other. If the spins are anti-parallel, then the electrons can share the same orbital otherwise Coulomb repulsion will appear between the atoms where the magnitude of the repulsion force depends on the separation distance between the unpaired electrons, r as:

$$F \propto \frac{e^2}{4\pi\varepsilon_0 r^2}. \tag{2.9}$$

Following Chikazumi [39], let's assume an He atom with two electrons whose wave function are $\psi_1(r_1)$, respectively $\psi_2(r_2)$, where $r_{1,2}$ are the general coordinates of the electrons. Consequently, the total Hamiltonian of the He atom is

$$\begin{aligned}
\mathscr{H} &= \mathscr{H}_1 + \mathscr{H}_2 + \mathscr{H}_{12} \\
&= -\frac{2e^2}{4\pi\varepsilon_0 r_1} - \frac{\hbar}{2m_e}\Delta_1 \\
&\quad - \frac{2e^2}{4\pi\varepsilon_0 r_2} - \frac{\hbar}{2m_e}\Delta_2 - \frac{e^2}{4\pi\varepsilon_0 r_{12}},
\end{aligned} \tag{2.10}$$

where r_1, r_2 are the vector positions of the spins and r_{12} is the distance between them. Note that Δ means Laplace operator and m_e is the electron's mass. The corresponding wave function of the He atom is a combination of both wave functions for each electron. Here, we distinguish two states: first is the anti-parallel state, where the wave function must be anti-symmetric and the other state is the parallel state, where the wave function is symmetric as:

$$\begin{aligned}\psi_s(r_1, r_2) &= \frac{1}{\sqrt{2}}[\psi_1(r_1)\psi_2(r_2) + \psi_2(r_1)\psi_1(r_2)] \\ \psi_a(r_1, r_2) &= \frac{1}{\sqrt{2}}[\psi_1(r_1)\psi_2(r_2) - \psi_2(r_1)\psi_1(r_2)]\end{aligned} \tag{2.11}$$

Respecting the quantum mechanical formalism, the total energy of the system can be written as:

$$U = \int \psi^* \mathscr{H} \psi dV, \tag{2.12}$$

where $\psi = \psi_s + \psi_a$. By expanding the calculations from equation (2.11), we obtain four terms of energy: two as an individual energy for each electron, a Coulombian term and lastly a term which does not have a correspondance in classical physics given by following expression:

$$J_{12} = \int\int \psi_1^*(r_1)\psi_2^*(r_2)\mathscr{H}_{12}\psi_2(r_1)\psi_1(r_2)dV_1dV_2 \tag{2.13}$$

J_{12} is called the Heisenberg coupling constant or the exchange integral. This treatment has been applied not only for the He atom and hydrogen molecule (H2), the nature of molecular field in ferromagnetic materials being well established based on similar calculations. For a more complex system with a high number of atoms, the exchange integral becomes more expensive to be calculated as the Schroedinger equation must be solved for an increasing number of electrons. Therefore, some approximations are assumed in order to solve a large system of atoms resulting in a theory, called density functional theory [40]. In reference [40] are presented some of the techniques proposed to solve a complex system. Very often the exchange integral between two spins becomes a tensor. The first order case is the isotropic case, where the exchange integral is a scalar. The second order case is a matrix where the non-diagonal elements are zero and the third order is the case when the exchange integral is a matrix shown below:

$$J_{ij} = \begin{bmatrix} J_{xx} & J_{xy} & J_{xz} \\ J_{yx} & J_{yy} & J_{yz} \\ J_{zx} & J_{zy} & J_{zz} \end{bmatrix} \tag{2.14}$$

The exchange energy is calculated via matrix multiplication shown in following:

$$\mathscr{H}_{\text{exc}} = -\frac{1}{2}\sum_{i\neq j}^{N} \begin{bmatrix} S_x^i & S_y^i & S_z^i \end{bmatrix} \begin{bmatrix} J_{xx} & J_{xy} & J_{xz} \\ J_{yx} & J_{yy} & J_{yz} \\ J_{zx} & J_{zy} & J_{zz} \end{bmatrix} \begin{bmatrix} S_x^i \\ S_y^i \\ S_z^i \end{bmatrix} \tag{2.15}$$

Depending on the form of the matrix, particularly the relationship between the components of the matrix, the exchange interaction can exhibit some particular forms such as two-ion anisotropy contribution [41] where the anisotropy arises purely due to the exchange or Dzyaloshinskii-Moriya (DM) exchange form.

2.2.2 Anisotropy Energy

The second term of the Heisenberg Hamiltonian is represented by the anisotropy term. The magnetic anisotropy is a property of a magnetic material which gives a preferential direction of the spins in space. This gives a rise to a variation of internal energy with the direction of the spontaneous magnetisation comprised in the anisotropy energy [39]. This preferential direction arises from spin-orbit coupling resulting in a specific crystalographic symmetries. In a ferromagnet multiple axes can exist of symmetries, but the most simple case is the uni-axial anisotropy identified in hexagonal Cobalt and FePt. The expression for uni-axial anisotropy energy is:

$$\mathscr{H}_{\text{ani}} = -k_u \sum_{i}^{N} (\mathbf{S}_i \cdot \mathbf{e})^2, \tag{2.16}$$

where k_u is the uniaxial anisotropy constant per atom calculated as dividing the macroscopic anisotropy to the number of atoms and $\mathbf{e}$ is the direction of easy axis.

Another form of the anisotropy is cubic anisotropy which occurs when the ferromagnet possess three easy axes. The strength of the cubic anisotropy is usually weaker compared with uni-axial anisotropy due to the existence of three preferential directions where the energy is:

$$\mathscr{H}_{\text{ani}}^{\text{cubic}} = \frac{k_c}{2} \sum_{i}^{N} (S_{i,x}^4 + S_{i,y}^4 + S_{i,z}^4), \tag{2.17}$$

where k_c is the cubic anisotropy per atom. Such materials which exhibit cubic anisotropies are: Fe and Ni for example which are not typically relevant for recording media applications.

2.2.3 Zeeman and magnetostatic energy

A magnetic field can appear naturally in nature as a result of an electrical current variation shown in Maxwell's equations[42]. The interaction of the magnetic spins with an external magnetic field provides a torque which can be used to switch the direction of the magnetisation being beneficial for some applications. The energy given by an external field often called Zeeman energy named after Pieter Zeeman who discovered the effect of the spectral line splitting in several components during the presence of a static magnetic field[43]. The expression of Zeeman energy is given by the following equation:

$$\mathscr{H}_{=} -\sum_{i}^{N} \mu_0 \mu_s \mathbf{S}_i \cdot \mathbf{H}_{\text{app}}, \tag{2.18}$$

where μ_0 is the magnetic permeability of free space, μ_s is the magnetic moment of the spin, and $\mathbf{H}_{\text{app}}$ is the magnetic field strength measured in J/Tm^3

Lastly, the dipole or magnetostatic energy is the energy which occurs between two magnetic spin moments $\mathbf{S}_i, \mathbf{S}_j$ separated by a distance $\mathbf{r}_{ij}$ giving a energy expressed in following equation[35]:

$$\mathscr{H}_{\text{dipole}} = \frac{\mu_0 \mu_s}{4\pi r_{ij}^3} \left[\mathbf{S}_i \cdot \mathbf{S}_j - \frac{3}{r_{ij}^2} (\mathbf{S}_i \cdot \mathbf{r}_{ij})(\mathbf{S}_j \cdot \mathbf{r}_{ij}) \right]. \tag{2.19}$$

According to Blundell [35], the magnetostatic energy of two magnetic moments of $1\mu_B$ separated by a distance of 1Åproduces an energy around $\approx 1 \times 10^{-23}$ J being weak compared with the exchange energy in order to create a order among the spins at short range distance.

2.3 Atomistic Spin Model and Langevin Dynamics

The atomistic spin dynamics (ASD) model allows us to write the extended Heisenberg Hamiltonian, shown in equation (2.6) for each individual atom within the assumption of a localised atomic moment. Practically, each atom posses an effective magnetic moment given by the unpaired electrons on the electronic shell. Unlike the micromagnetics approach, the ASD model uses more realistic parameters provided by DFT calculations or experimental measurements. Several software packages enable DFT calculations of magnetic materials such VASP[44], SIESTA[45] etc. These software packages can calculate the ground states of magnetic materials giving a full description of magnetic parameters such as atomic moment, anisotropy and exchange constants.

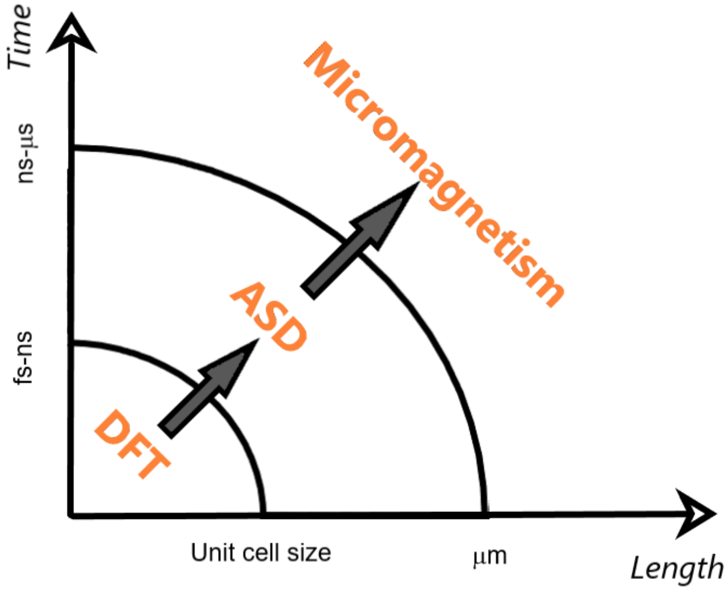

Fig. 2.3 Schematic representation of time/length scale of multi-scale calculations method.

The importance of the ASD model is given by the utility of the results provided using this model, acting like a "bridge" between first principles calculations (KKR and DFT) and micromagnetic model as shown schematically in figure 2.3. This can be embedded into a multi-scale modelling approach taking the parameters from DFT calculations as an input and giving results as output for micromagnetic LLB model[46]. The fundamental method of describing the magnetic properties of a material is given by the first principles calculations which deals with sub-femtosecond processes where the quantum mechanical effects govern the behaviour of electronic configurations. This provides estimations of the fundamental quantities such as magnetic moment length, exchange integrals and anisotropy constants followed by the ASD which utilises the DFT calculations as inputs to compute at nano-scale, magnetic processes such as Curie temperature, coercivity, and others. The limitations of DFT calculations is given by the incapability of taking into account the thermal fluctuations, whereas ASD can predict the behaviour of magnetic properties by considering the magnetic spin coupled to a thermal bath. This is described in Langevin dynamics described on following.

2.3.1 Equation of Motion

The evolution or the dynamics of the magnetisation for each spin is described by **Landau-Lifshitz-Gilbert** (LLG) equation [47]. The LLG equation begins from the assumption of a precessional motion performed by an electron as shown previously in figure 2.1 where the classical mechanics of a rotational rigid body can be applied for the electron precession as [48]:

$$\frac{d\mathbf{L}}{dt} = \mathbf{T}, \tag{2.20}$$

where $\mathbf{L}$ is the angular momentum equivalent of the spin $\mathbf{S}$ and $\mathbf{T}$ is the torque of the spin, defined as:

$$\mathbf{T} = -\gamma \mathbf{S} \times \mathbf{H}, \tag{2.21}$$

where $\mathbf{H}$ is the effective field acting on the spin and γ represents the gyromagnetic ratio calculated with following formula:

$$\gamma = \frac{g|e|}{2m_e C} \tag{2.22}$$

By introducing equation (2.21) in equation (2.20) we can obtain the Landau equation of precessional motion of the electron without any damping expressed as:

$$\frac{d\mathbf{S}}{dt} = -\gamma \mathbf{S} \times \mathbf{H} \tag{2.23}$$

Equation (2.23) shows an undamped precession of the spin, however in reference [48] is shown that the motion of the spins is not infinite: the precession decays due to damping mechanisms which are introduced phenomenologically explaining also the energy loss. The damping force is found to be directly proportional to the time-variation of the magnetisation as $\mathbf{H}_{\text{damping}} = -\lambda \frac{d\mathbf{S}}{dt}$. By introducing this damping field into the effective field the LLG equation can be derived as detailed in Appendix A. The LLG equation for a single spin is:

$$\frac{d\mathbf{S}}{dt} = -\frac{\gamma}{1+\lambda^2}\left[\mathbf{S} \times \mathbf{H} + \lambda \mathbf{S} \times (\mathbf{S} \times \mathbf{H})\right], \tag{2.24}$$

where λ is the Gilbert damping parameter for a single atomic spin which includes local intrinsic effects. The LLG equation shows a finite elliptical motion of the spin unlike equation (2.23). This equation is composed of two components of the motion: one is the precession determined by the first part of the equation $\mathbf{S} \times \mathbf{H}$ and the second term describes the alignment of the spin towards the effective field direction, $\mathbf{H}$ determined by the double cross product:

S × **S** × **H**. This is illustrated schematically in figure 2.4 showing the trajectory of a spin during the alignment along field direction from in-plane starting position.

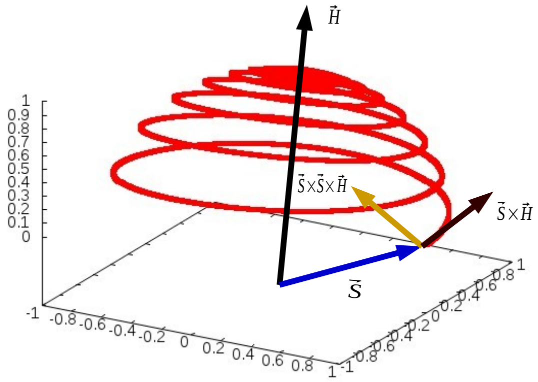

Fig. 2.4 Schematic representation of a damped precessional motion of a spin in an applied field. The spin is initially in-plane aligned following a precessional alignment along applied field direction, **H**.

The effective field in the equation above (2.24), **H** can be calculated using equation (2.7) which can be determined analytically for the zero Kelvin case. Once the applied field is determined, this equation can be solved for a single non-interacting spin straight forward in cartesian coordinates by separating the variables and integrating. The solutions are the following [49]:

$$\begin{cases} S_x(t) = \operatorname{sech}\left(\frac{\alpha\gamma H}{1+\alpha^2}t + A\right)\cos\left(\frac{\gamma H}{1+\alpha^2}t + B\right) \\ S_y(t) = \operatorname{sech}\left(\frac{\alpha\gamma H}{1+\alpha^2}t + A\right)\sin\left(\frac{\gamma H}{1+\alpha^2}t + B\right) \\ S_z(t) = \tanh\left(\frac{\alpha\gamma H}{1+\alpha^2}t + A\right) \end{cases} \tag{2.25}$$

A and B are constants of integration. We can find these integration constants for particular cases when the initial conditions are established. For a switching of the spin from the in-plane position along x-axis to z-axis, the integration constants are zero. This system of solutions can help to perform a basic test for a single non-interacting spin at zero Kelvin when we implement a numerical integration scheme such as Heun scheme for example.

2.3.2 Langevin dynamics. Noise mechanism

We determined the equation of the spins dynamics in the absence of any temperature being able to describe the time evolution of the magnetisation. In addition to this, the interest of our work in this thesis is to study the dynamics of a system at finite temperatures, therefore a theory to describe the thermal behaviour is necessary to be included in our investigation model.

Particular to ferromagnetic materials, the dependence on temperature is given by the Weiss law for a micromagnetic particle. However, at the atomistic scale there is no theory to claim any temperature dependence for an individual spin until 1979 when Brown [50] derived a formalism to describe the thermal fluctuation on fine nanoparticles which is applied later to atomistic temperature simulations. Within this model, called fluctuation-dissipation theorem, it is assumed a statistical probability for a transition of a particle from a certain energy state to another which strongly depends on temperature. Hence, there is a *stochastic* term which causes fluctuations of the magnetisation at non-zero temperature. This can be transposed for an individual spin as long it is assumed that the electron is coupled to a thermal bath and posses a stochastic field which is additive to the effective field as:

$$\mathbf{H}^i_{\text{eff}} = -\frac{1}{\mu_0 \mu_s} \frac{\partial \mathscr{H}}{\partial \mathbf{S}_i} + \underbrace{\zeta_i(t)}_{\text{stochastic}} , \tag{2.26}$$

where ζ_i is the thermal field attributed to each spin, i. Equation (2.26) represents the Langevin equation of the magnetic field comprising two terms: deterministic and stochastic term. This can be introduced in LLG equation forming the Langevin equation of spin dynamics known as the stochastic LLG equation expressed as:

$$\frac{d\mathbf{S}_i}{dt} = -\frac{\gamma}{1+\lambda^2} \left[\mathbf{S}_i \times (\mathbf{H}_i + \zeta_i) + \lambda \mathbf{S}_i \times (\mathbf{S}_i \times (\mathbf{H}_i + \zeta_i))\right] \tag{2.27}$$

Equation (2.27) is not directly integrable as a continuous function since the fluctuation field is a stochastic variable. There are two approaches for solving this kind of stochastic equation such as Itô integral and Stratonovich integral which gives a pseudo-analytical solution of the sLLG. For a large system, numerical methods to compute these integrals are needed, but before proceeding to detail the solvers for this equation, we focus on the noise mechanism, particularly to find the expression and properties of the noise. In reference [51], the main two properties of the noise are stated shown in following:

$$\begin{cases} \langle \zeta_i(t) \rangle = 0, \\ \big\langle \zeta_i(t), \zeta_j(t) \big\rangle = 2\delta_{ij}\delta(t-s)D \end{cases} \tag{2.28}$$

where i, j are the cartesian components of the spins, D represents the strength of noise, assumed to be isotropic and also it depends on temperature. $\langle\rangle$ denotes the average of the thermal field calculated for a transition between two energy states. δ_{ij} is the Kronecker function which ensure two different energy states. and $\delta(t-s)$ represents the auto-correlation function over a time interval $t-s$. This correlation function is determined within the mathematical model of Wiener for a Brownian motion which states that over a finite time interval $[0, t-s]$ the probability of event is a random variable which follows a Gaussian distribution with zero mean shown in the equation below:

$$\delta(t-s) = \sqrt{t-s}N(0,1) \tag{2.29}$$

where $N(0,1)$ is the standard Gaussian distributed number with zero mean. In this case, the random number does not depend on the time interval as long as this is enough to reach equilibrium. This technique is called *white* noise.

Finally, the strength of the noise, D needs to be determined in order to have a full depiction of Langevin dynamics. In references [52, 51] it is shown how to calculate the amplitude of the noise by solving the associated Fokker-Planck (FP) equation. A system described by a Langevin equation has a corresponding FP equation whose expression for the sLLG equation is following:

$$\frac{\partial P(t)}{\partial t} = -\frac{\partial}{\partial \mathbf{S}}\left[\left(-\mathbf{S}\times\mathbf{H} - \lambda\mathbf{S}\times(\mathbf{S}\times\mathbf{H}) + D(1+\lambda^2)\mathbf{S}\times\left(\mathbf{S}\times\frac{\partial}{\partial\mathbf{S}}\right)\right)P(t)\right], \tag{2.30}$$

where $P(t)$ is the probability distribution. When the bath reaches thermodynamic equilibrium, the time-derivative of probability ditribution vanishes. Again, we deal with an electron bath, whose probability distribution is given by the Boltzmann distribution, $P_0 = e^{-\frac{\mathscr{H}}{k_BT}}$. Hence, the equation for stationary case can be written as:

$$\frac{\partial P_0}{\partial t} = -\frac{\partial e^{-\beta\mathscr{H}(S)}}{\partial \mathbf{S}} = \beta\mathbf{H}P_0 = 0, \tag{2.31}$$

where β is $1/k_BT$. By expanding the calculations of equations (2.30) and (2.31), the expression for D can be obtained as:

$$D = \frac{2\lambda k_B T}{\gamma \mu_s}, \tag{2.32}$$

where $|\gamma|$ is the gyromagnetic factor shown in Table 2.1.

To summarize, by taking into account equations (2.28), (2.29), and (2.32), we obtained the following expression for the thermal field:

$$\mu_0 \mathbf{H}^{\mathrm{th},i}_{x,y,z} = \sqrt{\frac{2\lambda k_B T}{\gamma \mu_s \Delta t}} \mathbf{N}(0,1), \tag{2.33}$$

where $\Delta t = t - s$ is the interval time mentioned in equation (2.29). In numerical integration this represents the time step of the solver. $\mathbf{N}(0,1)$ is the Gaussian distribution with zero mean on x, y, z dimensions.

Following Stratonovich calculus which is consistent with the rules of classical deterministic integration and differentiation it can be obtained pseudo-exact solutions for each component of the spin[49]:

$$\begin{aligned}
S_x(t) &= S\mathrm{sech}\left[\frac{\lambda\gamma(Ht + \mu_0 H_{\mathrm{th}})}{1+\lambda^2}\right] \cos\left[\frac{\gamma(Ht + \mu_0 H_{\mathrm{th}})}{1+\lambda^2}\right] \\
S_y(t) &= S\mathrm{sech}\left[\frac{\lambda\gamma(Ht + \mu_0 H_{\mathrm{th}})}{1+\lambda^2}\right] \sin\left[\frac{\gamma(Ht + \mu_0 H_{\mathrm{th}})}{1+\lambda^2}\right] \\
S_z(t) &= S\tanh\left[\frac{\lambda\gamma(Ht + \mu_0 H_{\mathrm{th}})}{1+\lambda^2}\right]
\end{aligned} \tag{2.34}$$

2.4 Implementation and integration methods

The ASD model presented in the previous section has been successfully implemented and tested in the VAMPIRE software package [1] a powerful tool to simulate the magnetic properties of nano-materials. VAMPIRE is a relatively large C/C++ object-oriented code using minimal external libraries which makes it more versatile in order to be installed on a wide range of computer architectures. Despite the minimal external libraries requirement, it confers multiple features presented in reference [1]. This code runs efficiently and gives good performance due to ability of running in parallel using Message Passing Interface (MPI) and General-Purpose Computing on Graphics Processing Units (GPGPU).

Our simulations presented in this thesis are obtained solely by using VAMPIRE and adding our contribution. The framework structure of this code is detailed in reference [1] which follows several steps:

- first step is to create the unit cell type. Priory using VAMPIRE, the information about the crystal structure of the material is required. After the unit cell is created, this is replicated with respect to a specific geometry achieving the dimensions desired by the user.
- the second step is the initialisation of variables imposed by the user followed by the calculation of exchange interactions and the list of neighbours.
- the third step is to simulate the effective magnetic properties such as: spin fields, positions, magnetisations etc. Here, there are two approaches. One is dynamically by integrating the sLLG equation using different integration schemes and the second approach is represented by the energetic solutions using Monte-Carlo or Constrained Monte-Carlo.
- the last step is the average and extraction of the results

We note that the magnetic quantities commonly used in VAMPIRE are in agreement with the International System of Units. However, in there are few quantities we need to set as inputs which are not in the SI units list. The atomic moments, for example, should be set as multiple of Bohr magneton μ_B, whereas the applied magnetic field is defined in Tesla. The rest of the constants used in VAMPIRE are summarised in the table below.

Quantity	Symbol	SI value
Bohr magneton	μ_B	$9.274 \times 10^{-24}\,\mathrm{JT}^{-1}$
Gyromagnetic ratio	γ	$1.76 \times 10^{11}\,\mathrm{T}^{-1}\mathrm{s}^{-1}$
Permeability of free space	μ_0	$4\pi \times 10^{-7}\,\mathrm{T}^2\mathrm{J}^{-1}$
Boltzmann constant	k_B	$1.3807 \times 10^{-23}\,\mathrm{JK}^{-1}$

Table 2.1 Table of constants

2.4.1 Heun and Semi-implicit scheme

In this section we will detail the integration methods for sLLG equation presented in the previous section. Here, we start with the Heun scheme followed by the semi-implicit scheme, already implemented in VAMPIRE. Solving the sLLG equation can be done within the Stratonovich interpretation which allows us to treat the sLLG equation as a Riemann integral[52]. Therefore, we can treat sLLG as ordinary differential equation using Taylor expansions.

The simplest integration scheme of sLLG is the Euler method whereas Heun method is the Euler scheme with an additional step called predictor-corrector. For a generic deterministic function, $f(t,x) = y'(t)$, with an initial condition, $y(t_0) = y_0$, the Euler scheme can be derived from the Taylor expansion as:

$$y(t_0 + h) = y(t_0) + hy'(t_0) = y_0 + hf(t_0), \tag{2.35}$$

where h is a generic time step. This method retains only the first term of the Taylor expansion. A more advanced integration scheme will include more Taylor terms such as Runge–Kutta methods. In addition to Euler method, Heun uses the Euler step as an intermediate step before calculating the final step. For a single spin described by the sLLG equation, the Heun step (predictor-corrector step) is following [1]:

$$\tilde{\mathbf{S}}_{n+1} = \mathbf{S}_n + \Delta\mathbf{S}\Delta t, \tag{2.36}$$

where

$$\begin{aligned}\Delta\mathbf{S} = -\frac{\gamma}{1+\lambda^2}[\mathbf{S}_n \times (\mathbf{H}_{\text{eff}} + \mathbf{H}_{\text{th}}) +& \\ \lambda\mathbf{S}_n \times (\mathbf{S}_n \times (\mathbf{H}_{\text{eff}} + \mathbf{H}_{\text{th}}))]&\end{aligned} \tag{2.37}$$

Final position is calculated as a function of the predictor step. $\tilde{S}_{n+1}$, as:

$$\mathbf{S}_{n+1} = \mathbf{S}_n + \frac{1}{2}(\Delta\mathbf{S} + \Delta\tilde{\mathbf{S}})\Delta t, \tag{2.38}$$

where

$$\begin{aligned}\Delta\tilde{\mathbf{S}} = -\frac{\gamma}{1+\lambda^2}[\tilde{\mathbf{S}}_{n+1} \times (\mathbf{H}_{\text{eff}} + \mathbf{H}_{\text{th}}) +& \\ \lambda\tilde{\mathbf{S}}_{n+1} \times (\tilde{\mathbf{S}}_{n+1} \times (\mathbf{H}_{\text{eff}} + \mathbf{H}_{\text{th}}))]&\end{aligned} \tag{2.39}$$

This method is based on trapezoidal rule of numerical integration being an explicit scheme because the unknown quantity $\mathbf{S}_{n+1}$ appears only on the left side of the equation. This makes it very simple to implement it, and, despite the simplicity it confers optimal computational efficiency converging to the Stratonovich solution. However, the length of the spin is not preserved, a spin normalisation being mandatory after the calculations of both the intermediate and final step. Besides the spin normalisation, the effective fields needs to be re-evaluated.

In order to obtain a stable convergence using Heun method, for each partial step is important to choose a correct time step depending on the simulation temperature. It is well known that above and in the vicinity of Curie temperature, the Heun scheme becomes unstable. In reference [1], Evans *et al.* performed some tests in order to find the dependence of the quality of convergence as a function of the ratio between the simulation temperature and the Curie temperature. In figure 2.5 is shown the mean magnetisation of a generic ferromagnet as a function of time step at different temperature simulations. We observed a good convergence for time step lower than 10×10^{-15} s for a range of temperature below the Curie point. Above Curie temperature, the material acts like a paramagnet where the spins are randomly ordered determining the vanishing of mean magnetisation.

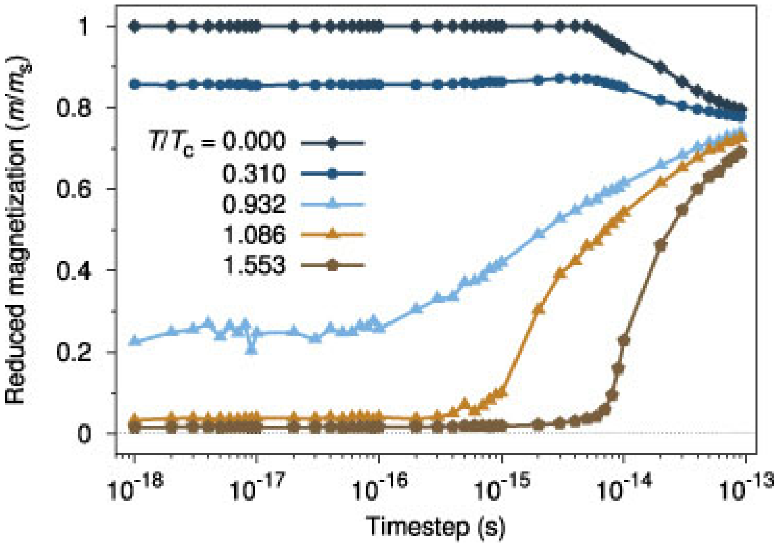

Fig. 2.5 The dependence of time step on mean magnetization for different reduced temperatures for the Heun integration scheme. This graph is taken from reference [1].

Two new integration schemes have been proposed by Mentink *et al.* [53] being more promising in terms of stability and speed of the calculations. In addition, the second scheme, called semi-implicit B is supposed to preserve the length of the spin. This scheme has been previously investigated by Ellis *et al.*[54] in their investigations on rare-earth doped permalloy. The methodology of this scheme is similar to the Heun scheme, calculating an intermediate step following:

$$\tilde{\mathbf{S}}_{n+1} = \mathbf{S}_n - \frac{\mathbf{S}_n + \tilde{\mathbf{S}}_{n+1}}{2} \times \mathbf{A}(\mathbf{S}_n), \tag{2.40}$$

where

$$\mathbf{A}(\mathbf{S}) = \frac{\gamma\Delta t}{(1+\lambda^2)\mu_s}[\mathbf{H}_{\mathrm{eff}}(\mathbf{S}) + \mathbf{H}_{\mathrm{th}} + \lambda\mathbf{S}\times(\mathbf{H}_{\mathrm{eff}}(\mathbf{S}) + \mathbf{H}_{\mathrm{th}})]. \tag{2.41}$$

The final step corresponding to the time step, $n+1$, is calculated via the equation:

$$\mathbf{S}_{n+1} = \mathbf{S}_n - \frac{\mathbf{S}_n + \mathbf{S}_{n+1}}{2} \times \mathbf{A}\left(\frac{\mathbf{S}_n + \mathbf{S}_{n+1}}{2}\right), \tag{2.42}$$

We identified the presence of the unknown terms $\tilde{\mathbf{S}}_{n+1}$ $\mathbf{S}_{n+1}$ on both sides of the equations above denoting implicit dependences. The mechanism of solving this kind of equations includes a Cayley transform [55] corresponding to each implicit equation presented above as:

$$\begin{aligned}\tilde{\mathbf{S}}_{n+1} &= \mathrm{Cay}(\mathbf{A}(\mathbf{S}_n,t))\mathbf{S}_n\\ \mathbf{S}_{n+1} &= \mathrm{Cay}\left(\mathbf{A}\left(\frac{\mathbf{S}_n + \tilde{\mathbf{S}}_{n+1}}{2},t\right)\right)\mathbf{S}_n\end{aligned} \tag{2.43}$$

The corresponding Cayley transform for the intermediate step, $\tilde{\mathbf{S}}_{n+1}$, is:

$$\mathrm{Cay}(\mathbf{A}(\mathbf{S}_n,t))\mathbf{S}_n = \mathbf{S}_n + \frac{\mathbf{A}(\mathbf{S}_n,t)\times\mathbf{S} + \frac{1}{2}\mathbf{A}(\mathbf{S}_n,t)\times\mathbf{A}(\mathbf{S}_n,t)\times\mathbf{S}_n}{1+\frac{1}{4}|\mathbf{A}(\mathbf{S}_n,t)|^2} \tag{2.44}$$

Similarly for the final step, $\mathbf{S}_{n+1}$, the corresponding Cayley transform can be expressed as:

$$\begin{aligned}\mathrm{Cay}\left(\mathbf{A}\left(\frac{\mathbf{S}_n + \tilde{\mathbf{S}}_{n+1}}{2},t\right)\right)\mathbf{S}_n = \mathbf{S}_n &+ \frac{\mathbf{A}\left(\frac{\mathbf{S}_n+\tilde{\mathbf{S}}_{n+1}}{2},t\right)\times\mathbf{S}}{1+\frac{1}{4}|\mathbf{A}\left(\frac{\mathbf{S}_n+\tilde{\mathbf{S}}_{n+1}}{2},t\right)|^2} +\\ &\frac{\frac{1}{2}\mathbf{A}\left(\frac{\mathbf{S}_n+\tilde{\mathbf{S}}_{n+1}}{2},t\right)\times\mathbf{A}\left(\frac{\mathbf{S}_n+\tilde{\mathbf{S}}_{n+1}}{2},t\right)\times\mathbf{S}_n}{1+\frac{1}{4}|\mathbf{A}\left(\frac{\mathbf{S}_n+\tilde{\mathbf{S}}_{n+1}}{2},t\right)|^2}\end{aligned} \tag{2.45}$$

Now we have explicit equations for the semi-implicit integration scheme methodology which allows us a straight forward process of implementation in VAMPIRE. In order to test the performance of semi-implicit integration scheme implemented in VAMPIRE, we performed a series of benchmarks similar to Evans *et al.* [1] presented in figure 2.5. We chose a generic ferromagnet whose Curie temperature is 1388 K with an hcp structure corresponding to Co. The exchange constant as input using nearest neighbours approximation can be calculated via following equation[1]:

$$J_{ij} = \frac{3k_BT_c}{\varepsilon z}, \tag{2.46}$$

where $\varepsilon = 0.79$ is a correction factor which arises due to the spin waves in 3D Heisenberg model [56] and z is the coordination number; for an hcp structure, the coordination number is 12, for example. We performed, therefore, several time series at different temperatures as a ratio of Curie temperature. We allowed an total integration of 0.1 ns for each timestep value. The dependence of reduced magnetisation as a function time step at different values of temperature is shown in figure 2.6.

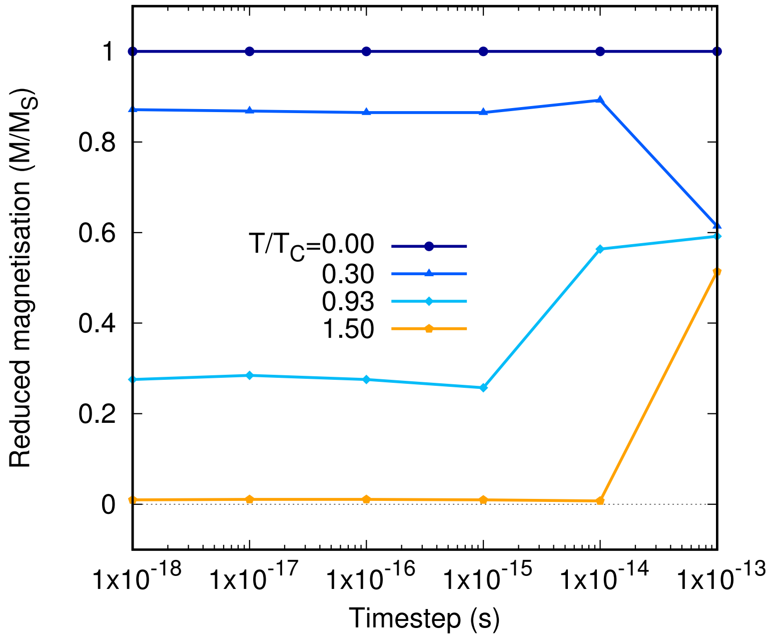

Fig. 2.6 The dependence of time step on mean magnetisation for different reduced temperatures for the semi-implicit integration scheme.

Overall, we observed a reasonable performance of the semi-implicit scheme especially at low temperatures. At zero Kelvin, the magnetisation is preserved at any timestep, Δt, values comparing with Heun scheme where the reduced magnetisation beyond a certain value of Δt breaks which violates the conservation law of the LLG equation. At high temperatures, in vicinity of Curie point, the Heun scheme, however, confers a better average, but the semi-implicit scheme is more stable up to a timestep value, $\Delta t = 1 \times 10^{-14}$ s. A time step of 1×10^{-15} s should be sufficient to obtain a feasible integration of sLLG equation at elevated temperatures offering better integration compared to the Heun scheme. A time step with an order higher will lead to a 10 times longer computation time. This is important when we think a strategy of parallel calculations. Most of the strategies involve spatial decomposition whereas time parallelisation is not admissible in ASD simulations. Hence, an integration scheme which is capable of good performance at low values of the timestep is more desirable.

Therefore, the semi-implicit scheme is a good candidate for an implementation in MPI or GPGPU algorithms.

2.4.2 Monte-Carlo and Constrained Monte-Carlo methods

The previous integration methods refer to the dynamical approach of ASD by solving the LLG equation of motion. In this subchapter, we will present few ways to energetically evolve the dynamics of the spins which takes into account the thermal fluctuations being faster to simulate the equilibrium properties for a system, such as the Curie temperature, for example. These methods are based on Monte-Carlo (MC) techniques which are physical time-independent [57] and the fundamental idea is to make an adjustment to the physical system and calculate the variation of energy, ΔE, between these two states of the spins. MC simulations converge rapidly to equilibrium saving the computation time and are relatively easy to implement.

One efficient algorithm is represented by Metropolis Monte Carlo (MMC) presented on following. The procedure of MMC respect several steps. The first step is to choose randomly a spin, $\mathbf{S}_i$. In the second step the initial direction of the spin is changed randomly into a new position, $\mathbf{S}_i'$, called trial move. Finally, the difference of energies between the old and new position is calculated, $\Delta E = E(\mathbf{S}_i') - E(\mathbf{S}_i)$ and compared with the probability of acceptance calculated via following equation:

$$P = \exp\left(-\frac{\Delta E}{k_B T}\right) \tag{2.47}$$

If the computed probability through equation (2.47) is greater than 1, then the spin adopts the move otherwise the position is restored back to initial position, $\mathbf{S}_i$. This steps are repeated for each atom in the system, representing a single MC step. In reference [58], Hinzke and Nowak demonstrated that the performance of MC method is influenced by the type of the trial move performed depending on the magnetic properties of the system. In figure 2.7 are shown schematically these three types of moves described in detail in reference [58].

For example a large anisotropy material will be better performed by MC with a spin flip move illustrated in figure 2.7 (a). This move reverses the spin direction once the move is accepted similar to an Ising model. A second alternative to simulate nucleation processes using MC is given by the random move which does not depend on the initial direction shown schematically in figure 2.7 (c). Unlike the spin-flip move, this trial move does not force the spin to jump the energy barrier; a uniform random move has been performed. The type of move which ensures the ergodicity the most is given by the Gaussian move shown in figure 2.7 (b). This move takes in to account the initial move and allows the spin to fluctuate within

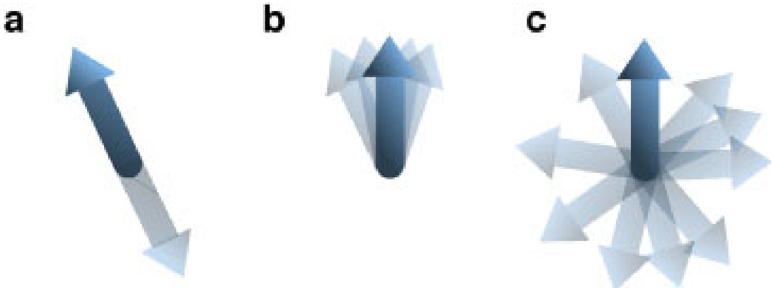

Fig. 2.7 Schematic illustration of the three types of trial moves: (a) spin flip; (b) Gaussian and (c) random. This picture is reproduced from reference [1].

a cone centred on initial direction following next expression[1]:

$$\mathbf{S}_i' = \frac{\mathbf{S}_i + \sigma_g \mathbf{N}}{|\mathbf{S}_i + \sigma_g \mathbf{N}|}, \tag{2.48}$$

where $\mathbf{N}$ is a Gaussian distributed random number and σ_g is the width of the cone. The width of the cone is temperature-dependent similar to the Langevin term given by following expression:

$$\sigma_g = \frac{2}{25}\left(\frac{k_B T}{\mu_B}\right)^{\frac{1}{5}} \tag{2.49}$$

This method properly describes the coherent reversal processes and different methods of testing have been performed successfully by Evans *et al.* [1] showing a good agreement between MC simulations and sLLG equation, both converging to a unique solution of temperature magnetisation dependence. In some cases the convergence can be very slow, therefore the cone width can be adaptive depending on the rate of acceptance of MC moves. This method is called adaptive MC method and the cone width can be expanded for a high rate of acceptance or lowered for a low rate of acceptance.

Another powerful method used in this thesis is the constrained Monte-Carlo (CMC) method which allows us to calculate the magnetic properties along a specific direction. This method was proposed by Asselin *et al.* [59] in order to calculate the temperature dependence of anisotropy for bulk and surfaces. This method involves to pick up a pair of spins where the trial move described above acts on both spins. The CMC method implies several step as:

- first step is to randomly choose a *primary* spin $\mathbf{S}_i$ and a *compensation* spin $\mathbf{S}_j$.
- in the second step a trial MC move is applied to the primary spin obtaining a new spin $\mathbf{S}_i'$.

- in the third step the x and y components of the compensation spin are adjusted in order to mantain the magnetisation length of x, y components as:

$$\begin{aligned}\mathbf{S}'_{jx} &= \mathbf{S}_{jx} + \mathbf{S}_{ix} + \mathbf{S}'_{ix}, \\ \mathbf{S}'_{jy} &= \mathbf{S}_{jy} + \mathbf{S}_{iy} + \mathbf{S}'_{iy}\end{aligned} \tag{2.50}$$

- the fourth step consists in adjusting the z component,

$$\mathbf{S}'_{jz} = \mathrm{sgn}(\mathbf{S}_{jz})\sqrt{1 - \mathbf{S}'^{2}_{jx} - \mathbf{S}'^{2}_{jy}} \tag{2.51}$$

  If the value enclosed within the square root is negative the iteration stops and takes a null move.

- In this step the new magnetisation is computed as:

$$\mathbf{M}'_z = \mathbf{M}_z + \mathbf{S}'_{iz} + \mathbf{S}'_{jz} - \mathbf{S}_{iz} - \mathbf{S}_{jz}. \tag{2.52}$$

  If $|\mathbf{M_z}| \leq 0$, stop and take null move. This step is followed by the computation of the energy difference: $\Delta\mathscr{H} = \mathscr{H}' - \mathscr{H}$

- in the seventh step we compute the acceptance probability, P:

$$P = \min\left[1, \frac{M'_z}{M_z}\frac{S_{jz}}{S'_{jz}}\exp\left(-\frac{\Delta\mathscr{H}}{k_B T}\right)\right]. \tag{2.53}$$

- in the last move the move is accepted with probability P or rejected as null move with the probability $1 - P$.

This method proved to achieve the ergodicity and it has been tested successfully in reference [59] by reproducing the temperature dependence of anisotropy $L1_0$ FePt. This allows to obtain the reversal mechanism by using the Gaussian trial move and it will be used in our investigations of finding the energy barrier for different magnetic systems.

2.5 Conclusion and further work

To summarise, in this chapter we have covered the fundamental theoretical concepts of magnetism, particularly relating to ASD model. We also detailed the method we used throughout this thesis finding Langevin dynamics a good approach to describe the thermal fluctuations of the magnetic particles at atomistic scale. We found that sLLG equation can be written individually for each atom being solved within Stratonovich's interpretation. Our integration schemes proved to work reasonably giving good qualitative and quantitative results. Another method described in this chapter is MC/CMC method which allows the determination of the static properties of magnetic materials in an efficient way giving results in good agreement with the experimental measurements.

As further work, a new method to solve the energy barrier and activation volume is under the progress of developing consisting in a semi-analytical method by applying a constraint using Lagrange multipliers[60] .

Chapter 3

Investigation model of inter-granular exchange interaction

It is well known in micro-magnetism that two ferromagnets interact in such a way that each one of them tries to align the other in its own direction. This is called inter-granular exchange interaction with respect the micro-scale of the sizes. In this chapter, the interaction between finite sized grains is studied with regard to understanding the dependence of the inter-granular exchange on a series of factors such as the distance between the grains, temperature and the quality of the isolating layer.

We studied CoPt grains with and without anisotropy in different cases which might occur following the deposition of the magnetic material where inter-granular exchange interactions can be detrimental for the recording process. An optimal separation between the grains needs to be found during the sputtering process in order to increase the areal density depending on the isolating layer which might be partially affected by the migration of the magnetic atoms into the separation layer, leading to exchange coupling. This exchange can be used, as part of the recording optimisation process, to give stability to the written bits against the demagnetisation field. Using an atomistic spin model we reproduced an exponential decay of the inter-granular exchange with thickness of the isolating layer for a tri-layer system previously measured by Sokalski *et al.* [2]. In addition, a hexagonal distribution of CoPt grains is studied in this chapter to understand which exchange model is more suitable to depict the interaction between the magnetic grains. Here, we found a limitation of the simple classical Heisenberg model for higher separations and a better description is provided by adding a biquadratic term which is detailed later in the following.

In both cases, thickness dependence of the exchange interaction can be modeled with an exponential power law but the angular dependence differs from direct exchange compared with the indirect exchange. In other words, we distinguished two regimes where the exchange form can fall depending on the distance and doping density rate of the magnetic impurities into the separation layer.

3.1 Introduction

The areal density of the magnetic grains can be increased in two ways: one is the reduction of the grain sizes and, secondly is to reduce the separations between the grains. As shown early in this thesis in the finite sized simulations, the sizes of the grains cannot be decreased beyond a critical size where the grain can lose its magnetic properties affecting the recording performance.

The challenge is to fabricate the recording media using the sputtering deposition method, ideally to obtain an uniform arrangement of isolated grains. The deposition method implies a growing process of the magnetic grains in such a way the grains do not touch each other. To do that, a non-magnetic phase is necessary to be created by using a doping process with non-magnetic elements which migrate to the boundary of the magnetic grains. Here, the deposition conditions such as annealing temperatures and concentration of non-magnetic elements dictate the magnetic features of the grains and the segregant layer. This has been extensively demonstrated for a wide range of magnetic material depositions[61, 62], particularly for FePt thin films where the annealing temperature can reduce the intergranular spacing. Shao *et al.*[63] reported a strong dependence of the magnetic properties of FePt/Ag thin films where both M_s and H_c increase with higher annealing temperatures. In addition to this, reference [62] reports a decreased spacing between the FePt grains in combination with Cu, Ag, and Au as direct effect of the annealing temperature.

The thickness of the segregant layer is observed to decrease the inter-granular exchange energy following an exponential law. Sokalski and his co-workers [2] measured the coupling energy density on separation thickness by doping CoPt with Chromium oxide. This is shown in figure 3.1 where three different oxides have been measured giving a similar decrease with the thickness of the doping layer following[64]:

$$\sigma = A\exp\left(-\frac{\delta_{\mathrm{ox}}}{B}\right) + C \tag{3.1}$$

where δ_{ox} is the thickness of the oxide layer and A,B,C are some arbitrary fitting constants.

The difficulty is to find the theoretical support for this exponential law of the coupling exchange decrease. It has been suggested that this can be attributed to the direct exchange through "pinholes" detailed in references [65–67] caused by a magnetic disorder in the segregant layer which gives rise to direct ferromagnetic coupling between the grains.

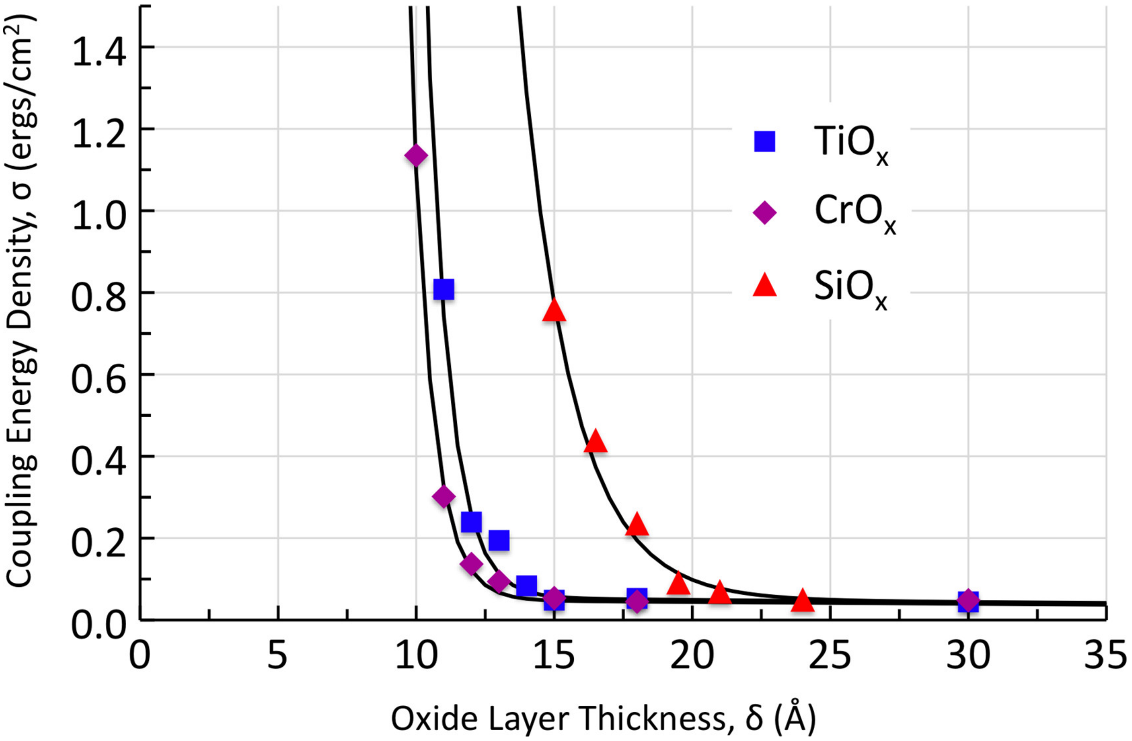

Fig. 3.1 Measured coupling exchange energy at different thicknesses of the oxide layer for different doping elements. The solid line stands for an exponential fitting function given by the equation (3.1). Taken from reference [2].

Slonczewski [68] developed an indirect model of the exchange between two identical ferromagnets separated by a non-magnetic tunneling barrier. His formalism is based on quantum penetration of the energy barrier by calculating the density of states corresponding to each different barrier heights. Besides the angular dependence of the Heisenberg exchange, Slonczewski found an exponential decrease of the Heisenberg coupling with the barrier's height as $J \approx e^{-2kd}$, where k is the electron momentum and d is the length of the barrier which might support the experimental results by Sokalski[2] and others [66, 69, 70].

3.2 Heisenberg and biquadratic model of the exchange interaction. Theory of the intergranular exchange.

A basic form of the exchange interaction energy is given by the Heisenberg form, often referred to as bilinear variation. In references [71, 72] a thin film of dispersed particles is modeled where the exchange between neighbouring particles i and j can be calculated as[71]:

$$\begin{aligned} E^{ij}_{\text{exch}} &= -N_{ij}J_{ij}\mathbf{S}_i \cdot \mathbf{S}_j \\ &= -N_{ij}J_{ij}\cos(\theta), \end{aligned} \tag{3.2}$$

where N_{ij} is the number of particles in the contact area between (i, j) and θ is the angle between the magnetisations of the pair of spins. In the classical model of micromagnetism the exchange energy can be written in terms of angles $\theta_{i,j}$ which is always assumed to be small[73]. Here, the small angles approximation can be used allowing equation (3.2) to be written for coupled spins as:

$$E^{ij}_{\text{exch}} \propto JS \sum_{\text{neighbours}} \theta^2_{i,j} \tag{3.3}$$

Experiments done by Rührig *et al.* [74] on Fe/Cr multilayers reveal unusual domain formation which gives rise to perpendicular orientation of the Fe magnetisation with respect to the Cr magnetisation. This can be explained by introducing a new higher order term of the Heisenberg exchange form called biquadratic transforming equation (3.2) into [74]:

$$\begin{aligned} E^{ij} &= A^{ij}(1 - \mathbf{m}_i \cdot \mathbf{m}_j) + B^{ij}[1 - (\mathbf{m}_i \cdot \mathbf{m}_j)^2] \\ &= \underbrace{A^{ij}[1 - \cos(\theta)]}_{\text{Bilinear}} + \underbrace{B^{ij}[\sin(\theta)^2]}_{\text{Biquadratic}}, \end{aligned} \tag{3.4}$$

where θ is the angle between magnetic vectors, A^{ij} and B^{ij} are the bilinear and biquadratic exchange constants between the grains i and j. These constants are strongly dependent on the separation distance between the layers giving two regimes of interactions. A short distance will lead to a stronger Heisenberg form having an exponential decrease as shown by Sokalski experiments whereas the biquadratic effect is more pronounced at higher distance, greater than 1.5 nm as shown in the reference [74] for this particular multilayer system.

In addition to this, biquadratic exchange varies with the temperature demonstrated in the experiments done by Gutierrez *et al.*[75] on Fe/Al/Fe tri-layer system. Their measurements on orthogonal magnetic layers shows a power law decay of the intergranular exchange which can be modeled with the following law:

$$B^{ij} = B_0^{ij}(1 - T/T_C)^{\alpha} \tag{3.5}$$

For this 90° alignment an exponent of $\alpha = 2$ is found giving a quadratic law as $B^{ij} \propto (1 - T/T_C)^2$.

The existence of the biquadratic term can be related to three types of theoretical explanations. First evidence is the spatial fluctuation of the spacer thickness in non-ideal specimens detailed in reference [76]. Here, the appearance of the spin-wave fluctuations whose impact is to favour perpendicular alignment of the moments. Another mechanism is determined by the electronic structure of an ideal tri-layer system. This has been demonstrated by experiments done on Fe/Al/Fe [75].

Slonczewski [77] proposed a theoretical demonstration of the biquadratic term using a quantum derivation of the indirect exchange between localised spins. Within this model, we assume a migration of the conduction electrons into the spacer layer where they mediate the interaction between the ferromagnets. Hence, an indirect exchange such as RKKY interaction occurs between the magnetic layers due to the concentration of the conduction electrons in the isolating layer. This migration is likely due to the weak exchange energy of the ferromagnets or spin currents.

For a system of two identical ferromagnets separated by a nonmagnetic layer with thickness w shown in figure 3.2, a "*loose*" spin will possess a local-spin Hamiltonian given by the vectorial sum of both exchange fields corresponding to each ferromagnet as[77]:

$$\mathscr{H} = (\mathbf{H}_1 + \mathbf{H}_2) \cdot \widehat{\mathbf{e}}_S, \tag{3.6}$$

where $\widehat{\mathbf{e}}_S$ is the direction of the spin, and $\mathbf{H}_{1,2}$ are the corresponding magnetic fields defined via RKKY interaction as:

$$\begin{aligned} \mathbf{H}_1(z) &= -J_0 \frac{\cos(2k_f z)}{z^2} \mathbf{m}_1 \\ \mathbf{H}_2(z) &= -J_0 \frac{\cos[2k_f(w-z)]}{(w-z)^2} \mathbf{m}_2, \end{aligned} \tag{3.7}$$

where $\mathbf{m_{1,2}}$ are the magnetisations vectors of both ferromagnets, J_0 is a constant which embeds the intrinsic magnetic properties and k_f is the Fermi wave vector detailed later in

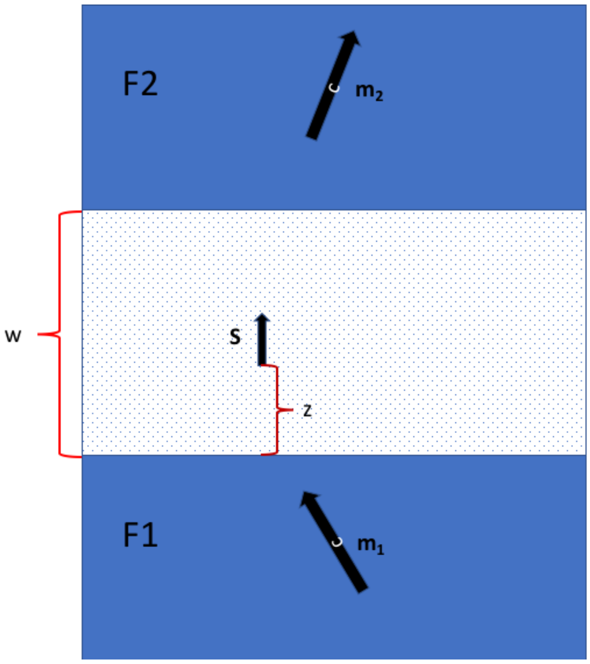

Fig. 3.2 Schematic represantion of the cross section for two semi-infinite ferromagnets F1 and F2 with unit moments $\mathbf{m}_1$ and $\mathbf{m}_2$ separated by a non-magnetic spacer of thickness w.

RKKY chapter. The "*loose*" spin is situated between the magnetic layers at a distance of z from the bottom one (F1) and $w-z$ from the top one (F2). Here, the total exchange between the magnets is expressed as:

$$H(\theta) = \left(H_1^2 + H_2^2 + 2H_1H_2\cos(\theta)\right)^{1/2}. \tag{3.8}$$

Equation (3.8) will give rise to higher-order exchange of the intergranular exchange similar to equation (3.4). The effect of the exchange interaction is given by the additive effect of all spins placed between the ferromagnets. Moreover, the energy per spin at a specific temperature is given by the following equation[77]:

$$f(T,\theta) = -k_BT\ln\left(\frac{\sinh[1+(2s)^{-1}]H(\theta)/k_BT}{\sinh[H(\theta)/2Sk_BT]}\right), \tag{3.9}$$

where s is the quantum spin number. Equation (3.9) is a fundamental equation for developing a theory of inter-granular exchange on thermal fluctuations which can be verified by ASD simulations.

3.3 Tri-layer system

3.3.1 Model of the tri-layer system

In this section, we focus on a particular case of inter-granular exchange interaction in order to reproduce the theoretical and experimental prediction done by Sokalski and Slonczewski aiming to understand atomistically the effects at the nanoscale. To do this, we employed the atomistic spin model described in the methods section in order to model two identical ferromagnets separated by a dilute magnetic oxide layer as shown in figure 3.3. Unlike ECC media, where two ferromagnets are coupled by a direct ferromagnetic coupling, in this model the coupling is made through a non-magnetic oxide layer. To model the exchange across the layer, we create a random distribution of magnetic moments in this space with a ferromagnetic coupling. Hence, we have a disordered magnetic layer which weakly couples the grains depending on the doping density known as magnetic impurities.

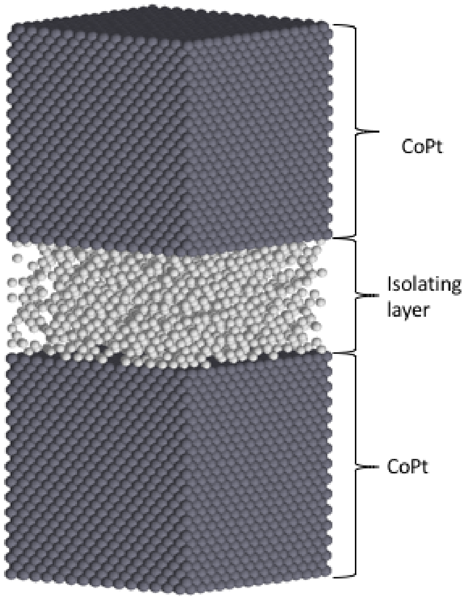

Fig. 3.3 A visualisation of the bilayer system made of two identical ferromagnets separated by a dilute oxide layer with a doping concentration of 30% of magnetic atoms in this case. The width and height of each ferromagnet are 5 nm.

The approach of the simulations is similar to the calculations done by Evans *et al.* presented in reference [78] where the exchange energy of the system has been investigated as a function of the temperature and inter-layer thickness. In contrast with the Evans model, we introduced the uniaxial anisotropy energy contribution into the general Hamiltonian of the system which is defined as:

$$\mathscr{H} = -\sum_{i \neq j} J_{ij} \mathbf{S}_i \cdot \mathbf{S}_j - \sum_i k_u (S_i^z)^2, \tag{3.10}$$

where $J_{ij} = 5.6 \times 10^{-21}\,\mathrm{J/link}$ is the exchange interaction between nearest neighbour site i and j, $k_u = 5.9 \times 10^{-23}\,\mathrm{J/atom}$ is the uniaxial anisotropy constant which gives a macroscopic anisotropy of $6.26 \times 10^6\,\mathrm{J/m^3}$ which is closer to CoPt bulk anisotropy [32]. The atoms are arranged in a FCC structure with an individual magnetic moment of $\mu_s = 1.44\,\mu_\mathrm{B}/\mathrm{atom}$ giving a saturation magnetisation of $6 \times 10^5\,\mathrm{JT^{-1}m^{-3}}$ (A/m) and a lattice parameter $a = 3.54$ Å. All these atomistic parameters are summarized in the table 3.1 below.

Parameter	value
μ_s	1.44 μ_B
J_{ij}	$5.6 \times 10^{-21} J$
k_u	5.9×10^{-23} J/atom
T_C	1280K

Table 3.1 Atomistic parameters used for the bilayer system which corresponds to CoPt with an FCC crystal structure. The lattice constant of this structure is $a = 3.54$Å.

As shown in equation (3.10), we assume the atoms interact directly through the exchange interaction without taking into account the long-range magnetostatic interaction or the indirect exchange. The approach of calculating the exchange energy per site is the nearest neighbours (NN) approximation which preserves the magnetic properties of the exchange interaction.

Although we have a direct exchange between the atoms, the inter-layer coupling is done by direct exchange coupling between CoPt atoms embedded in the diluted layer as shown in figure 3.3 where the density of the atoms can be controlled by randomly removing the desired fraction of atoms from initial FCC crystal structure. In other words, the model of the inter-layer of the isolating layer is to build a similar grain as CoPt grains but instead of having a full FCC crystal structure we remove a significant number of atoms which can be controlled leaving a disordered lattice with vacancies at some atomic sites. This will cause a broken symmetry of the exchange interactions, giving rise to weak coupling depending on the number of missing atoms and the thickness of the inter-layer.

We note that the magnetic impurities have the same properties as the atoms contained by the grains whose magnetic properties have been summarized in the table 3.1.

3.3.2 Calculations of inter-granular exchange of tri-layer system

In the following, we present some calculations done to determine the effective inter-granular exchange between two grains presented in the previous subchapter. The method is similar to that presented in reference [78] which applies a constraint to the bottom grain aiming to retain the domain wall and to vary the axis of the magnetisation for the second ferromagnet.

The calculations are performed using the hybrid-CMC method presented in the methods chapter which allows to apply a constraint force only to a specific grain whereas the others are set to evolve freely. The magnetization of the top ferromagnet is varied sequantally from $+z$-axis to $-z$-axis through 180° with a step of 5°. At each constraint angle, 10,000 CMC steps are performed to equilibrate the system and another 10,000 CMC are performed to calculate the average properties of the system.

The main interest of these simulations is to calculate the exchange energy of a grain during the rotation being in an exchange interaction with its neighbour. Therefore, the bottom layer is considered fixed throughout the switching process of the top layer while the coupling layer is free to respond as the angle of the top layer is varied. We performed, therefore, a series of simulations where the thickness of the interface layer varies from $0.25\,\mathrm{nm}$ to $2.5\,\mathrm{nm}$ this being the range where the effective exchange varies the most. A typical set of calculated torque curves are shown in figure 3.4 for three different thicknesses of the inter-layer. Here, the y-component of the magnetisation is constrained to be zero throughout the switching mechanism resulting in a polar angle θ dependence only. This will lead to the maximum amplitude on y-component of the torque plotted in figure 3.4 where the simulation temperature is $100\,\mathrm{K}$. The torque is normalised to the contact area between the layers.

In the simulations performed by Evans *et al.* [78] there is a strong dependence of the torque on the doping density with a strong influence on the exchange energy scaling. Different doping densities can drastically affect the shape of the dependence of coupling energy on inter-layer thickness given by the Sokalski law. In our simulations, we fixed the concentration of the doping at 30% aiming to find a typical angular dependence of the exchange energy.

As defined, the torque can be calculated as the partial derivative of the Hamiltonian with respect to polar angle θ as:

$$\begin{aligned}\mathscr{T} &= -\frac{\partial \mathscr{H}}{\partial \theta} \\ &= -A\sin(\theta) - 2B\sin(\theta)\cos(\theta),\end{aligned} \tag{3.11}$$

where A represents the magnitude of the exchange energy contribution and B is the anisotropy contribution. This fitting expression works well for higher separations or weak coupling

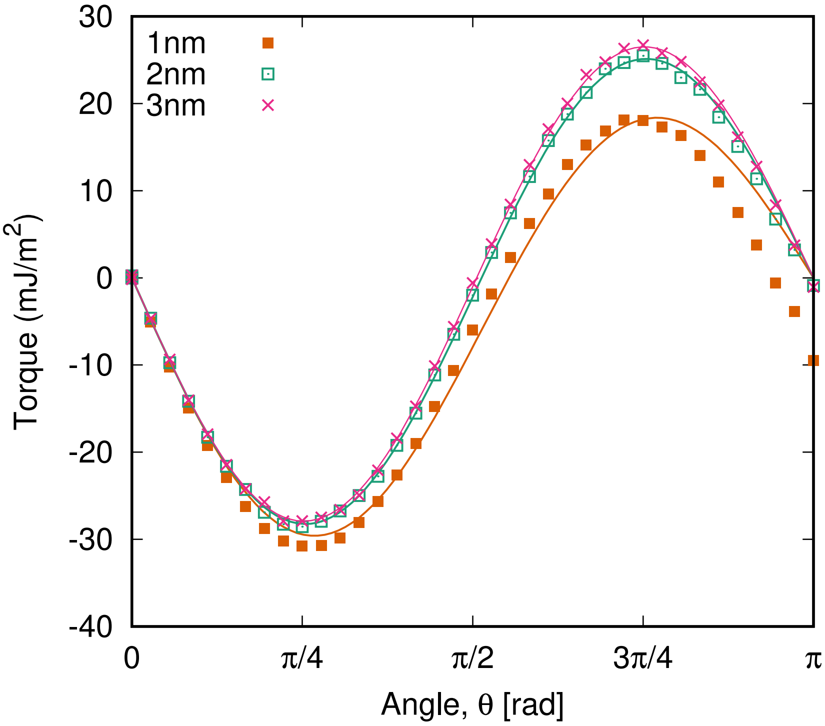

Fig. 3.4 In this figure are plotted calculated restoring torque as a function of the angle between magnetic layers for different inter-layer thicknesses. The simulations are performed at 100K and the doping density of the interlayer is 30%.The solid lines stand for the fit using equation 3.11.

between the layers given by low impurity doping. However, for short distance between ferromagnets this expression breaks down due to a non-uniform configuration of the spins in the top layer at high polar angles.

The non-uniform configuration of the spins leads to nucleation at the interface between the inter-layer and the top layer where the domain wall formation can be observed in figure 3.5 (a) compared with figure 3.5(b). The spin direction is plotted as a function of the system height during the switching mechanism of the top layer as presented in figure 3.5 for a particular inter-layer thickness of 0.15nm shown in figure 3.5(a), respectively 2.5 nm shown in figure 3.5(b). The reduced magnetisation is calculated as $M_z/M_s = \sum_i^N S_z^i$ where $N = 450$ is the total number of atoms in a single atomic layer (mono-layer) and S_z^i is the z-component of the spin direction. Within the coupling layer (inter-layer), N is a statistical variable but can be approximated as 30% of a ferromagnetic atomic layer if the doping constant is set at 30%. A non-uniform direction of the spins can be observed within the top layer especially at higher angles of the magnetisation and low thickness of the inter-layer, where the anti-parallel

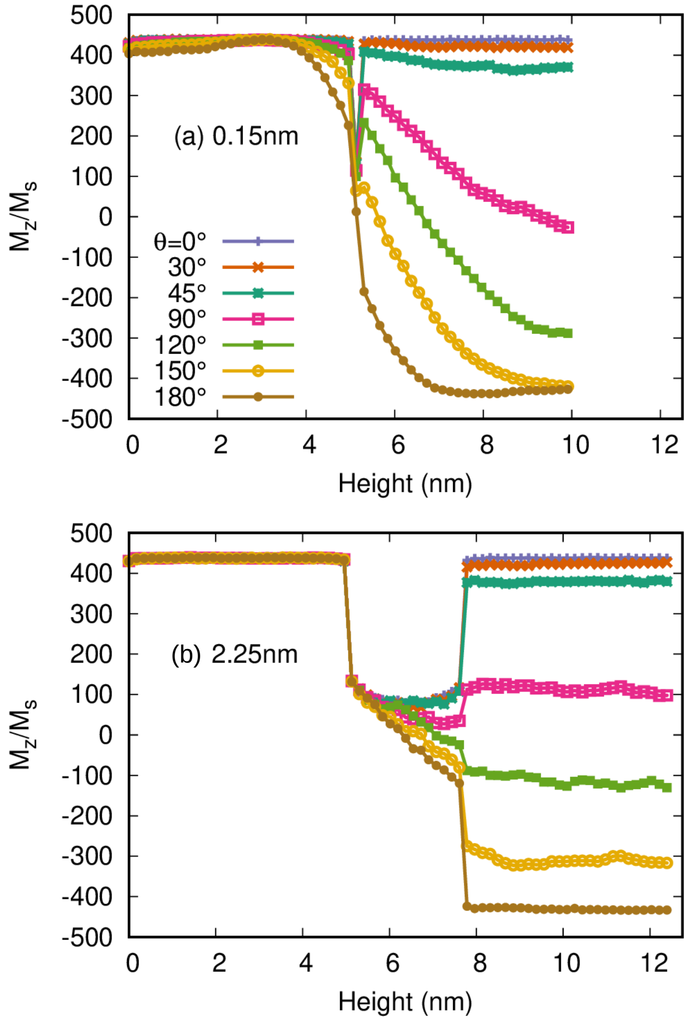

Fig. 3.5 Profile of the magnetisation by averaging the z-component of spins direction for each atomic layer as $M_z/M_s = \sum_i^N S_z^i (N = 450$ atoms per atomic layer) as a function of height of the tri-layer system during the switching mechanism of the top ferromagnet. Each magnetic layer is 5 nm height and the inter-layer has a variable dimension, in these cases (a) 0.15nm and (b) 2.25nm respectively, with a concentration of 30% of magnetic impurities.

orientation of magnetisation vectors effect the energy in such a way that domain wall appears induced by the anisotropy of the bottom grain through the exchange interaction.

Clearly, the expression for the torque curve expressed in equation (3.11) cannot be applicable for strong exchange interaction caused by the small separation. This has great importance in choosing the deposition parameters in order to obtain an optimal distance between the grains.

In non-anisotropy simulations, Evans *et al.* [78] found the bilinear fit appropriate to describe the angular dependence of the torque. However, the contribution of the anisotropy has an impact on the angular dependence which can be described by the additional term corresponding to the anisotropy expressed in equation (3.10). This is very similar to a biquadratic expression due to the $\cos^2$ dependence but no evidence of biquadratic exchange can be found in both cases: anisotropic and non-anisotropic. Therefore, we fit the free energy curves using equation (3.10) in order to find the strength of the exchange energy. Figure 3.6 shows the dependence of the effective exchange coupling as a function of the thickness of the inter-layer. The simulation points have been fitted using the decay law of Sokalski given by equation:

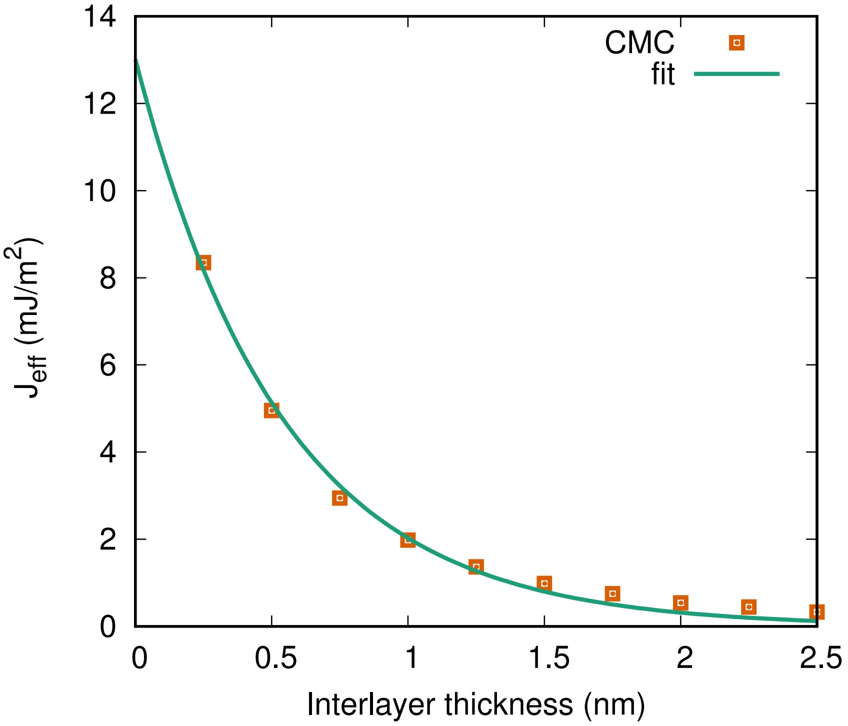

Fig. 3.6 This graph shows the calculated dependence of the effective exchange coupling energy as a function of the inter-layer thickness for a doping density of 30% at 100 K. The solid line represents the fit using the Sokalski law given by equation 3.12.

$$J(x) = J_0 e^{-x/a}, \tag{3.12}$$

where J_0 and a are some arbitrary fitting parameters. For this particular case of 30% doping density, we found a value for $J_0 = 13.01 \times 10^{-21}\,\mathrm{mJ/m^2}$ and $a = 1.85\,\mathrm{nm}^{-1}$. These fitting parameters can vary significantly with the simulation temperature and the doping density. We observed a good agreement of our simulations with experimental measurements done by Sokalski. We note that the angular dependence is well-fitted by the bilinear term only. However, the model results consider only two interacting grains. The more complicated situation of multiple interacting grains is considered in the following section where a significant biquadratic contribution is found.

3.4 Multi-grain system simulations

3.4.1 Model of the hexagonal distribution of CoPt grains

In this section, we propose a more complex model of the granular media to be investigated by creating a structure of seven grains distributed into a hexagonal shape as shown in figure 3.7. Each grain has a regular hexagonal prism shape with a diameter of 5nm and 5nm height separated by a non-magnetic layer in the same manner as in the previous section allowing periodic boundary condition in the z-direction in order to avoid any surface effects. The atomistic parameters of the grains are the same as in the tri-layer system summarized in Table 3.1 with a saturation magnetisation of $M_s = 6 \times 10^5\,\mathrm{A/m}$.

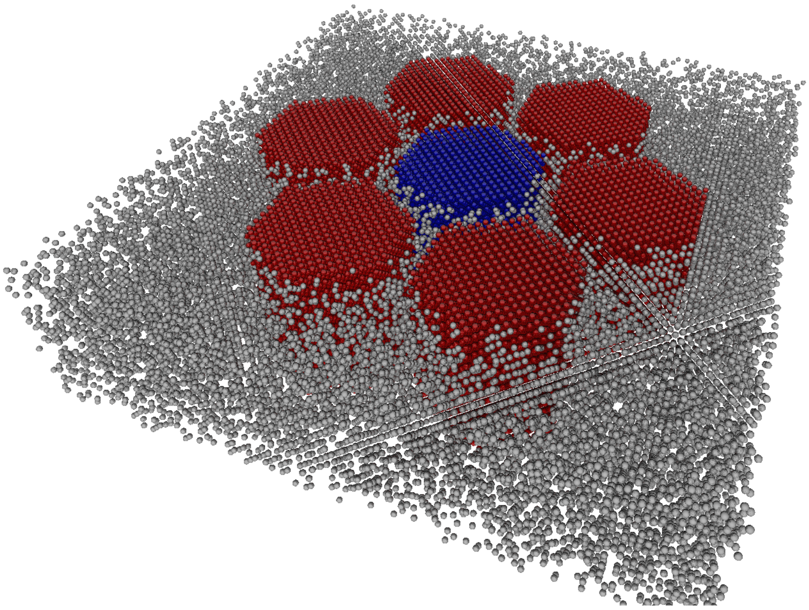

Fig. 3.7 A typical configuration system of the hexagonal distribution of the grains with an inter-layer doping constant of 30%. Each grain is hexagonal-based with a corner-to-corner diameter of 5 nm and 5 nm height.

In this model, we assume a x-z plane rotation of the central grain axis keeping a zero y-component of the magnetisation while the other grains are constrained to remain unreversed throughout the rotation process. Our aim is to find out how neighbours affect this process. Since the distance between the grains and the doping density are important in the decoupling process we perform a systematic investigation by varying the separation and the doping density. In reference [79] is demonstrated experimentally that a grain boundary width around 1nm will lead to a high-density of perpendicular media maintaining high performance of the recording process. Therefore, we set the separation to vary between 0.5nm and 1nm.

3.4.2 Angular dependence of torque

In the following, we present some results of the hexagonal system by computing the torque during the rotation process of the central grain. In the first instance, we are interested to see the exchange energy's behaviour only. Hence, we removed the anisotropy term letting the exchange interaction to be dominant. Although in reality the grain size and the spatial distribution randomly vary, generally being modelled by a Voronoi structure, in this model we assume 7 identical grains placed in such a way they provide a high symmetry as shown in figure 3.8. Despite the high symmetry, at specific polar angles θ different symmetry breaks may occur in the spin configurations.

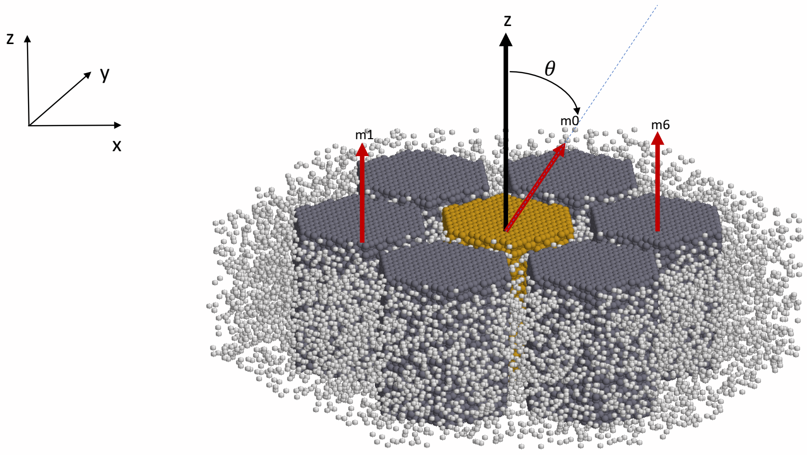

Fig. 3.8 Schematic illustration of a typical rotation process of the central grain. The rotation of the magnetisation axis occurs in $x-z$ plane.

We proceed in a similar way as in the previous subchapter, to find the angular dependence of the torque by performing 10,000 CMC steps to equilibrate and another 10,000 for averaging the magnetic properties at each angle step. Figure 3.9 shows the calculated angular dependence of the central grain for different thicknesses of the inter-layer (a) 0.50nm, (b) 0.75nm and (c) 1.00nm at 200 K, 400 K, respectively 600 K . The torque is normalised to the contact area of the grains which is the sum the six side faces of the grain as $6 \times 5 \times 2.5\text{nm}^3$. In addition to the separation between the grains, we are interested how the temperature decreases the inter-granular exchange by varying the temperature up to the Curie point.

The angular dependence of the torque can be described by two models of the exchange. The first one is given by the bilinear form known as Heisenberg equation expressed in equation 3.2. The bilinear term will give a $\sin(\theta)$ dependence whereas the second model given by the biquadratic model comes with an additional quadratic term from the partial derivative of the biquadratic exchange energy:

$$\begin{aligned} \mathscr{T}_y &= -\frac{\partial \mathscr{H}}{\partial \theta} \\ &= -J_1 \sin(\theta) - 2J_2 \sin(\theta)\cos(\theta), \end{aligned} \tag{3.13}$$

where J_1 is the strength of the bilinear term and J_2 the strength of the biquadratic term.

In figure 3.9 both expressions for the inter-granular exchange interaction have been used for the fitting of the torque angular dependence for the multi-grain system. At smaller separations between the grains and low temperatures, where the coupling is stronger, the peak of the torque is slightly shifted from $\pi/2$ to higher angles. The Heisenberg model predicts the minimum at $\pi/2$, whereas the biquadratic model gives a more accurate fit according to our results presented in figure 3.9 for low temperatures such as 200K represented by the points with square shape.

Overall, the inclusion of the biquadratic term gives the best fit, although the fit is poor for the lowest inter-granular layer thickness shown in figure 3.9(a). As it was discussed in the introduction the origin of biquadratic exchange energy can have multiple reasons but in this computational model, we relate this behaviour to inhomogeneous rotation of the spins caused by a random distribution of the impurities in the inter-layer leading to a dispersion of the local exchange.

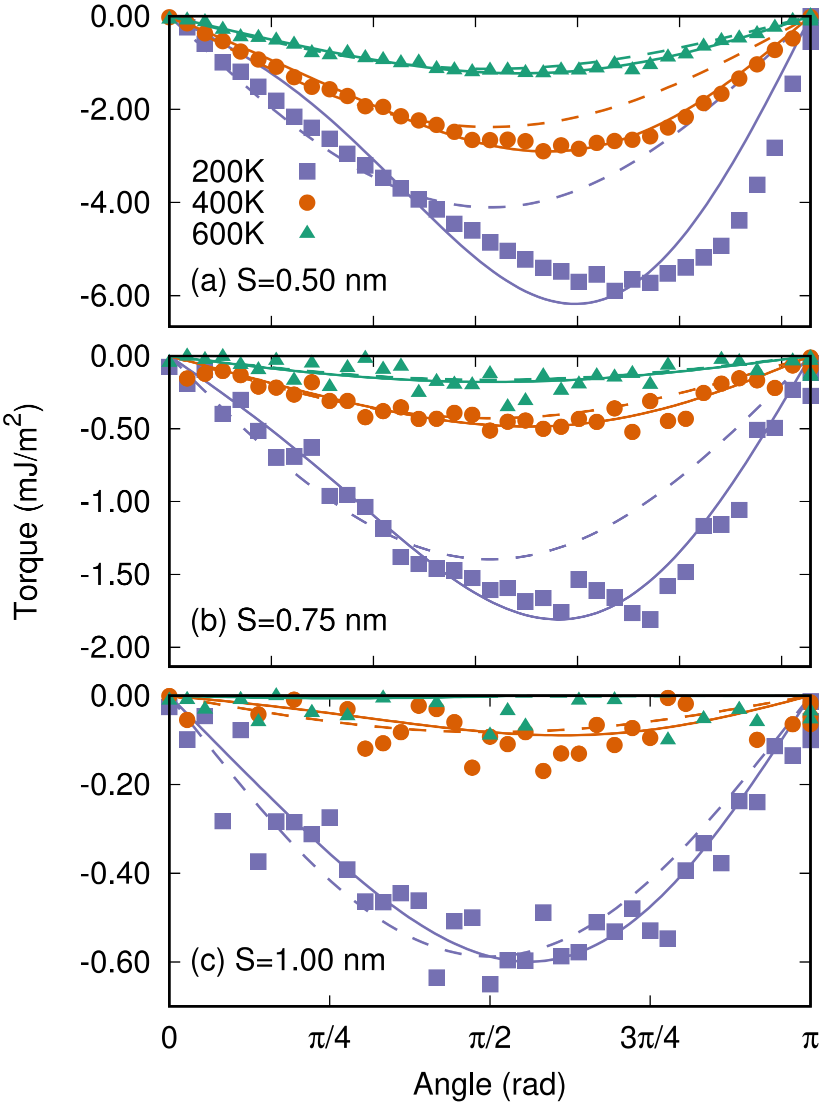

Fig. 3.9 The angular dependence of the torque acting on the central grain for three different separations of the inter-layer (a) 0.50nm, (b) 0.75 nm, and (c) 1.00nm respectively. The doping density of the inter-layer is set at 20%. The dashed line is the fit using Heisenberg model expressed in equation (3.2) whereas the solid lines represent the fit using biquadratic exchange given by the equation (3.13).

3.4.3 Dependence of inter-granular exchange on separation, doping rate and temperature

The combination of biquadratic and bilinear terms expressed in equation (3.13) describes very well the angular dependence of the torque in the low density regime and high temperatures above 300 K of interest for HAMR. To have a clear dependence of the effective exchange energy on the temperature at different separations and densities in low regime, we extracted the bilinear exchange constant J_1 and the biquadratic constant J_2 through the fitting of the torque curves using equation (3.13). Figure 3.10 shows the temperature dependence of the effective exchange which can be expressed in terms of exchange field using

$$H_{\text{exch}} = J_{\text{eff}}/M_s^0 V, \tag{3.14}$$

where J_{eff} is the effective exchange constant normalised to the contact area of the grains A and V is the volume. The saturation magnetisation is the same as in the tri-layer system $M_s^0 = 6 \times 10^5\,\text{A/m}$.

Although we have a higher-order exchange, there is a clear exponential decay of the effective exchange with the temperature for both bilinear and biquadratic exchange constants being consistent with the Slonczewski model for the biquadratic and the calculations of Evans *et al.* for the bilinear term. Both bilinear and biquadratic exchange constants follow the power law shown in equation (3.5) but we noticed a faster decay of the biquadratic term with the temperature. In addition to this, we found a scaling of the exponent, α, with the density and the separation distance between the grains suggested by the different shape of the dependences shown in figure 3.10.

By taking into account the variation of the exponent with density and temperature the power law of the effective exchange must be re-written as:

$$J_{\text{eff}}(T,d,s) = J_0 \left(1 - \frac{T}{T_C}\right)^{\beta(d,s)}, \tag{3.15}$$

where d is the density of the inter-layer magnetic impurities and s is the separation between the grains. Now the effective exchange is a three-variable function. Besides the thermal exponential reduction, the separation and density also play a role in the strength of the exchange. To show this, we plotted the dependence of the effective exchange energy as a function of the inter-layer thickness shown in figure 3.11.

We studied both cases with and without anisotropy given by the solid and empty symbols respectively. In both cases, we noted a similar decrease of the exchange energy with an increased inter-layer thickness at different densities. However, in the low regime of density such as 20% for example, we identify a difference of the exchange energy with and without anisotropy. This is related to a preferential direction of the spins to align, however at higher concentration of the impurities, we cannot identify a notable difference between these two cases. These calculated points have been plotted using an exponential law similar with

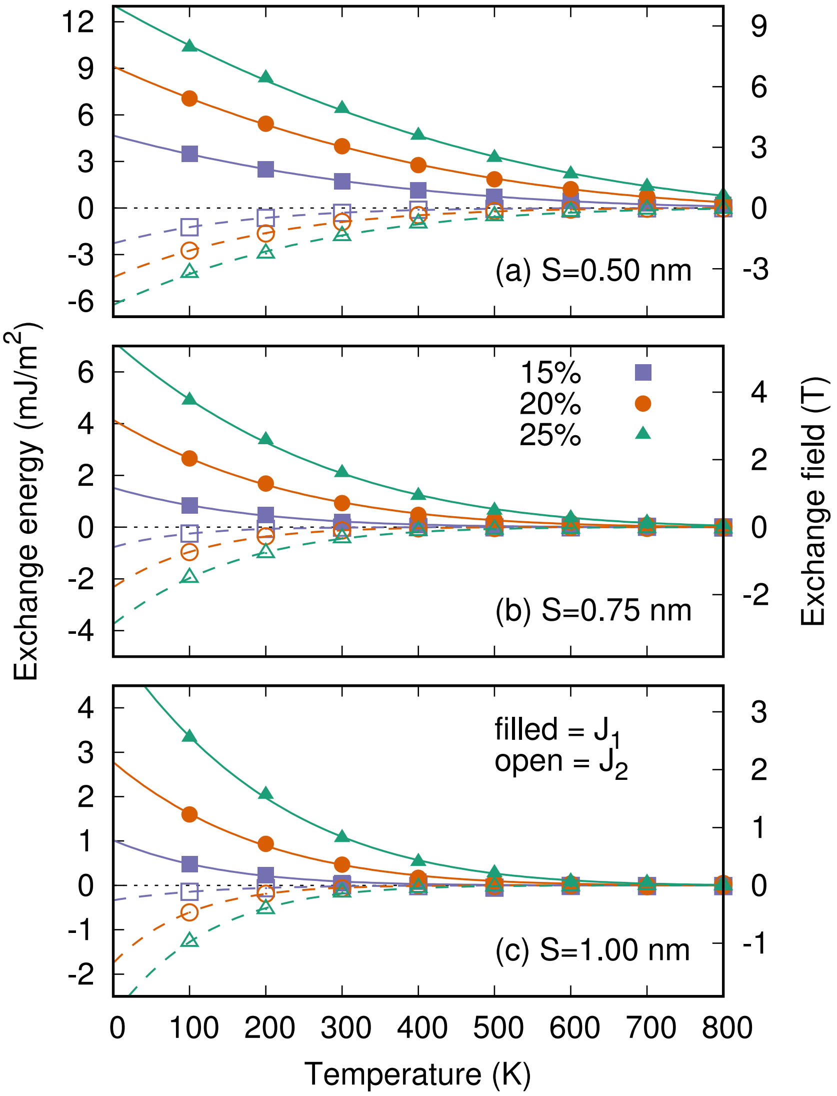

Fig. 3.10 In this graph is plotted the temperature dependence of the effective inter-granular exchange for three different separation distances (a) 0.5nm, (b) 0.75nm, and (c) 1.00nm at lower density of the magnetic impurities. The bilinear exchange constant J_1 is shown in filled points and the biquadratic J_2 is shown in open points. J_1 points have been fitted using equation (3.15)

Sokalski law expressed in following equation:

$$J_{\text{eff}} = J_0 e^{-k/s}, \tag{3.16}$$

where k is a fitting constant and s is the separation between the grains. Therefore, we are entitled to postulate based on our calculation that the exchange energy strongly depends on

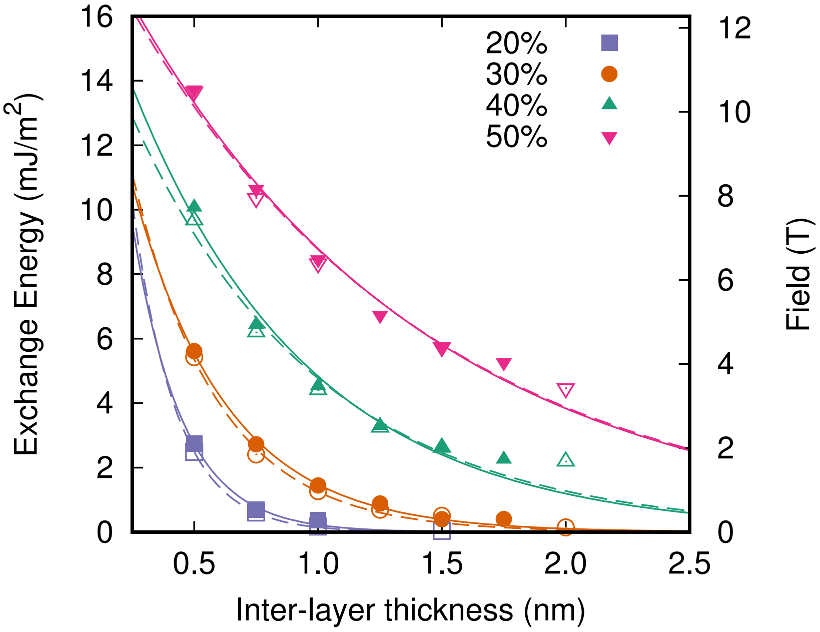

Fig. 3.11 In this graph is plotted the dependence of the inter-granular exchange as a function of the inter-layer thickness at 300K. The open and closed points represent with and without anisotropy values. The density varies between 20% and 50% whereas the temperature is fixed at 300K. The solid lines shows the fit using an exponential law given in equation (3.16).

the temperature, density, and separation. By combining equation (3.15) with equation (3.16) we can write a unified equation for the inter-granular exchange energy as:

$$J_{\text{eff}}(T,d,s) = J_0 \left(1 - \frac{T}{T_C}\right)^{\beta(d,s)} e^{-\frac{k(d)}{s}}. \tag{3.17}$$

In the following, we simulate a scenario where the central grain is at the boundary between two written bits of information, by setting 3 neighbours aligned to $+z$ direction and the other 3 switched to $-z$ direction as shown in the inset of figure 3.12. In this scenario the bilinear term of the exchange is influenced by two terms which are in opposition where the biquadratic term is additive. Hence, the energy can be expressed similarly to equation (3.13) where $J_1 = J_1^{\text{up}} - J_1^{\text{down}}$ is a result of the difference between the exchange with the neighbours aligned "up" and the exchange with the switched neighbours. Again, the torque curves are fitted using equation (3.13) giving accurate results for low densities. At higher values of density the fit does not match exactly with the calculated points but it provides a good qualitative description of the model. A notable effect of high density is the non-minimum energy at $\theta = \pi$ resulting in an antisymmetric curve of the free energy. This explains local dispersion of exchange coupling analoguous to the effect described by Slonczewski in interface roughness effects.

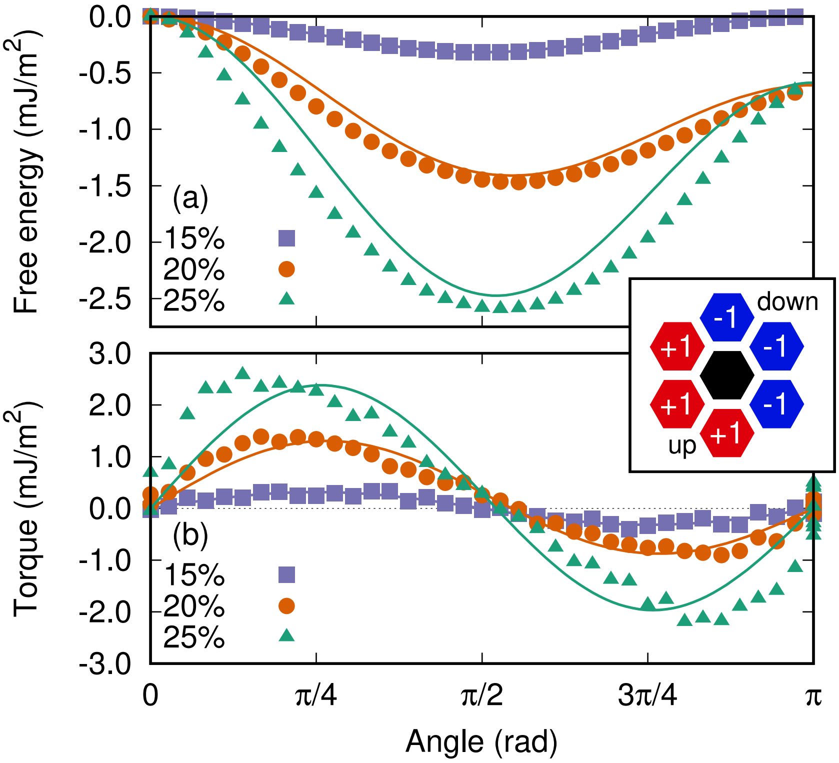

Fig. 3.12 The angular dependence of the free energy shown in panel (a) and the torque shown in panel (b) acting on central grain when it has 3 neighbours constrained with $m_z = +1$ and 3 neighbours with $m_z = -1$ for 15%, 20%, and 25% at 300K.

3.5 Conclusions and further work

To summarise, in this chapter we investigated in detail the inter-granular exchange energy by employing the Atomistic Spin model using CMC simulations. Our results for a tri-layer system are in strong agreement with the experimental results done by Sokalski *et al.*, demonstrating again an exponential decrease with the separation between the grains. This has been also demonstrated by Evans *et al.* for anisotropic simulations but the exchange is affected in a similar way in the anisotropy case despite the alignment preference given by the anisotropy field.

In a more complex system the macroscopic Heisenberg exchange model is not sufficient to describe the angular variation of torque, this being demonstrated atomistically in our simulations. A theoretical and experimental support for higher order exchange is given by Slonczewski by introducing an additional higher order term in the exchange form of the energy for multi-layers system called biquadratic exchange term. In fact, the Slonczewski model is an extended Heisenberg model with an additional higher order term, denoted by the biquadratic term. We identified this term in our calculations shifting the angular dependence of the torque curves.

Further simulations can be performed to investigate a more complex structure such as an arrangement of five ECC media grains illustrated in figure 3.13. We consider the ECC media grain as an improvement of CoPt grain used for current simulations, but this comes with additional effects such as different modes of nucleations which might be affected by the inter-granular exchange. The biquadratic and the nucleation effects can effect not only the recording process performance but also the long-term stability. The way that these can affect the recording process is unknown for the moment but investigation of energy barrier would give more information about the long-term stability.

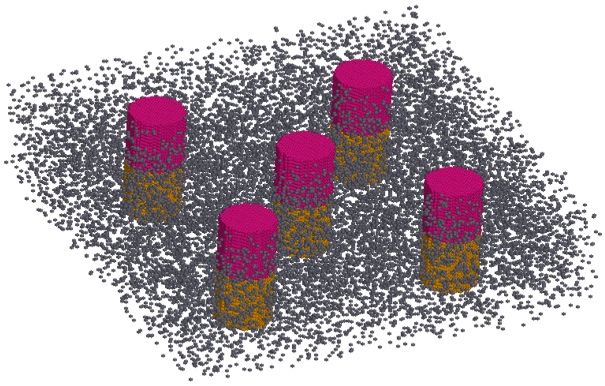

Fig. 3.13 A visualisation of a complex structure of 5 ECC grains coupled by a non-magnetic layer with a doping density of 15%.

Chapter 4

Atomistic simulations of exchange-coupled composite (ECC) media

In the previous chapter the exchange interaction between magnetic grains has been investigated showing the dependence of the inter-granular exchange in different parameters. The aim of the current chapter is to carry out a detailed study of exchange interactions within a new design of the grains for recording media. Here, a combination of two magnetic phases linked by a ferromagnetic coupling generically called exchange coupled composite media will be simulated in order to understand the role of the exchange within the layers and the intralayer coupling. A particular aspect of the exchange has been observed in exchange-coupled composites (ECC) specifically exchange spring behaviour has been investigated as a function of temperature, applied field strength, exchange coupling at the interface and the damping constant. We report a faster decrease of the energy barrier of ECC media than previous theoretical prediction which might be related to the nucleation which strongly depends on the static properties of the materials such as thickness, anisotropy energy and exchange stiffness and also the characteristics which determine the dynamics such as the damping constant, temperature and others. We found an anomalous damping dependence of the switching time for higher regime damping of the soft phase as a result of the nucleation which is pinned at the interface. However, at higher values of the applied field, the switching time dependence is more consistent to theoretical predictions.

4.1 Introduction

Magnetic recording has been extensively studied in order to increase the areal density of the grains in the last few decades by reducing the grain size. This problem becomes more challenging as it is necessary to maintain a high signal-to-noise ratio (SNR) where the grain dimensions effect the strength of the SNR according to equation (4.1) as shown in reference [80]

$$S/N \approx \frac{1}{\left[< D >^3 \left(1 + \left(\frac{\sigma}{D}\right)^2\right)\right]}, \tag{4.1}$$

where D is the grain size and σ is the grain size distribution. Another important aspect of recording is related to thermal stability which can be achieved with high magneto-crystalline anisotropy which implies a larger magnetic field to switch the magnetisation. This has been formalized in the magnetic *trilemma* according to Richter *et al.* [81]. Several technologies have been proposed to solve the *trilemma* of magnetic recording such as patterned media[82] and heat assisted magnetic recording (HAMR) [83] with a new perspective of media design. In addition, by using ECC media design one can anticipate good performance beyond 1Tb/in^2 as it is reported in reference [84].

HAMR uses a laser pulse to heat locally the grain in order to reduce the magnetic anisotropy thereby allowing the magnetisation to switch ensuring optimal thermal stability after the system is cooled back to ambient temperature. This approach presents some thermal limits suggested by Suess *et al.* [85] which consists in thermal errors induced by heating known as thermal jitter. This problem has been previously theoretically studied by Evans *et al.* [86] who identified the *quadrilemma* of heat assisted magnetic recording to understand how temperature affects the writing process detailed in the introduction chapter of this thesis.

A solution to this is a combination of hard and soft magnetic phase proposed by Suess and Schrefl [87] with different Curie temperatures in order to improve the writing process by avoiding thermal errors which might occur. Here, the relation which describes the rate of errors during the writing process can be expressed as:

$$\mathrm{BER} = \exp\left(-\frac{2J_S(T_{\mathrm{wr}})VH_{\mathrm{wr}}}{k_B T_{\mathrm{wr}}}\right), \tag{4.2}$$

where T_{wr} and H_{wr} are the temperature and the strength of the magnetic field during the recording process. J_S is the magnetic polarization which also depends on temperature and

Curie temperature as follows:

$$J_S(T) = J_S(T_0)\sqrt{\left[1 - \left(\frac{T}{T_C}\right)^{\alpha}\right]^{\beta}}, \tag{4.3}$$

where $J_S(T_0) =$ is the polarization at zero Kelvin and T_C is the Curie temperature of the magnetic material. Equation (4.2) shows an exponential decrease of the bit errors rate with higher writing temperatures, where an increased polarization $J_S(T_{wr})$ and stronger fields H_{wr} will result in a more accurate writing process. Therefore, high T_C materials are required for this process in order to increase the polarization at elevated temperatures according to equation (4.3). L1$_0$ FePt, however cannot offer sufficient saturation magnetisation and high Curie temperature. Consequently, an additional soft phase such as Fe is preferred to counterbalance the M_S needed and to increase the average magnetic polarization of the composite.

Another major benefit of ECC media is represented by the exchange spring effect [88, 89] which allows to reduce the writing field according to the following equation [90]:

$$H_{\mathrm{wr}} = \frac{K_{u,\mathrm{hard}} \cdot t_{\mathrm{hard}} + K_{u,\mathrm{soft}} \cdot t_{\mathrm{soft}}}{M_{S,\mathrm{hard}} \cdot t_{\mathrm{hard}} + M_{S,\mathrm{soft}} \cdot t_{\mathrm{soft}}}, \tag{4.4}$$

where $K_{u,\mathrm{hard}}$ and $K_{u,\mathrm{soft}}$ are the perpendicular anisotropy of hard, respectively soft phase, M_S is the saturation corresponding to each phase, and t_{hard}, t_{soft} are the thickness of hard/soft layers. Due to a small anisotropy of the soft layer $(K_{u,\mathrm{soft}} \ll K_{u,\mathrm{hard}})$, equation (4.4) can be approximated with:

$$H_{\mathrm{wr}} \approx \frac{K_{u,\mathrm{hard}} \cdot t_{\mathrm{hard}}}{M_{S,\mathrm{hard}} \cdot t_{\mathrm{hard}} + M_{S,\mathrm{soft}} \cdot t_{\mathrm{soft}}}. \tag{4.5}$$

Equation (4.5) shows a clear reduction of the field required for writing process. This represents an ideal case when the nucleation effects do not occur and it can be achieved with graded media. However, the writing field strongly depends on the nucleation field. In reference [91] is shown that at specific thicknesses of the soft layer the nucleation is formed in the soft phase, followed by a propagation towards the interface where is pinned. The equation which predicts the writing field is expressed as [91]:

$$H_{\mathrm{wr}} = \max(H_{\mathrm{pin}}, H_{\mathrm{n}}), \tag{4.6}$$

where H_{pin} and H_{n} are the pinning field, respectively nucleation field. Here, an optimal thickness of the soft layer should be equal to hard phase thickness which reduces the writing field by a factor of 5.

On following, we employed the atomistic spin model in order to simulate the behaviour of the exchange spring within ECC media. Unlike micromagnetic models, the atomistic model confers the possibility to understand different behaviours of the exchange spring on different parameters such as temperature and damping constant of the materials by simulating the magnetisation at atomistic scale.

4.2 Atomistic properties of ECC media

4.2.1 Theoretical Fe/FePt bilayer model

In this section we present an atomistic model of a new design proposed for heat assisted magnetic recording (HAMR) in order to extend the thermodynamic limits of recording media. A bi-layer system which comprises a hard magnetic phase such as FePt with large perpendicular anisotropy linked by ferromagnetic exchange to an Fe phase with high M_S.

$$\begin{aligned}\mathscr{H} = &-\sum_{i,j} J_{ij}^{\text{Fe}}\mathbf{S}_i^{\text{Fe}}\cdot\mathbf{S}_j^{\text{Fe}} - \sum_i k_u^{\text{Fe}}(S_{iz}^{\text{Fe}})^2\\ &-\sum_{i,j} J_{ij}^{\text{FePt}}\mathbf{S}_i^{\text{FePt}}\cdot\mathbf{S}_j^{\text{FePt}} - \sum_i k_u^{\text{FePt}}(S_{iz}^{\text{FePt}})^2\\ &-\sum_{i,j} J_{ij}^{\text{int}}\mathbf{S}_i^{\text{Fe}}\cdot\mathbf{S}_j^{\text{FePt}} - \sum_i \mu_0\mu_i\mathbf{S}_i\cdot\mathbf{H}_{\text{app}}.\end{aligned} \tag{4.7}$$

The general form of the Hamiltonian can be seen in equation (4.7) which arises from an extended Heisenberg Hamiltonian excluding the magnetostatic energy since the behaviour of the system is dominated by the anisotropy. This includes six terms where three of them represents the inter-layer and intra-layer exchange energies. The other two represent the anisotropy energy contribution from Fe and FePt and the last term corresponds to the Zeeman energy in the presence of an external magnetic field.

In equation (4.7) the spins are represented as unit vectors, $\mathbf{S}_i$ with the magnitude of the magnetic moment given by μ_i and μ_0 is the permeability of free space. J_{ij} represents the exchange coupling which is restricted to the nearest neighbours in order to speed up the calculations. Here, the spin index i varies between 1 and N-total number of the spins and j varies between 1 and total number of NN which are interacting with any given spin i.

Parameter	Fe	FePt
J_{ij}	$7.05 \times 10^{-21}\,\mathrm{J/link}$	$4.5 \times 10^{-21}\,\mathrm{J/link}$
k_u	$5.25 \times 10^{-25}\,\mathrm{J}$	$2.2 \times 10^{-22}\,\mathrm{J}$
μ_s	$2.22\,\mu_\mathrm{B}$	$1.9\,\mu_\mathrm{B}$
a	$3.249\,\mathrm{\AA}$	$3.249\,\mathrm{\AA}$
Lattice	bcc	bcc
J_{ij}^{int}	$1.5 \times 10^{-21}\,\mathrm{J}$	

Table 4.1 Atomistic parameters of Fe and FePt in both cases isolated and interacting through the J_{ij} interface.

We distinguish three types of exchange couplings: J_{ij}^{Fe} which is the exchange constant between Fe atoms, J_{ij}^{FePt} representing the exchange constant between hybrid FePt atoms which represents a single type of atoms which combines both properties of Fe and Pt, respectively J_{ij}^{int}-the exchange between Fe and hybrid FePt atoms at the interface. Most of the parameters come from experimental results and first principle calculations summarized in Table 4.1. For Fe the exchange value is $J_{ij}^{\mathrm{Fe}} = 7.05 \times 10^{-21}\,\mathrm{J}$ [92] which corresponds to high T_C of 1050 K close to experiment [93] whereas for FePt the exchange constant is $J_{ij}^{\mathrm{FePt}} = 4.5 \times 10^{-21}\,\mathrm{J}$. The interfacial exchange can vary depending on the ferromagnetic nature of the interfacial layer. In this model we consider a direct coupling between the hybrid FePt atoms and Fe atoms.

The magnetic moment of Fe is taken as $2.2\,\mu_\mathrm{B}/\mathrm{atom}$ which gives a macroscopic value of M_S of $1184\,\mathrm{emu/cc}$ and FePt has been investigated by Aas *et al* [92] using ab-initio calculations, finding an effective Fe moment of $2.86\,\mu_\mathrm{B}/\mathrm{atom}$ and $0.36\,\mu_\mathrm{B}/\mathrm{atom}$ for Pt for bulk value. In this chapter the sizes of the simulated grain are relatively small where the magnitude of Fe moment drops substantially at the margins or at the interface according to first principle calculations, therefore we restricted FePt moments at $1.9\,\mu_\mathrm{B}/\mathrm{atom}$ which corresponds to a macroscopic saturation of $1024\,\mathrm{emu/cc}$.

In reference [94] it is found that the large anisotropy of FePt ($K \approx 10^7$ erg/cc [95]) arises from the hybridization of the Fe and Pt orbitals. Mryasov *et al.* proposed a spin Hamiltonian which incorporates long-range exchange interactions and anisotropy contributions from single- and two-ion terms. For computational efficiency here we use an equivalent nearest neighbor exchange and a single ion uniaxial form for the anisotropy of FePt with an atomistic anisotropy constant of $k_u^{FePt} = 2.2 \times 10^{-22}\,\mathrm{J}$ and $k_u^{Fe} = 5.65 \times 10^{-25}\,\mathrm{J}$ for Fe arranged in a body-centred cubic (BCC) structure with a lattice parameter equal to 3.249 Å for FePt.

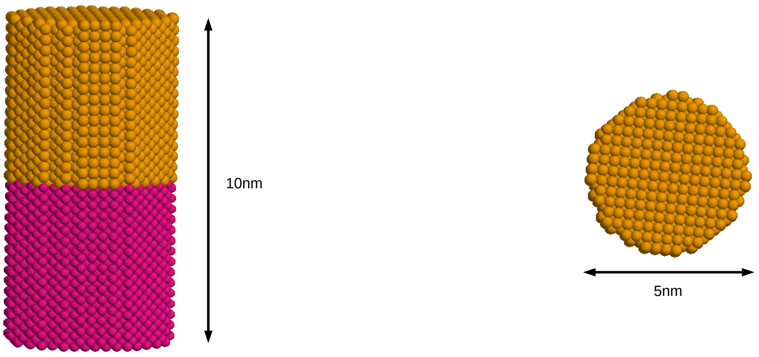

(a) (b)

Fig. 4.1 A 3D image of exchange-coupled composite (ECC) media. Figure (a) shows a profile picture of the grain which comprises two magnetic phases suggested by different colors. The magenta color on the bottom of the grain represents FePt with 5nm height and the yellow color represents the soft Fe phase. On image (b) it is illustrated a top view of the ECC grain.

Figure 4.1 illustrates a 3D picture of the exchange composite having a cylindrical geometry. This has been set at 10 nm height with a basal diameter of 5 nm. The magenta color indicates the hard phase (FePt) and yellow the soft phase (Fe). The crystal order of both phases is (BCC) with a separation distance of 3.249 Å giving 185 atoms per each mono layer.

4.2.2 Equilibrium properties of ECC media

In this section we simulated the fundamental magnetic properties of ECC media by using Monte-Carlo and Constrained Monte-Carlo methods described in the previous chapter. We started to investigate the dependence of spontaneous magnetisation of the composite on temperature. Spontaneous magnetisation of ECC media at certain temperature has a significant importance in simulations, particularly the shape of dependence M_S vs. T. The simplest model which describes this dependence is the classical fit expression $M(T) = (1-T/T_C)^{\beta}$ where $\beta = 1/3$ is the classical exponent. This expression works reasonably well for many magnetic materials demonstrated in reference [96]. However, not all materials can be described by this equation, Fe for example which is in our consideration for ECC design. Measurements of the magnetisation of Fe show a difference comparing with classical Heisenberg function, thus a new function was proposed by Kuz'min [97] expressed as:

$$M(T)/M_0 = \left[1 - s\left(\frac{T}{T_C}\right)^{3/2} - (1-s)\left(\frac{T}{T_C}\right)^{p}\right]^{\beta}, \tag{4.8}$$

where M_0 is the saturation magnetisation at zero Kelvin, s and p are arbitrary fitting parameters. For most materials it was found that $p = 5/2$ apart from Fe. Both the classical and Kuz'min functions give the correct form of $M(T)$ for wide range of materials but unlike classical Kuz'min gives a correct shape of the dependence. Evans *et al.* [3] demonstrated that equation (4.8) can be approximated with equation (4.9) in order to reproduce the experimental curve of $M(T)$.

$$M(T) = M_0 [1 - (T/T_C)^{\alpha}]^{\beta} \tag{4.9}$$

where α can be extracted after fitting the experimental results. This simplified function can ensure a correct form of $M(T)$. In our simulations this new function has been implemented by rescaling the temperature using α from experiment as:

$$\frac{T_{\mathrm{sim}}}{T_C} = \left(\frac{T_{\mathrm{exp}}}{T_C}\right)^{\alpha} \tag{4.10}$$

This will result in a rescaling of the magnetisation length in a such way that it will be the same as in experiment for a certain value of simulation temperature. In other words, for a specific temepratrure in experiment T_{exp} the simulation will use a rescaled temperature according to equation (4.10). In order to construct a reliable model of the temperature dependence for Fe we introduce figure 4.2 from reference [3] where the magnetisation has been calculated using Monte-Carlo calculations and averaging 20,000 integration steps per each simulation point on the graph.

In figure 4.2 we distinguish two cases of temperature simulation: first corresponding to classical model where $\alpha = 1$. The dark points show the simulated points of magnetisation whereas the line is the fit following equation (4.9) when $\alpha = 1.0$. The second case corresponds to the rescaled temperature according to equation (4.10) where the solid line is the experimental data fit and the triangles represents the simulated values of the magnetisation. The α for Fe is found to be 2.8 for Fe after the fit of the experiment. A discrepancy of the magnetisation is found between these two cases particularly at conventional temperatures where HAMR technology works. Therefore, this rescaling function will be used in our further simulations both for equilibrium properties and dynamics of the ECC media. FePt on the other hand is more close to classical but a factor of $\alpha = 1.5$ will be applied in order to get closer to experiment[98].

Figure 4.3 shows simulated $M(T)$ curves for Fe, and FePt respetively using the same approach as in figure 4.2 by averaging 10,000 Monte-Carlo steps per each simulated point.

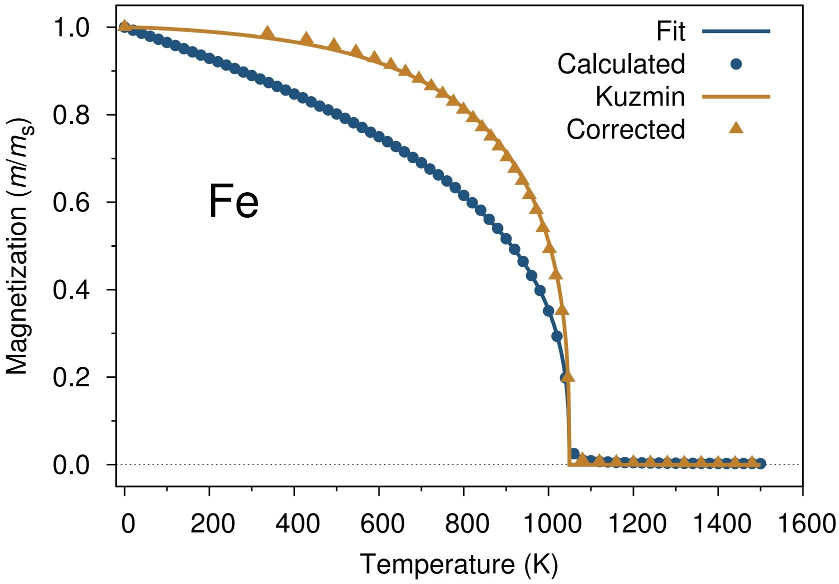

Fig. 4.2 Temperature-dependent magnetisation for Fe. The dark line represents the fit for the classical case when $\alpha = 1$ whereas the light line is the fit using equation for the experimental results. The light triangles represent the simulated data after the rescaling law was applied. The experimental fitting parameter α is found to be 2.86. This graph has been taken from Evans *et al.* [3].

Both layers have been simulated in interaction coupled by a ferromagnetic exchange coupling of $J_{\text{int}} = 3 \times 10^{-21}$ J with the same parameters presented in table 4.1. We obtained a similar dependence as in figure 4.2 for Fe. The Curie temperature has been extracted by fitting the simulation points using equation (4.9) giving a Curie temperature value for Fe of 1050 K and 700 K for FePt which are in quantitative agreement with experimental measurements which validates the model for calculations at the atomistic scale.

We can now proceed to calculate static and dynamic properties using the atomistic model. First we investigate the energy barrier of the ECC medium, and its temperature dependence using the constrained MC model. Due to the constraint the magnetisation is out of equilibrium resulting in a torque. By definition the torque can be calculated as a cross product between the magnetisation and the effective magnetic field as:

$$\mathscr{T} = -\mu_s^i \sum_i \mathbf{S}_i \times \mathbf{H}_{\text{eff}}^i. \tag{4.11}$$

First, we need to investigate the torque energy of the composite during a rotation of the magnetisation axis of 180° from aligned spins on easy axis to anti-parallel state.

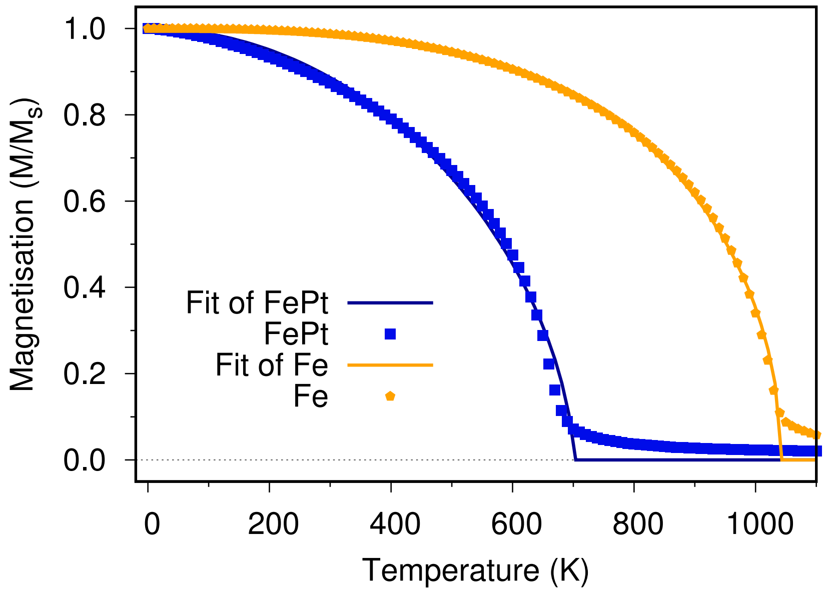

Fig. 4.3 In this graph is plotted the temperature-dependent magnetisation for Fe and FePt. The fit is represented by the solid lines using the equation: $m(T) = [1 - (T/T_C)^{\alpha}]^{\beta}$ according to equation (4.9). After the fit a value of Curie temperature of 1050 K for Fe and 700 for FePt have been extracted. The experimental exponent α is 2.8 for Fe and 1.5 for FePt.

For analysis of the numerical data, it is useful to have a simple analytical benchmark for the torque assuming coherent rotation. Deviations from the simplified approach will indicate the onset of non-uniform rotation. Such an expression can be derived from the equation of the total energy of the system expressed in equation (4.7) as:

$$|\mathscr{T}| = -\frac{d\mathscr{H}_{\mathrm{ECC}}}{d\theta}, \tag{4.12}$$

where θ is the polar angle of the magnetisation with respect to the easy axis. $\mathscr{H}_{\mathrm{ECC}}$ is the hamiltonian of ECC media expressed in equation (4.7). Hence, equation (4.12) can be expanded as:

$$
\begin{aligned}
|\mathscr{T}| = \frac{d}{d\theta}&\left[\underbrace{\sum_{i,j} J_{ij}^{\mathrm{Fe}}\mathbf{S}_i^{\mathrm{Fe}}\cdot\mathbf{S}_j^{\mathrm{Fe}} + \sum_{i,j} J_{ij}^{\mathrm{FePt}}\mathbf{S}_i^{\mathrm{FePt}}\cdot\mathbf{S}_j^{\mathrm{FePt}} + \sum_{i,j} J_{ij}^{\mathrm{int}}\mathbf{S}_i^{\mathrm{Fe}}\cdot\mathbf{S}_j^{\mathrm{FePt}}}_{\mathscr{H}_{\mathrm{ex}}}\right] + \\
\frac{d}{d\theta}&\left[\underbrace{\sum_i k_u^{\mathrm{Fe}}(S_{iz}^{\mathrm{Fe}})^2 + \sum_i k_u^{\mathrm{FePt}}(S_{iz}^{\mathrm{FePt}})^2}_{\mathscr{H}_{\mathrm{ani}}} + \sum_i \mu_0\mu_i\mathbf{S}_i\cdot\mathbf{H}_{\mathrm{app}}\right]
\end{aligned}
\tag{4.13}
$$

Since $\mathscr{H}_{\mathrm{ani}}^{Fe} \ll \mathscr{H}_{\mathrm{ani}}^{FePt}$ this can be neglected in the total torque. It is possible that under certain circumstances a domain wall can be introduced, which is not taken into account in the current analysis. By developing equation (4.13) for an external magnetic field along $+z$ direction, we can obtain following fit expression for the torque curve as:

$$
\begin{aligned}
|\mathscr{T}(\theta_i)| &= A_{\mathrm{ex}}(\theta_i) + \frac{d}{d\theta_i}\left[\sum_i k_u^{\mathrm{FePt}}(S_i^{\mathrm{FePt}})^2\cos(\theta_i)^2 + \sum_i \mu_0\mu_i S_i\cdot H_{\mathrm{app}}\cos(\theta_i)\right] \\
&= A_{\mathrm{ex}}(\theta_i) - 2\sum_i k_u^{\mathrm{FePt}}(S_i^{\mathrm{FePt}})^2\sin(\theta_i)\cos(\theta_i) + \sum_i \mu_0\mu_i S_i\cdot H_{\mathrm{app}}\sin(\theta_i).
\end{aligned}
\tag{4.14}
$$

We can be identify two types of rotation: first when the rotation is coherent without any nucleation or domain wall formation during the reversal process and the second when nucleation or domain wall can occur. Within coherent rotation the expression of torque can be simplified due to a non variation of exchange term A_{ex} with angle as long all the spins are parallel to magnetisation axis $(\theta_{i-1} = \theta_i = \theta_{i+1} = \theta)$. Here, the exchange term can be approximated with a constant and the torque equation can be approximated with:

$$
|\mathscr{T}(\theta)| = A + K\sin(2\theta) + H\sin(\theta). \tag{4.15}
$$

Equation (4.15) is consistent with Stoner-Wohlfarth (SW) [99] model taking in account the contribution from the uniaxial anisotropy and the applied field. With this theoretical insight in reversal process we performed a series of Constrained Monte-Carlo simulations aiming to calculate the torque energy as a function of the polar angle. The approach is to vary the polar angle of the both layers simultaneously from 0° where all spins are aligned to easy axis on $+z$ direction to 180° where the spins are oriented anti-parallel to easy axis. We performed 100,000 CMC steps to average the magnetic properties at each value of the angle with an increment angle step of 5° and keeping fixed the azimuthal angle $\phi = 0°$. Hence, the torque has a maximum on y-component due to in-plane rotation. For simplicity we will consider $|\mathscr{T}| = T_y$ for the further numerical integration prior to find the energy barrier of the system.

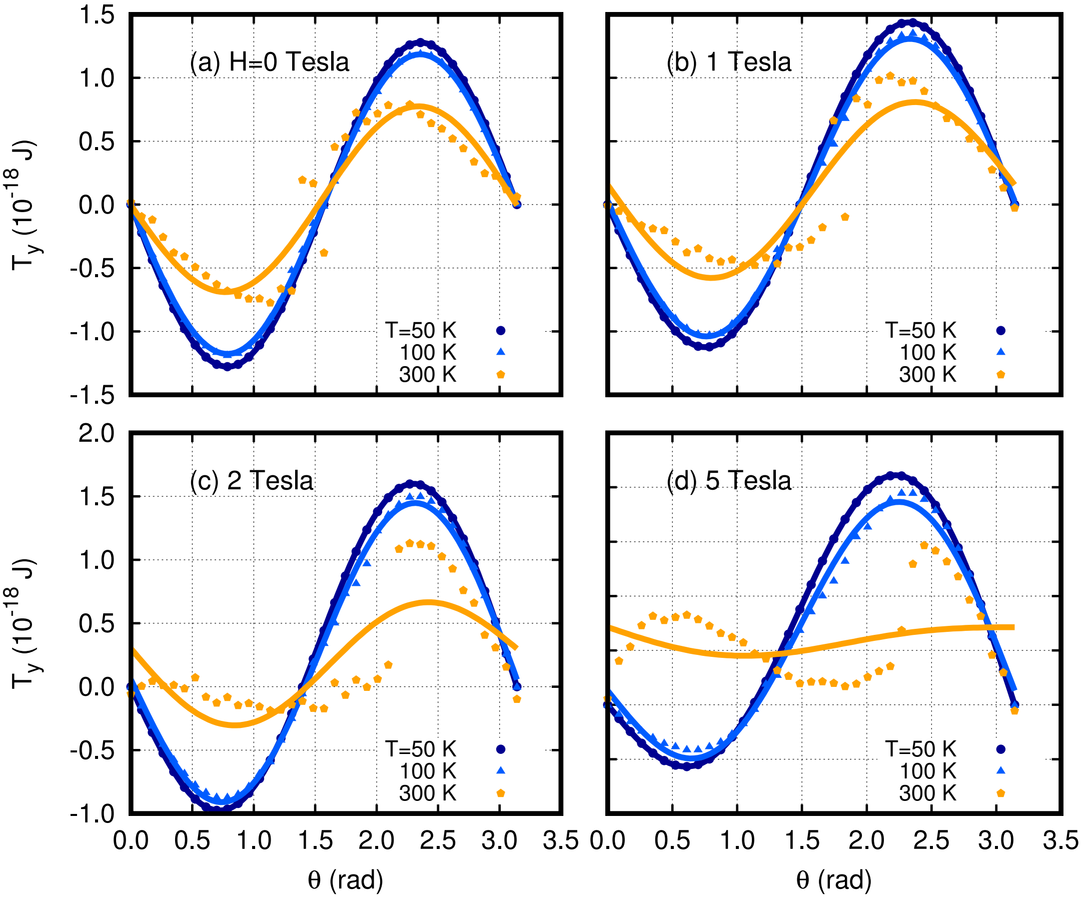

Fig. 4.4 In this graph is plotted the torque energy T_y as a function of the polar angle θ at 50 K, 100 K, and 300 K respectively. The applied field is oriented anti-parallel with easy axis and vary from 0 T to 5 T. The solid lines stand for the fitting using equation (4.15).

In figure 4.4 is plotted the calculated y-component of the torque at each polar angle θ. This shows a perfect agreement with equation (4.15) at lower temperatures independently on the strength of the applied field which denotes a coherent rotation of the spins. Therefore, the composite behaves similarly with SW particle for zero Kelvin while high temperatures break this agreement demonstrated by the solid lines which stand for the fitting following equation (4.15). Figure 4.4 shows an inconsistency of the model for elevated temperatures as the nucleation might occur due to the spin fluctuations. The applied field plays a role in shifting the maximum of the torque for each simulation temperature determining an asymmetric torque curve with an increased magnetic field. This has been demonstrated in figure 4.4 (d) comparing with the case of zero field (a).

As an evidence of different mechanisms of rotation depending on temperature, figure 4.5 shows the layer-resolved magnetisation at any given value of θ. Here, the magnetisation of each atomic layer has been plotted as a function number of atomic layer. Our model of ECC media contains 60 layers where the first 30 are identified as FePt layers and the layers between 30-60 are Fe. Each magnetisation layer is a magnetisation sum of 186 atoms, but there is a discrepancy between saturations of Fe and FePt layers due to different atomic moments for these two types of atoms at zero Kelvin. Here, the saturation value of FePt layer is 351.5 μ_B and 417.3 μ_B for Fe.

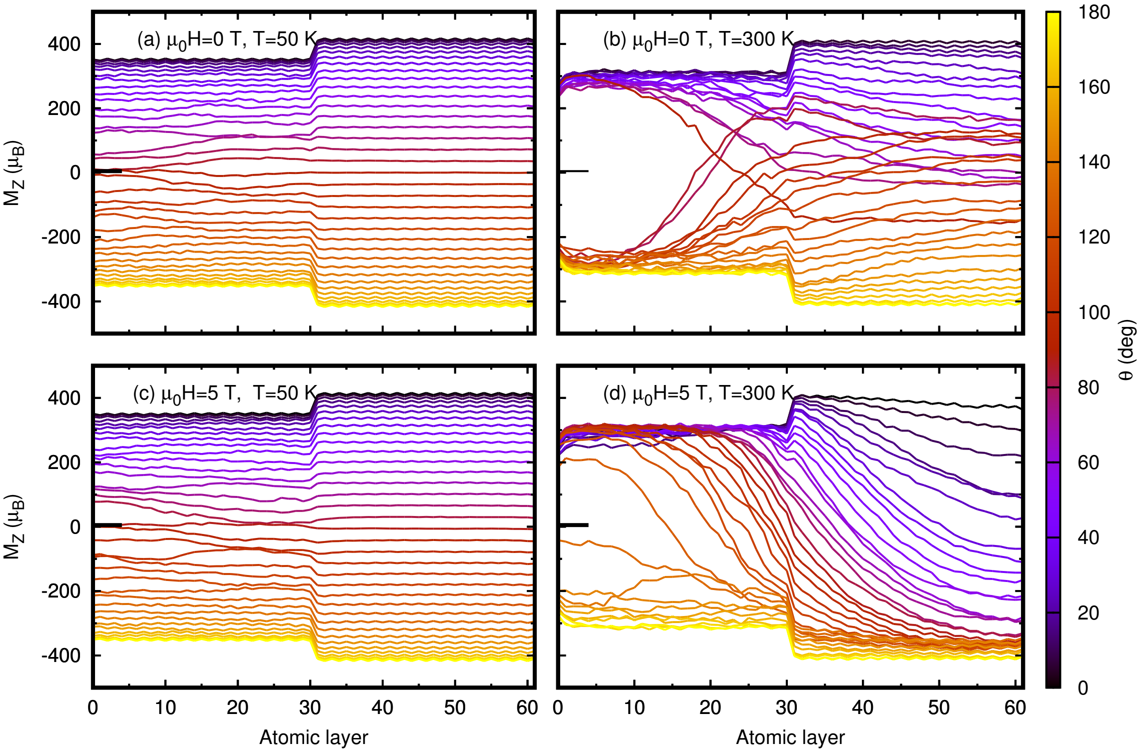

Fig. 4.5 In this graph is plotted the magnetisation of each atomic layer of ECC media during the CMC simulations. The color of line denotes the angle of the magnetisation with respect to the easy axis where light color corresponds to low angles from 0° whilst dark color denotes the high angles up to 180°.

We find that saturation magnetisation for both Fe and FePt layers does not vary with height at low temperatures which denotes the absence of domain wall formation in these cases demonstrated in figure 4.5 (a) and (c). However, with an increased simulation temperature the spin fluctuations will give rise to a variation of saturation with the height. Figure 4.5 (b) and (d) show a nucleation for a temperature of 300 K for two values of reversal field. It can be seen that the presence of nucleation does not depend on the strength of the applied field but the domain wall formation might have different forms depending on the field at elevated temperatures. Analytically, it is expected to observe a domain wall when the size of system is larger than the domain wall width which is calculated as follows[100, 101]:

$$\delta = \pi\sqrt{\frac{A}{K}}, \tag{4.16}$$

where A is the exchange energy known as exchange stiffness and K is the macroscopic exchange. Aharoni[73] found an analytical expression for the exchange computed within nearest-neighbours approximation as:

$$A = \frac{2J_{ij}s^2}{a}c, \tag{4.17}$$

where $a = 3.249\,\text{Å}$ is the lattice parameter, s represents the lattice vector and c is a factor which depends on the crystal structure. For a given value of macroscopic $K_{\mathrm{FePt}} = 1.29\times10^{7}\,\mathrm{J/m^3}$ and $J_{ij} = 4.5\times10^{-21}\,\mathrm{J}$ the domain wall width for FePt is around $\approx 5.25\,\mathrm{nm}$ which is larger than the size of FePt phase (5 nm).

Prior to predicting the thermal stability of ECC media, it is necessary to find the energy barrier of the composite. For a mono-domain particle the energy barrier is predicted by the SW model as:

$$\Delta E_{\mathrm{max}} = KV, \tag{4.18}$$

where K is the macroscopic anisotropy of the particle and V is the volume. The equation (4.18) becomes dependent on the anisotropy field in the presence of an external field. Therefore, different maximum and minimum states of energy appear. Hence, we have different ways to characterize the energy barrier. Assuming a particle whose magnetisation axis changes from $+z$ to $-z$ with perpendicular anisotropy and an external magnetic field applied along the anisotropy direction, the maximum and minimum of energy barrier can be expressed as:

$$\begin{aligned}\Delta E_{\mathrm{max}} &= KV\left(1+\frac{H}{H_K}\right)^2\\ \Delta E_{\mathrm{min}} &= KV\left(1-\frac{H}{H_K}\right)^2\end{aligned} \tag{4.19}$$

where H is the strength of the external field and H_K is the anisotropy field. The energy barrier can be calculated numerically as a difference of maximum and minimum of angular dependence of free energy, ΔF. The free is obtained integrating the torque curve shown in figure 4.4 along the angle using the same approach as in reference [102] where $\Delta F = \int_0^\theta \mathscr{T} d\theta$.

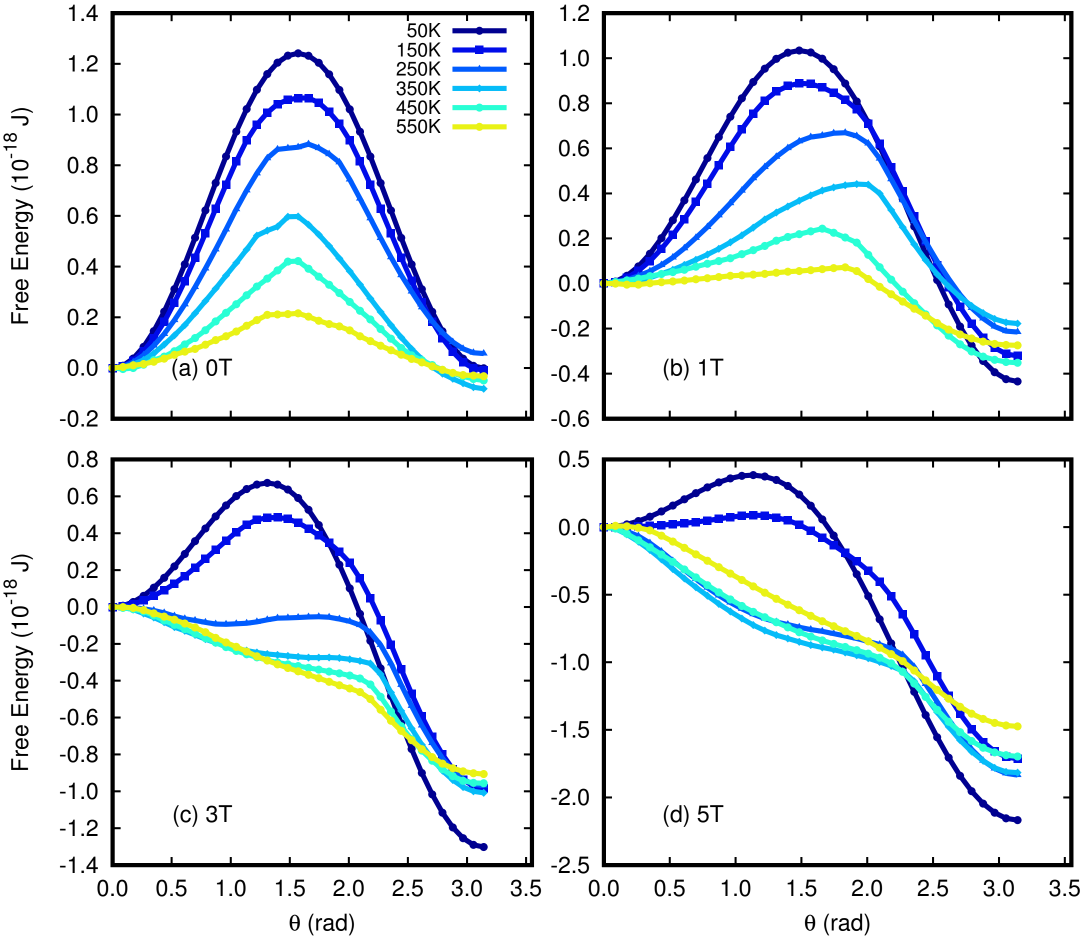

Fig. 4.6 In this graph is plotted the dependence of free energy ΔF as a function of angle at different temperatures by integrating the torque curves shown in figure 4.4 along θ. The reversal magnetic field strength varies from 0 T corresponding to case (a) to 5 T corresponding to graph (d).

Figure 4.6 shows the free energy curves for different simulation temperatures computed numerically using the torque curves presented previously. The strength of the applied field determines the values of the maximum and minimum of the free energy graph, whereas the temperature will decrease the amplitude of the maximum for all the field values. This can be related to random nucleation which might occur in the system corroborated with the applied field. Figure 4.6 clearly shows a reduction of the free energy peak with increasing temperature due to the thermal reduction of the anisotropy while the reversal field makes the minimum lower. Another effect of the magnetic field consists in the shifting of the peak. This is demonstrated more accurately if we compare the blue lines corresponding to the simulation temperature of 50 K where clearly the peak is centred at a smaller polar angle θ for a higher field comparing with the zero field case.

In the following we extracted the maximum of each free energy path in order to determine the energy barrier ΔE which enables determination of the thermal stability of the magnetisation according to Arrhenius-Néel law. Figure 4.7 shows an expected decrease of energy barrier of ECC media with an increased magnetic field according to SW theory. This shows a good agreement between theory and CMC simulations at a simulation temperature of 50 K due to the coherent switching of the spins. However, SW theory is not valid anymore for non-coherent rotation which might occur in some circumstances such as elevated temperature or domain wall formation. In ECC media, nucleation processes can occur also at low temperatures demonstrated by the hysteresis loops in the following section. However, this is happening near to the coercivity zone where the reversal field is closer to the switching field which is time dependent. In our CMC method the magnetic properties are averaged at equilibrium which does not allow any field rate dependence.

All these information related to energy barrier can be useful in calculation of the long-term stability. One option to characterize the thermal stability of a ferromagnet, is to calculate the so called figure of merit shown in the equation below:

$$\xi = \frac{2\Delta E}{MVH_s}, \tag{4.20}$$

where ΔE is the energy barrier, M is the saturation and H_s is the switching field which will be treated in detail in the following section. It is crucial to have a large energy barrier in order to confer thermal stability, however the energy barrier is decreased at high reversal fields and temperatures.

4.3 Coercivity studies

4.3.1 Thermal reduction of the coercivity.

In this section we investigate the coercivity of 10 nm height ECC media with an emphasis on the role of exchange spring on hysteresis loops via a thermal reduction of the coercivity.

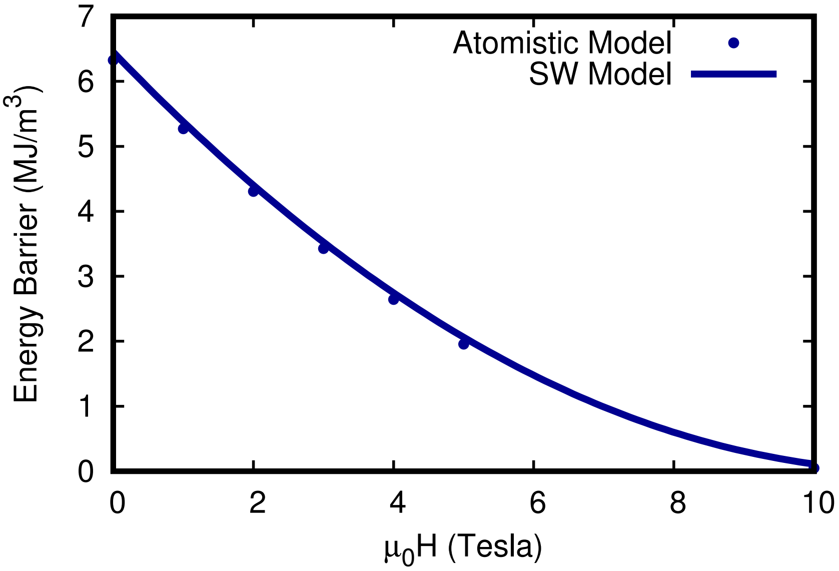

Fig. 4.7 Dependence of the energy barrier on reversal field strength for 10 nm height ECC media. The energy barrier simulation points have been extracted from figure 4.6 as a maximum of each free energy path at a simulation temperature of 50 K. The solid line stands for the fit using SW energy barrier according to equation (4.19).

We first investigate the temperature dependence of the coercivity by simulating a series of hysteresis loops at different temperatures. Here, the sLLG equation has been integrated using the Heun scheme described in the methods chapter. A time of 60 ns using an integration time step of 0.1 fs should be sufficient in order to have an accurate integration and good convergence with regard to a realistic hysteresis loop which depends on the speed of field strength variation in time known as sweeping rate equal to 1 Tns^{-1}. The importance of sweeping rate is given by the Sharrock equation [11, 12] where a slow variation of the field leads to a better equilibration at each magnetic field value which implies a lower coercivity comparing with a high sweeping rate.

$$\frac{H_c(t)}{H_0} = 1 - \left[\frac{k_B T}{\Delta E(0)} \ln\left(\frac{t_0}{\ln(2)\tau_0}\right)\right] \tag{4.21}$$

Equation (4.21) shows a possible decrease of the coercive field with the time t. Therefore, we set our simulations of hysteresis loops to perform 100,0000 integration steps per 0.1 T giving a high accuracy, especially at elevated temperatures where the Heun scheme becomes more sensitive to thermal fluctuations.

The magnetic field has a small deviation from the easy axis and its z-component varies from $+15$ T to -15 T and vice-versa. A typical series of simulated hysteresis loops are shown in figure 4.8 (a). At low simulation temperatures it is clear that switching is a two-step process due to the slow development of the exchange spring. Again, the temperature has been rescaled in the same way as in CMC simulations but the effective field is given by:

$$\mathbf{H}_i = -\frac{1}{\mu_0 \mu_i}\frac{\partial \mathscr{H}}{\partial \mathbf{S}_i} + \Gamma(t)\sqrt{\frac{2\alpha k_B T_{\mathrm{sim}}}{\gamma \mu_s \Delta t}}. \tag{4.22}$$

This equation has been detailed in the methods chapter but again the simulation temperature T_{sim} is calculated via equation (4.10). As the the temperature increases there is a transition from this two-step process to a single step due to the decrease in the FePt anisotropy relative to the interface exchange. For each value of the coupling exchange, the anisotropy of the hard phase (FePt) dictates mainly the value of the coercive field. However, the exchange spring may decrease this value as shown in the following.

In ECC media or hard/soft bi-layer system it is important to understand the nucleation process defined by Aharoni [73] which can effect the switching mechanism. In the exchange spring mechanism a domain wall is nucleated and propagates to the interface where is pinned until the applied field is greater than than the pinning field in order to switch the whole magnetisation of the system. Kronmüller and Goll [103] derived an expression for the pinning field within bi-layer system with different magnetic properties of the both phases. Suess [104] demonstrated a simple formula for the pinning field of a bi-layer system where the exchange and the saturation magnetisations are the same for both layers as follows:

$$H_{\mathrm{pinning}} = \frac{1}{4}\frac{K_{\mathrm{hard}} - K_{\mathrm{soft}}}{J_s} \tag{4.23}$$

Where J_s is the spontaneous polarization. A strong dependence of the pinning field on the difference between the anisotropy values can be observed from equation (4.23) which leads to a decrease at higher temperature due to thermal reduction of the anisotropy demonstrated in the previous energy barrier simulations.

At each temperature the coercive field is extracted, which is shown in figure 4.8(b). This shows a clear decrease with increasing temperature which can be modeled using a power law expression,

$$H_C(T) = H_C(0)\left(1 - \frac{T}{T_C}\right)^{\varepsilon}, \tag{4.24}$$

where ε is a fitting exponent found to be 1.68, $H_C(0)$ represents the coercive value at 0 Kelvin at 6.45T and T_C is the value of Curie temperature determined in figure 4.3 at 700 K for FePt. In particular we note a coercive field of 0.75 Tesla at 500 K which is feasible for switching with the existing inductive head technology. In reference [104] the coercivity dependence on

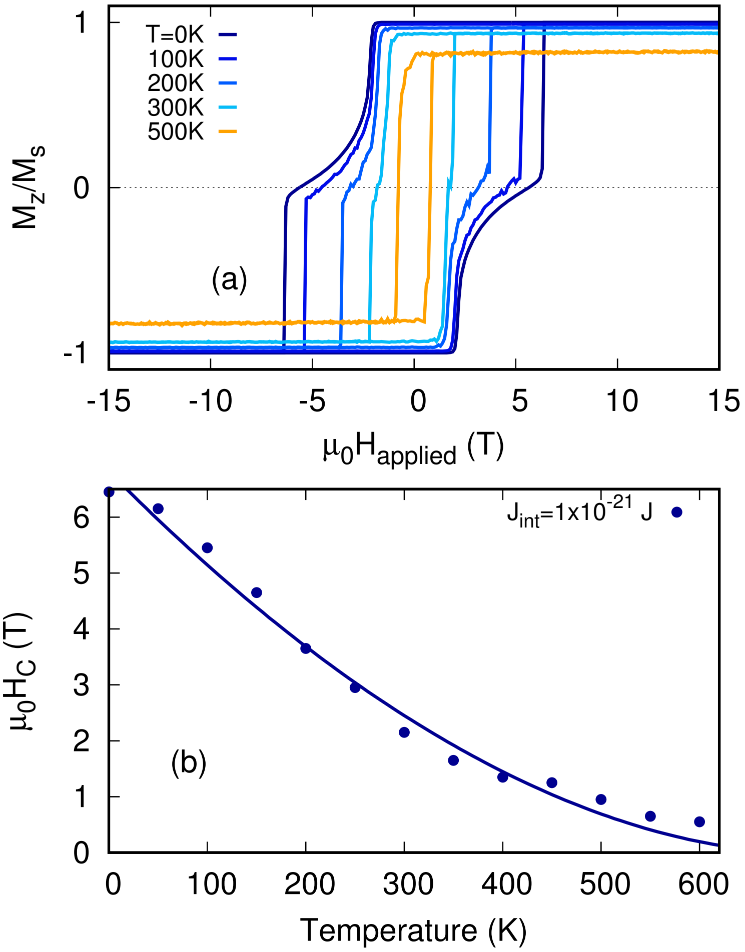

Fig. 4.8 The temperature dependence of coercive field for ECC media. Graph (a) illustrates a series of hysteresis loops for ECC media at different temperatures below the Curie point for a exchange coupling constant at the interface of $J_{\text{int}} = 1 \times 10^{-21}$ J. In graph (b) the points have been extracted from the hysteresis loop at each temperature value shown on graph (a). The solid line is a fit using equation (4.24). $T_C = 700K$ and the fitted values are $H_C(0) = 6.45$T and $\varepsilon = 1.68$

the pinning field is given as:

$$H_C = H_{\text{pinning}} \frac{h}{\delta}, \tag{4.25}$$

where δ is the domain width defined in equation (4.16) and h is the height of the composite. Therefore, a smaller anisotropy caused by various factors can lead to a larger domain width and reduced coercivity.

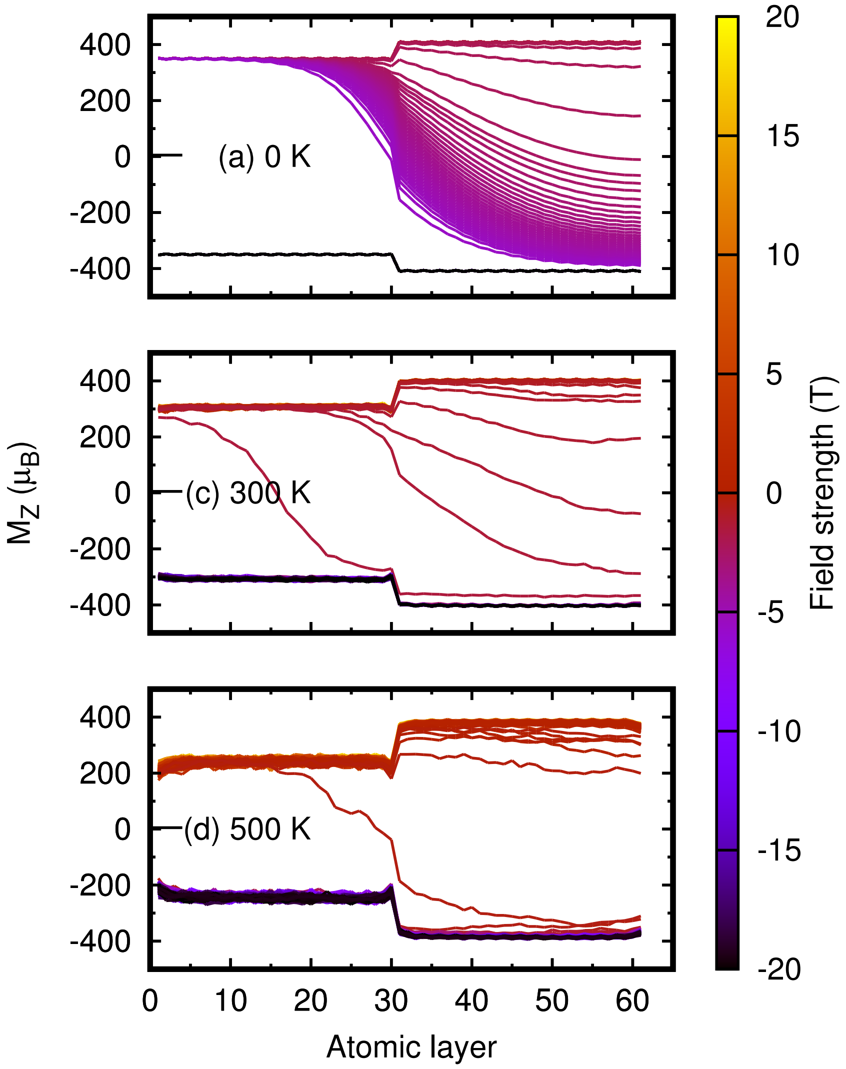

Fig. 4.9 In this graph is plotted the resolved-layer magnetisation for ECC media during the first branch of hysteresis loop when the field varies from 20 T to −20 T. This is suggested by the color where yellow indicates the starting value while dark color indicates negative value of the field. The total height of ECC media grain is 10 nm which contains 60 atomic layers. The first 30 layers correspond to FePt and the layers between 30-60 correspond to Fe.

In order to understand qualitatively how large is the domain wall width, we investigated the profile of the magnetisation. The results are shown in the figure 4.9, which shows the evolution of the layer-resolved magnetisation close to the coercivity for a range of temperatures. It is important to note that at all temperatures the magnetisation proceeds via an exchange spring mechanism. At very low temperatures the domain wall is strongly pinned at the interface due to the high anisotropy as expected from the prediction of Kronmüller and

Goll [103]. At elevated temperatures the weaker pinning leads to faster domain wall motion and reduced switching fields, indicative of a temperature-enhanced exchange spring effect. The exchange spring effect leads to a reduction in coercivity as shown in figure 4.9.

Figure 4.9 shows the evolution of magnetisation for each atomic layer of the exchange coupled composite during the first branch of hysteresis loop where the magnetic field strength varies from 20T to -20T. The magnetisation of each layer has been obtained by summing up all atomic moments contained by each layer as $\sum_i^N \mu_i S_z^i$. At zero field there is a discontinuity of the magnetisation at the interface due to the different saturation magnetisation of each magnetic phase. Both Fe and FePt atomic layers contain $N = 185$ atoms with different individual magnetic moments as mentioned in the section above which leads to a discrepancy between saturation magnetisations of the monolayers. Due to a higher M_S of the soft layer an accentuated spring effect occurs during the switching process. A particular aspect can be seen in figure 4.9 related to the speed of domain wall propagation depending on temperature. A slower switching occurs at zero Kelvin as shown in figure 4.9(a). Secondly, the domain width varies throughout the the hysteresis loops giving larger values close to coercivity zone for all temperatures cases. Hinzke *et al.* [105] demonstrated a larger domain wall width at higher temperatures in good agreement with our simulations. However, in a dynamical process it is hard to determine with a good accuracy the domain wall width due to a fast propagation of the nucleation and noise profile of the magnetisation.

4.3.2 Dependence of the coercivity on thickness and interface coupling. Critical thickness.

Great importance in the design of the recording medium is the thickness of the grains. For ECC media grains extensive studies have been done [106–110] to find the optimal balance between quantities of the soft and hard phase with respect to the density requirements. In reference [108] the FePt/Fe bi-layer is experimentally investigated using a SQUID magnetometer for measuring the magnetic properties at room temperature. A remarkable drop of the coercivity has been found with increasing the thickness of Fe layer at room temperature, particularly at thicknesses less than FePt thickness. For a thickness of Fe greater the FePt, the nucleation starts to play an important role in the reversal mechanism. The simple expression of Thiele *et al.* [90] given in equation (4.4) predicts a decrease of the coercity to zero with increasing thickness. However, the numerical results indicate a decrease to a minimum value. This is consistent with Goll and Breitling who pointed out that the coercivity cannot be smaller than the nucleation field [103].

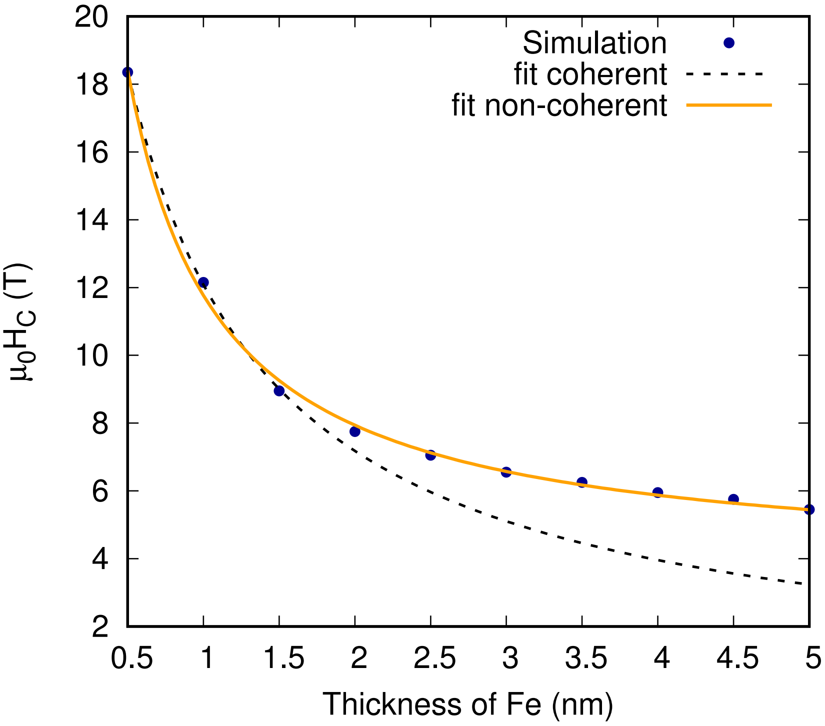

Fig. 4.10 The dependence of the coercive field on thickness of Fe. The thickness of FePt is kept fixed at 5 nm while the thickness of Fe varies from 0.5nm to 5nm. The solid points represent the value of coercive field extracted from hysteresis loop for each value of Fe thickness. The dashed line represent the fit using equation (4.5) whereas the solid line is the fit using the equation (4.26) [106]. The fitting gives a value for the nucleation field of 3.75 T.

Atomistically this dependence has been investigated by simulating a series of hysteresis loops in the same manner presented early in this chapter by extracting the coercive field from each hysteresis. The thickness of the soft layer has been varied from 0 nm to 5 nm whereas the FePt thickness is kept fixed at 5 nm. The results are shown in figure 4.10 for ECC media with a constant at the interface $J_{\text{int}} = 3 \times 10^{-21}$ J. Here, is observed a decrease of the coercive field where we can distinguish two regimes of switching: coherent and non-coherent. The coherent rotation can be fitted well by Thiele dependence (shown in equation 4.4) up to a specific thickness of the soft layer. In this case we restricted the fit up to 3 nm where this equation provide an excellent agreement. For higher values of the thickness the coherent equation breaks due to nucleation. A reasonable equation which describe this dependence has been found experimentally in reference [106] where the coercivity as a function on thickness is given by:

$$\mu_0 H_C(t_{\mathrm{Fe}}) = \frac{c_1}{t_{\mathrm{Fe}} + \dfrac{c_2}{\mu_0(H_C(0) - H_{\mathrm{n}})}} + \mu_0 H_{\mathrm{n}}, \tag{4.26}$$

where $c_{1,2}$ are some arbitrary fitting parameters. After the fitting a nucleation field $\mu_0 H_{\mathrm{n}} = 3.75\,\mathrm{T}$ has been extracted. According to this, for infinite thickness the coercivity achieves a ninimum value of:

$$\lim_{t_{\mathrm{Fe}} \to \infty} \mu_0 H_C(t_{\mathrm{Fe}}) = \lim_{t_{\mathrm{Fe}} \to \infty} \left[\frac{c_1}{t_{\mathrm{Fe}} + \dfrac{c_2}{\mu_0(H_C(0) - H_{\mathrm{n}})}} + \mu_0 H_{\mathrm{n}} \right] = \mu_0 H_n \tag{4.27}$$

Further investigations have been done by Y. Liu *et al.* [108] on FePt/Fe bilayer films where they measured the coercivity as a function of Fe thickness. They found a variation of nucleation field with Fe thickness both experimentally and theoretically.

Another important factor in order to decrease the switching field is the exchange coupling at the interface. For simplicity in this model we assume a direct exchange coupling between Fe and hybrid FePt atoms. In reality this exchange coupling can vary in a wide range depending on the qualities of the interface such as roughness, contact surface, crystal defects, etc. Therefore, several series of hysteresis loops have been performed for 10 nm height ECC media varying the exchange coupling at the interface.

Figure 4.11 shows the temperature dependence of coercivity for three different exchange coupling values at the interface. There is a slight decrease of the coercivity with an increased exchange coupling at the interface demonstrated by zero kelvin points in the graph. The dependences have been fitted using equation (4.24) giving an increase of power exponent ε from 1.68 for $J_{\mathrm{int}} = 1 \times 10^{-21}\,\mathrm{J}$ to 2.69 for $J_{\mathrm{int}} = 5 \times 10^{-21}\,\mathrm{J}$ denoting a lower coercivity for a stronger coupling at the interface.

4.4 Investigation of dynamical switching

In this section of the chapter, we investigate the switching mechanism process with emphasis on the role of the damping constant over the reversal mechanism. It is demonstrated that various damping constants can make the process faster or slower depending on several magnetic factors such as exchange spring enhanced by temperature. In Atomistic Spin Dynamics (ASD) model, damping constant is take as Gilbert form [48] where the lost energy

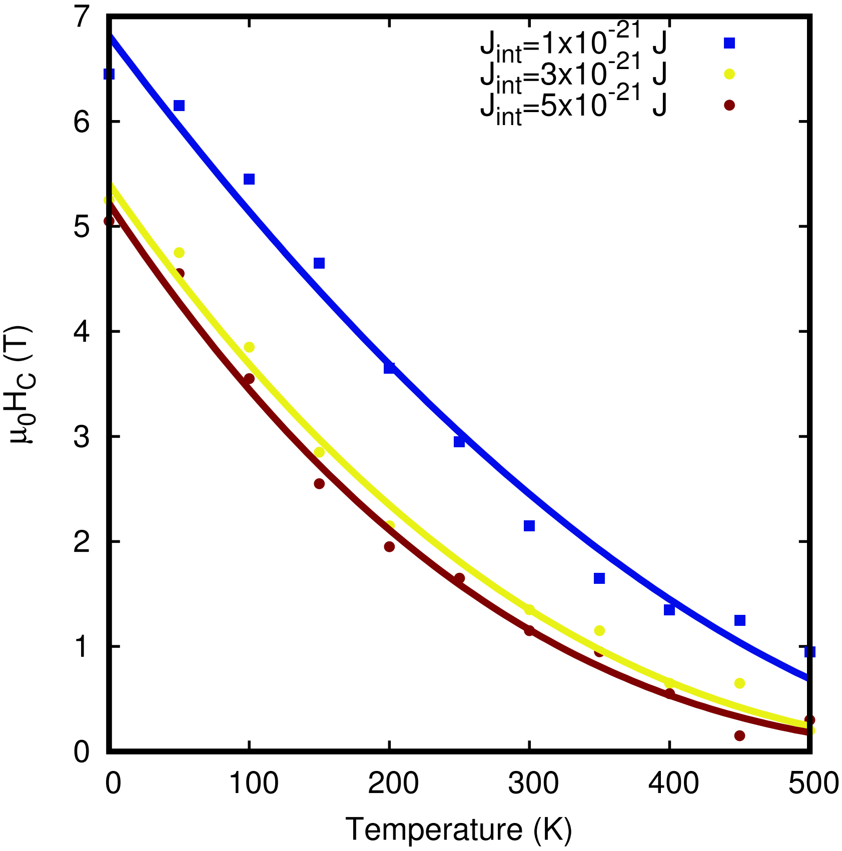

Fig. 4.11 In this graph is plotted the temperature dependence of the coercivity for three different exchange coupling at the interface. The simulated points have been extracted from the hysteresis loops whereas the solid lines stand for the fit using equation (4.24).

of a ferromagnet within a magnetisation process is attributed to a damped magnetic field which is proportional to the effective field.

4.4.1 Single particle switching and the Kikuchi law.

A single domain particle is the basic model which assumes all spins are parallel being described by the classical **LLG** equation. By solving the dynamical equation of a single domain particle it provides the fundamental insight in recording media. Here, Kikuchi [111] derived the minimum time needed for a ferromagnetic particle to switch its magnetisation for a given magnetic field. Here for a spherical particle which changes its magnetisation from M_{zi} state to M_{zf} state, the time is given by following equation:

$$\tau_f = \frac{1}{2\gamma H_{\text{eff}}} \frac{1+\alpha^2}{\alpha} \ln \frac{\left(M_s + M_{zf}\right)\left(M_s - M_{zi}\right)}{\left(M_s - M_{zf}\right)\left(M_s + M_{zi}\right)}, \tag{4.28}$$

where H_{eff} is the effective field, α is the damping constant and M_s is the saturation magnetisation. For the particular case of switching from oriented along easy axis state to in-plane, the reversal time can be expressed as:

$$\tau_f = \frac{1}{2\gamma H_{\mathrm{eff}}} \frac{1+\alpha^2}{\alpha}. \tag{4.29}$$

For most magnetic materials the damping constant $\alpha \ll 1$ where equation (4.29) shows a clear decrease of reversal time τ_f on damping constant. In the following, we simulate a generic Fe particle whose domain wall width is much larger than particle sizes keeping the same atomistic parameters for Fe as in previous simulations. It is assumed that an isolated Fe particle with a diameter of 5 nm acts like a single domain particle. We have investigated the reversal time defined by Barker *et al.* [112] as the time elapsed from aligned magnetisation on easy axis $m_z = 1$ to plane $m_z = 0$ where equation (4.29) is expected to give reasonable prediction of the switching time for a single domain particle. Figure 4.12 shows a series of reversal mechanism processes for Fe by integrating the **sLLG** equation for 10 ns under an applied field of 0.5 T. The trigger process of the reversal mechanism can be achieved with a minimal torque of the spins, generated by a small thermal fluctuation using a simulation temperature of 5 K. A logarithmic decrease of the reversal time with damping constant λ has been found as demonstrated in figure 4.12 (b), where we fit the calculated data with the Kikuchi equation (4.29) showing a good agreement.

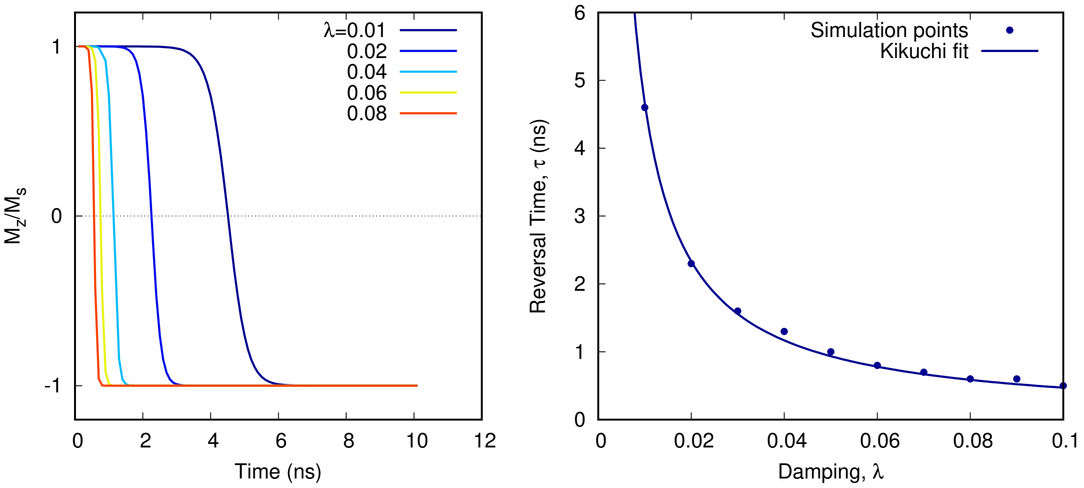

Fig. 4.12 Reversal time dependence on damping constant for a particle of Fe with 5 nm diameter. The left graph shows the time evolution of z-component of the reduced magnetisation for different values of the damping. The right graph shows the dependence of the reversal time extracted from simulation curves form the left graph.

These simulations show a great importance of the damping on the speed of the switching. Particularly, it is noted a reversal time of $\tau = 5 \times 10^{-10}\,\text{s}$ for $\lambda = 0.1$ being one order less than the case of $\lambda = 0.01$ where $\tau = 4.6 \times 10^{-9}\,\text{s}$.

The Kikuchi law can be applied successfully for monodomain particles, however for different designs of recording medium where nucleation can occur, the reversal time might not be consistent with minimum reversal time calculated by Kikuchi. One example is ECC media design where different polarizations and magnetic properties might generate side effects during the switching process. This has been investigated in detail in the following section in order to find a quantitative dependence of the reversal time on the damping for complex structures.

4.4.2 Switching mechanism of ECC media.

An optimal strategy to heat ECC medium is an issue which requires attention. This can be made by using a laser whose spot can have a spatial and temporal distribution, Gaussian distribution for example. Two strategies are proposed in reference [113] in order to increase the capabilities of HAMR. The first method implies a continuous laser spot applied on the material whereas the second method uses a pulsed laser spot.

In order to construct a realistic model of HAMR process for reversing the magnetisation via heating and reversal field we consider following profile of temperature:

$$T(t) = (T_{max} - T_{min}) \exp\left[-\left(\frac{t - t_p}{t_c} \right)^2 \right] + T_{min}, \tag{4.30}$$

where t_c is the cooling time and t_p is the time where the temperature reaches its maximum T_{max}. The total time of each simulation is 5 ns with the temperature peak at $t_p = 3\,\text{ns}$ and a cooling time of $t_c = 1\,\text{ns}$. The minimum and maximum temperatures used are 300 K , and 500 K respectively. For simplicity, the spatial variation of temperature is ignored as we assume all spins are exposed to the same temperature. This is based on the time of exposure to the elevated temperatures around nano-seconds being enough to achieve a thermodynamic equilibrium.

Beside the temperature another important factor in this process is the strength of the magnetic field. Due to an engineering limitation of the intensity of electrical current which passes into the coil, the maximum applied field produced cannot be much larger than 1 Tesla. Hence, in our HAMR model we will consider a reversal field of one Tesla.

4.4.3 The impact of Gilbert damping on the reversal time. Conventional and high field regime.

We now proceed to investigate the effect of damping constant of the soft layer by simulating the reversal mechanism in the same approach presented in the previous subsection. Here, a typical switching process is simulated over 5 ns with an integration step of 0.1 fs providing an accurate integration especially at elevated temperatures where the integration scheme is more sensitive to the thermal fluctuations.

Becker *et al.* [114] measured experimentally the damping of FePt using ferromagnetic resonance (FMR) for a wide range of temperatures and magnetic fields. They found a high damping value for $\mathrm{L1_0}$ FePt phase around 0.1. For this reason the FePt damping has been kept fixed in these simulation to 0.1 allowing variation of Fe damping only. In reference [115] has been demonstrated both experimentally and theoretically that a generic soft ferromagnet such as $\mathrm{Ni_{80}Fe_{20}}$ can reach high value of damping constant by doping with rare earth elements (RE) such as: Dy, Tb, Gd, and Ho. Furthermore, a linear increase of damping constant with the concentration of RE has been noted in experiment where RE doping increase the relaxation time measured with FMR. A remarkable increase of damping can be done using Dy doping approaching a value of $\alpha \approx 0.2$. We, therefore, will consider a high damping regime for Fe which presumably will speed-up the switching.

We previously found that for a temperature of 500 K and higher, the coercivity zone can be achieved with a strength of field around 1 T. Here we investigate the reversal mechanism for a range of fields finding an anomalous behaviour of the switching time with damping constant at fields around the coercivity.

Figure 4.13 (a-c) shows the time evolution of the z-component of reduced magnetisation for different damping constant of the soft layer (Fe) and different exchange coupling constants at the interface (a) $J_{\mathrm{int}} = 5 \times 10^{-21}\,\mathrm{J}$, (b) $J_{\mathrm{int}} = 3 \times 10^{-21}\,\mathrm{J}$, and (c) $J_{\mathrm{int}} = 2 \times 10^{-21}\,\mathrm{J}$ in a reversal field of 1 T. It is clear faster switching is happening with decreasing damping constant which is inconsistent with the Kikuchi law. This dependence can be interpreted as an effect of the exchange spring confirmed in the figure 4.9 where the switching proceeds via nucleation produced within Fe layer being pinned at the Fe/FePt interface before propagating into the FePt phase. The switching speed is determined by the strength of the pinning field enhanced by the interfacial exchange and anisotropy value. Prior to switching, a time is needed in order to obtain the spring configuration which leads to a faster switching for smaller damping coupled with a stronger exchange coupling.

Figure 4.13 (d-f) shows the evolution of transverse component of reduced magnetisation for Fe layer during the reversal mechanism calculated as $S^{\mathrm{Fe}}_{\mathrm{transverse}} = \frac{1}{N}\sum_i^N \sqrt{(S^{Fe}_{ix})^2 + (S^{Fe}_{iy})^2}$,

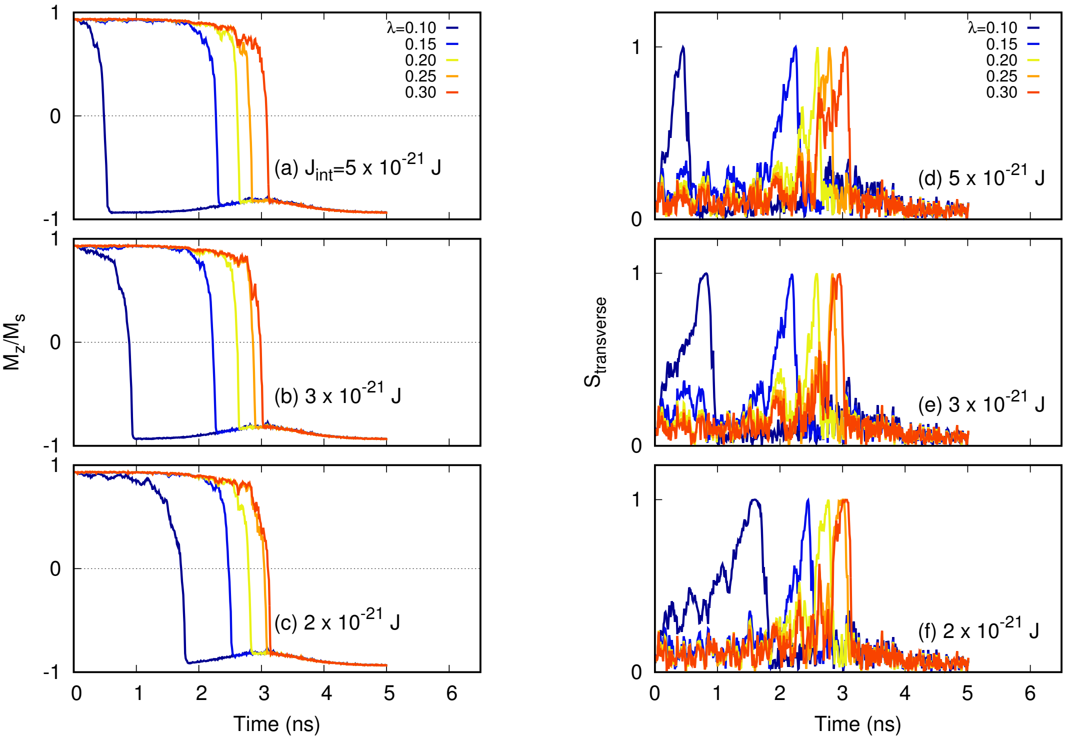

Fig. 4.13 In this graph is plotted the reversal mechanism of 10 nm height ECC media for different damping constant of the soft phase (Fe) at different exchange coupling values at the interface: (a) $J_{\text{int}} = 5 \times 10^{-21}$ J, (b) $J_{\text{int}} = 3 \times 10^{-21}$ J, and (c) $J_{\text{int}} = 2 \times 10^{-21}$ J. Figures (d-f) shows the time evolution of transverse component of Fe layer during the reversal mechanism calculated as: $S^{\text{Fe}}_{\text{transverse}} = \frac{1}{N}\sum_i^N \sqrt{(S_{ix}^{Fe})^2 + (S_{iy}^{Fe})^2}$. For all these simulations the damping of the hard phase (FePt) has been set at $\lambda = 0.1$ with an reversal field of 1 T and the temperature pulse follows the equation (4.30) where the maximum and minimum temperatures are 500 K, respectively $300K$.

where $N = 185$ is the total number of atoms contained by a single atomic layer of Fe. The evolution of Fe magnetisation it is important in understanding the switching mechanism as the magnetisation of Fe needs to be oriented in-plane before magnetisation propagates into the FePt phase. The exchange spring effect is maximum when the Fe magnetisation aligns in-plane requiring a certain number of precession cycles depending on the damping. Figures 4.13 (d-f) show the time needed for approaching a plane orientation of the Fe magnetisation. Here, a higher values of damping constant leads to more precession cycles in order to trigger the propagation of the magnetisation into FePt.

Figure 4.14 illustrates four cases of reversal mechanism in detail by averaging the z-component of reduced magnetisation per atomic layer denoted by the color, where red color represents "up" alignment and blue color is "down". For all cases the switching occurs before

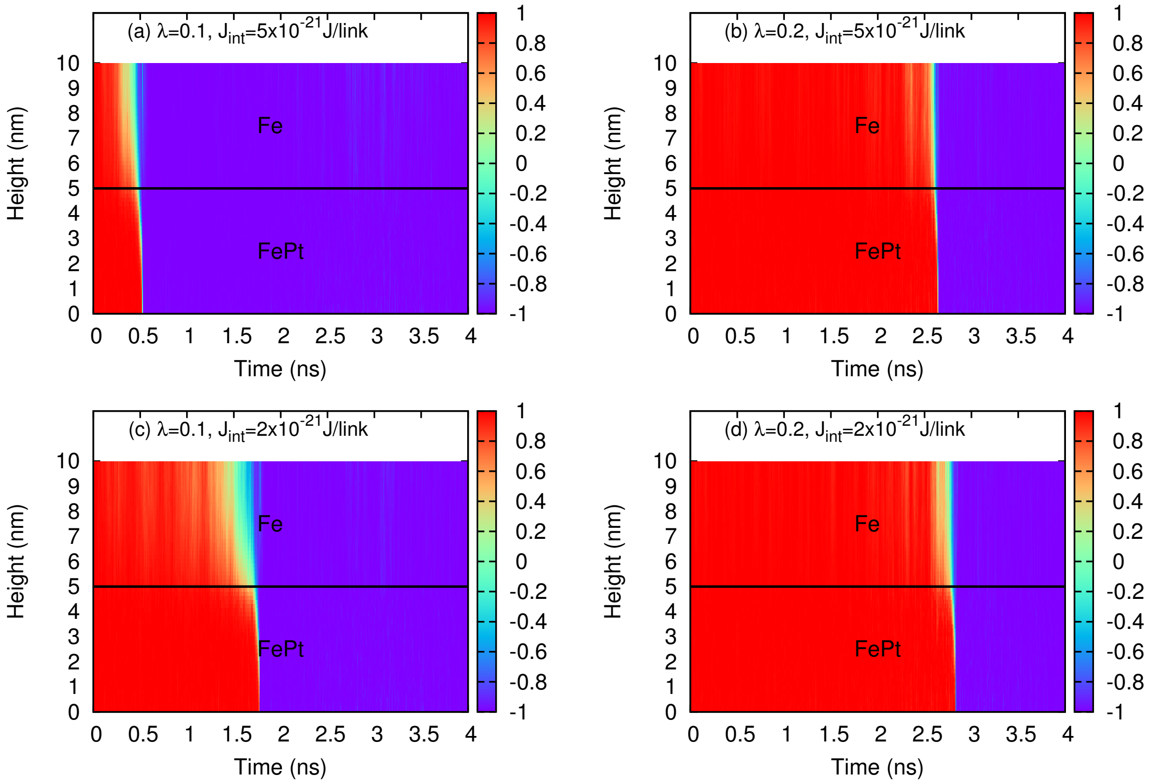

Fig. 4.14 In this graph is plotted the magnetisation profile during reversal mechanism for two different exchange coupling and two different Gilbert damping values. The system contains 60 atomic layers, the first 30 layers $\approx 5\,\mathrm{nm}$ correspond to FePt and the top layers correspond to Fe. The colors indicate the value of z-component of magnetisation. Here red color indicates a positive value of reduced magnetisation on z direction, blue indicates a negative, respectively white suggests a plane orientation of the reduced magnetisation.

the temperature reaches its maximum ($T_{\mathrm{max}} = 500\,\mathrm{K}$) at 3 ns. We explored two different exchange coupling strengths at the interface, and two different cases of damping. A clear increase of switching time can be seen again for a higher damping constant whereas a decrease of switching time occurs for an increased J_{int}. Another interesting observation from these color maps is related to different modes of switching in Fe compared with FePt. Here, white color shows a plane orientation giving more precession cycles of the magnetisation. Therefore, we can identify two modes of switching: one which involves more precession cycles called precessional switching characteristic to Fe layer where more white lines can be seen in comparison with FePt where less white lines can be seen.

In order to plot the dependence of reversal time τ on damping, we have extracted the reversal time from each $M_Z/M_S(t)$ loops shown in figure 4.13. Here, figure 4.15 (a) shows the dependence $\tau(\lambda_{\mathrm{Fe}})$ for two different exchange coupling. A clear increase of reversal time

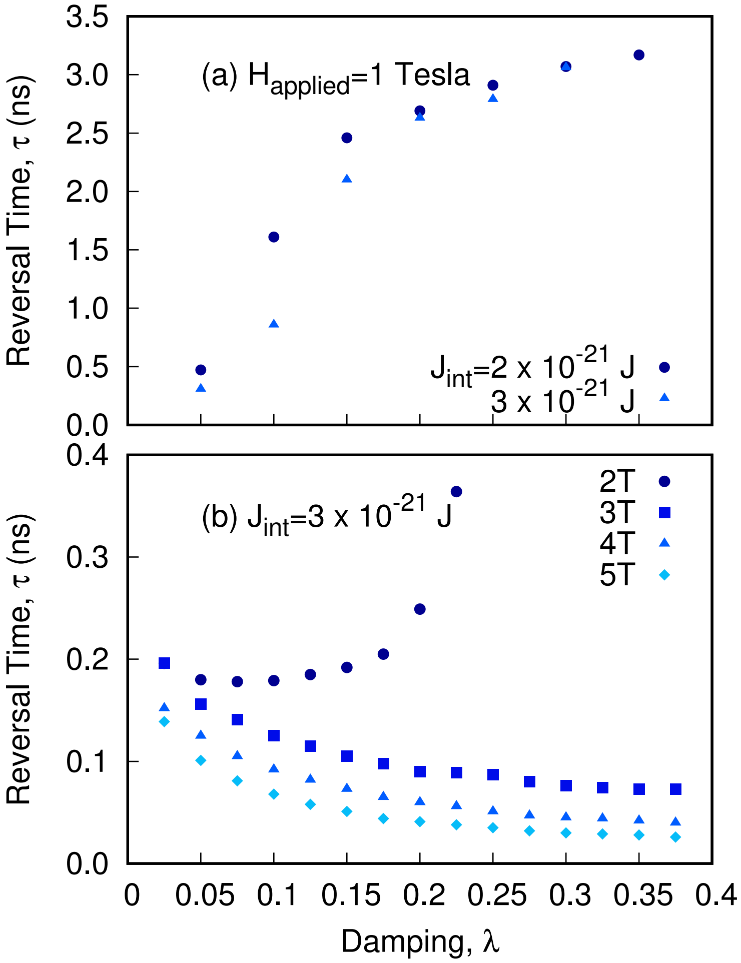

Fig. 4.15 In this graph is plotted the dependence of reversal time as a function of damping parameter for different cases: (a) low field near to the coercivity, $\mu_0 H_{\text{applied}} = 1\,\text{T}$, and (b) higher fields.

can be seen which is inconsistent with the Kikuchi law. A more pronounced increase of averaged reversal time can be seen for stronger exchange coupling as an effect of a weaker switching field. This has been demonstrated by Vogler *et al.* [116] using LLB macro-spin simulations.

On the other side, higher fields will lead to a faster propagation of nucleation here the speed of switching is not sensitive to the damping. Figure 4.15 (b) shows a change of reversal time dependence on damping where higher fields will lead to a decrease of the reversal time with damping.

Finally, we turn our investigation to the dependence of the reversal time on Fe thickness. It is hard to explore a regime of lower thickness of Fe within conventional fields due to an increased coercivity of the system which requires higher reversal magnetic field to obtain the switching. In the following we performed a series of investigations under a reversal field of 3 T by varying the thickness of the soft phase from 1nm to 5nm. Here, figure 4.16 shows the dependence of the reversal time on Fe thickness at different values of the damping for Fe. The simulations are performed in the same manner with the previous calculations presented early by using a temperature profile according to equation (4.30) where the maximum/minimum temperature is 500K, and 300K respectively.

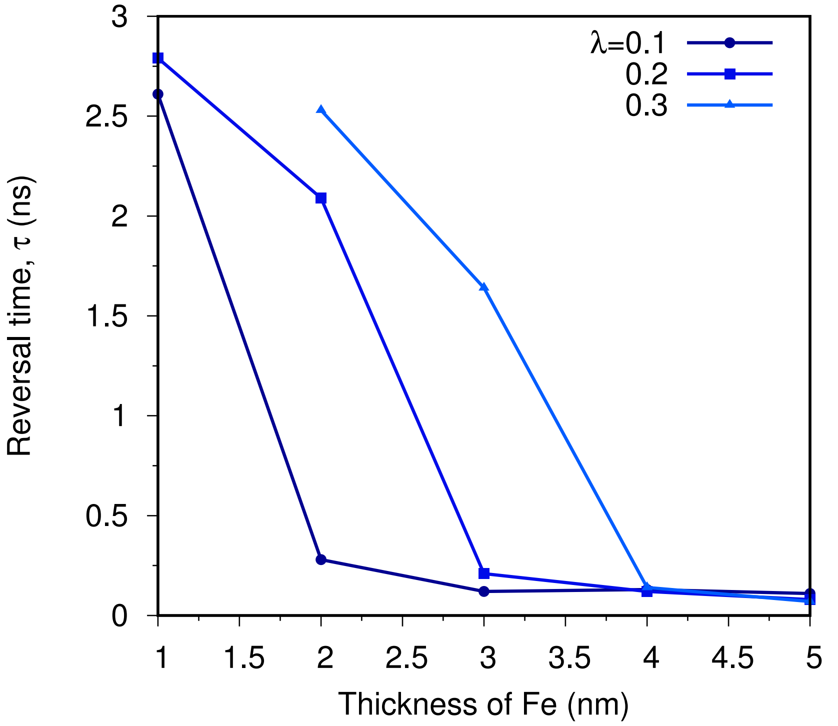

Fig. 4.16 In this graph is plotted the dependence of reversal time as a function of Fe thickness at different values of Fe damping. The strength of the reversal magnetic field is 3 T. The solid lines represents the eye guidance.

The writing field is increasing with increasing thickness of the soft phase demonstrated early in this chapter. We showed a strong agreement of our atomistic simulation on coercivity which varies on the thickness with respect to the Thiele law *et al.* [90] shown in equation (4.5). For a given reversal field strength, the thickness of the soft phase will influence the reversal time as a consequence of different writing fields at different number of Fe layers added into the system. Here, a larger thickness of the soft phase will lead to a shorter reversal time in the high field regime. In addition to this, for a thickness of 1nm and a damping value of 0.3, the switching cannot occur due to a larger writing field than 3T.

Greaves *et al.* [117] showed that for an increased thickness of the soft phase the nucleation field decreases. This is important in microwave-assisted magnetic recording (MAMR) where the switching is performed using a micro-wave generator embedded in the writing head [21]. This will transfer energy to the soft layer determining high precession of the magnetisation which lead to precessional switching with an applied field less the the coercivity of the material. In reference [117] it is shown that a good performance of this method is obtained when they apply a linear pulse with a specific frequency. It is also demonstrated that with an increased thickness of the soft layer there is an optimal frequency which determines the lowest switching field [117]. An increased frequency is required for low thickness of the soft phase which is in agreement with our results where longer reversal time is need for a low thickness of Fe phase as shown in figure 4.16 for a the value of damping $\lambda_{\mathrm{Fe}} = 0.1$ for example.

4.5 Conclusions

In this chapter we investigated the reversal mechanism of ECC media by employing the Atomistic Spin Model using two different approaches: static properties using CMC simulations and dinamycal properties using sLLG equation. We dedicated a particular interest in the benefits of ECC design which is supposed to perform well in HAMR due to the exchange spring effect. Our simulations show a good qualitative temperature dependence of the coercivity compared with the experimental results revealing a decrease of the writing field at elevated temperatures due to the reduction of the energy barrier on high thermal fluctuations.

CMC simulations show a reduction of the energy barrier with an increased temperature being feasible for HAMR temperature regime. However, CMC method does not predict a realistic decrease of the energy barrier with an increased applied field at low-temperature regime due to a coherent switching of the ECC media. In reality, we expect the nucleation to occur during the reversal mechanism according to dynamical simulations where the nucleation field can reduce the energy barrier as well. It has been found that nucleation appears at elevated temperatures, where the spins are allowed to randomly fluctuate in a wider angular range of the magnetisation favouring the non-coherent rotation of the system. An improvement of the field dependence might be obtained if we consider a different method to simulate the energy barrier where the constrained is done by a Lagrange multiplier field allowing the the integration of LLG equation. The implementation of this method remains further work.

Dynamic simulations give us more insight into the exchange spring behaviour of ECC media. We found the nucleation of the domain wall during the hysteresis loops which effects the switching mechanism. Further observations have been done by studying the reversal mechanism. We observed an anomalous damping dependence in heating/cooling processes in fields around the coercivity. Here a lower damping of the soft phase is found to accelerate the switching at low-regime of the fields, whereas higher fields will give an expected dependence of the reversal time on damping denoting a minimal effects of the nucleation caused by a faster propagation of the domain wall. We conclude that nucleation in ECC media needs to be considered, and is determined by several factors including the strength of the applied field, temperature, exchange coupling at the interface and thickness of the soft layer. Here the damping constant plays a crucial role in determining the speed of domain wall propagation, explaining the unexpected results at conventional fields.

Chapter 5

RKKY model of exchange interaction in FePt

In this chapter a new approximation to exchange interactions for FePt is proposed in order to describe the magnetic properties under different internal or external factors with a great importance for heat assisted magnetic recording since $L1_0$ FePt exhibits great properties for recording media. This model is represented by RKKY function which gives a new perspective into magnetic interaction in the relatation to the magnetisation processes in finite FePt grains. The aim is to produce an approximate spin Hamiltonian with a reduced number of neighbours in order to speed up the simulations of HAMR process in FePt media. In addition, a particular interest has been dedicated to investigate how the number of interactions per bond can influence the evolution of the magnetization at different temperatures and sizes of the system. We found this model more optimal to use in Monte-Carlo simulations in terms of the computational effort than full DFT-based spin Hamiltonian of Mryasov *et al.* [41].

Another aim of this chapter is to present a fundamental study of the implications of different lattice properties on finite size effects and how different truncations of the neighbours list can influence the temperature magnetization dependence at different sizes of the grains for a better understanding towards improving signal-noise-ratio (SNR).

5.1 Exchange interaction models of FePt.

5.1.1 First principle calculations of exchange interactions in FePt

$L1_0$ FePt exhibits good properties for recording media, particularly for heat assisted magnetic recording (HAMR) due to high magneto-crystalline anisotropy about $K \approx 7 \times 10^7\,\mathrm{erg/m^3}$ [32]. Therefore, a great effort has been dedicated to understand the exchange interaction especially at lower dimensions of the particles where the FePt grains can loose their ferromagnetic properties.

One reasonable approach is the first principle exchange interactions presented in reference [94] where the exchange coupling constant follows an oscillatory dependence with the separation distance between atoms as shown in figure below 5.2. The values for the exchange interactions have been determined by using first principle calculations for each atomic bond up to a radius of six unit cell sizes. In other words, in this model each atomic exchange energy is calculated using the interaction of the neighbors within a radius up to 2 nm.

$L1_0$ FePt phase allows Fe to polarise the Pt moments, bringing in to play the spin-orbit coupling of the Pt atoms. The configuration of $L1_0$ can be seen in figure 5.1 (a) where a single unit cell contains 4 atoms. The red atoms represents Pt atoms centered on the faces and blue spheres shows the distribution of Fe atoms.

(a) $L1_0$ phase

(b) Mryasov phase

Fig. 5.1 Models of crystal structure of FePt. Image (a) shows a face-centered cubic (FCC) structure which corresponds to $L1_0$ phase and image with two sorts of atoms: blue color illustrates the Fe atoms and red color illustrates the Pt atoms. Image (b) shows a simplified model used by Mryasov *et al.* where Pt atoms are not modeled leading to a BCC structure. The unit cell size for $L1_0$ is 3.54 Å, whereas for BCC is 2.50 Å.

For simplicity in the Mryasov spin Hamiltonian determined by the *ab-initio* data, the Pt atoms are not modeled but the effects of Pt are taken in account using an average moment induced by the Fe and exchange. Therefore, from $L1_0$ phase which consists in FCC structure as shown in figure 5.1 (a) the lattice is replaced with a single sort of atoms arranged in a structure shown in figure 5.1 (b). Within this model the vibrations of the lattice are not considered which implies a constant separation between atoms. The lattice parameter is $a = 2.50$ Å.

It is found that the Pt moment within this alloy is directly proportional to the exchange field from the Fe, which allows for a substitution removing the Pt and leaving the Fe as the only degrees of freedom. In reality, the Pt atoms are polarised by Fe giving rise to a local magnetic of moment of Pt which is calculated as:

$$\mathbf{m}_{\mathrm{Pt}} = \frac{1}{H_\nu} \sum_i J_{i\nu} \mathbf{S}_i, \tag{5.1}$$

where $J_{i\nu}$ is the effective exchange parameter between Fe and Pt, $\mathbf{S}_i$ is the Fe spin moment. H_ν is exchange field induced by the Fe neighbours into Pt sites. Constrained local-spin-density-approximation (CLSDA) [118] calculations shows a small in-plane anisotropy of Fe whereas the uniaxial anisotropy is given by the Pt moments which can be calculated as:

$$\mathscr{H}_{\mathrm{ani}} = -\sum_i \left[k^0_{\mathrm{Fe}} + k^0_{\mathrm{Pt}} \left(\frac{1}{H_\nu} \right)^2 \sum_\nu J^2_{i\nu} \right] (\mathbf{S}^z_i)^2 \tag{5.2}$$

Here both anisotropy contribution can be combined in a single generic constant $k^0_i = k^0_{\mathrm{Fe}} + k^0_{\mathrm{Pt}}/N \left(\frac{1}{H_\nu} \right)^2 \sum_\nu J^2_{i\nu}$ denoting the single-ion anisotropy constant for each individual hybrid-atom surrounded by N neighbours.

Finally, the full corresponding Hamiltonian for Mryasov model is expressed in the equation below:

$$\mathscr{H} = \underbrace{-\frac{1}{2} \sum_{i \neq j} J_{ij} \mathbf{S}_i \cdot \mathbf{S}_j}_{\mathscr{H}_{\mathrm{exc}}} \underbrace{- \sum_i k^0_i \, (S^z_i)^2}_{\mathscr{H}_{\mathrm{ani}}} \underbrace{- \frac{1}{2} \sum_{i \neq j} d^2_{ij} S^z_i S^z_j}_{\mathscr{H}_{\text{2-ion}}} \tag{5.3}$$

Another term of the exchange $\mathscr{H}_{\text{2-ion}} = \sum_{i \neq j} d^2_{ij} \mathbf{S}^z_i \cdot \mathbf{S}^z_j$ represents an anisotropy energy between neighbouring Fe atoms mediated by Pt atoms, called two-ion contribution term. This is more dominant than uniaxial anisotropy term and depends on the strength of the effective exchange field induced by Fe calculated as:

$$d^2_{ij} = k^0_{\mathrm{Pt}} \left(\frac{1}{H_\nu} \right)^2 \sum_\nu J_{i\nu} J_{j\nu}. \tag{5.4}$$

In reference [119] it is discussed about the model used for the exchange energy calculations using constrained density functional (CDF) theory. Due to the interaction of $5d$ Pt and $3d$ Fe, the exchange exhibits some particular aspects like oscillatory behavior and a differential between plane and perpendicular components of the exchange.

This Hamiltonian gives good agreement with experiment for the Curie temperature and the magnetisation scaling of the anisotropy (important for HAMR) but it involves many nearest neighbours (NN) and is computationally intensive. Here, we aim to retain the same physical features with a simplified Hamiltonian which is faster for computation.

5.1.2 RKKY parametrization based on Mryasov model

In the following section we present a method to evaluate the exchange interaction between atomic sites using a function derived on a quantum mechanical basis. This is an indirect method of quantification of the interactions between localized moments such as $3d$ metals. This function is known as RKKY interaction summarizing the initial letters of the surnames who discovered this effect: Ruderman, Kittel, Kasuya and Yosida.

As is presented by Blundell in reference [120], the magnetic susceptibility depends on the electron density of the gas as follows [120]:

$$\chi(\mathbf{r}) = \frac{1}{(2\pi)^3}\int d^3\mathbf{q}\chi_q, e^{i\mathbf{q}\cdot\mathbf{r}} \tag{5.5}$$

where $\mathbf{q}$ is the magnon wave vector. By solving the integral (5.5) a function can be obtained similar to equation (5.6) on the assumption of $k_f^{-1} \ll r$. The formalism of obtaining RKKY function has been detailed in Appendix B giving the following expression:

$$J(r) = J_0\frac{cos(k_f r)}{r^3}, \tag{5.6}$$

where J_0 represents the exchange value with the nearest neighbors (NN), k_f strongly depends on lattice properties of the magnetic material such as: lattice parameter, crystal order and valence. For an fcc structure, the Fermi wavevector can be calculated as: $k_f = (12\pi^2/a^3)^{1/3} \approx 4.90/a$ as shown in reference [121], where a is the lattice parameter.

Prior to constructing an RKKY model for hybrid FePt atoms, we observed a similarity between the RKKY function shown in equation (5.6) and the predictions of the Mryasov model. Both functions are oscillatory and dependent on the separation between atoms, therefore we used DFT data in order to find an appropriate wave vector k_f by fitting the exchange values from first principle calculations. The Fermi wave vector k_f is essential in order to tune the period of the exchange oscillation as shown in equation (5.6).

The RKKY approach was initially developed to describe the nuclear magnetic moment [122] and then was expanded to describe the magnetic interaction in metals and non-metals. As shown in figure 5.2 the exchange values for different separations can be mapped onto the RKKY function, however it is challenging to find the most accurate value for k_f in order to have the best fit. Therefore, we present in this work a comparison of the RKKY function with the full range Mryasov Hamiltonian in order to validate this model of exchange.

We employed the atomistic spin model which is based on the Heisenberg Hamiltonian as follows:

$$\mathscr{H} = \mathscr{H}_{ex} + \mathscr{H}_{ani}, \tag{5.7}$$

Here, $\mathscr{H}_{ani}$ represents the anisotropy term of the Hamiltonian which can be calculated as $\mathscr{H}_{ani} = -k_u \sum_i (\mathbf{S}_z^i \cdot \mathbf{e})^2$ where k_u is the perpendicular anisotropy constant per atom and **e** denotes the direction of the anisotropy axis along **z** direction.

The exchange parameter depends on the separation distance between the atoms, where the exchange can be ferromagnetic or antiferromagnetic as shown in figure 5.2. The number of interactions per atomic bond increases with the radius. Therefore, for a radius of one unit cell size the number of interactions per atomic bond is 26. Second order will generate 130 interactions whilst the 5th order will generate 1978 interactions.

The exchange term per atomic bond i is calculated using equation (5.8) where $J_{ij}(r)$ is considered a first order tensor

$$\begin{aligned}\mathscr{H}_{ex}^i &= -\sum_j J_{ij}(r)\mathbf{S}_i \cdot \mathbf{S}_j \\ &= -\sum_j \begin{pmatrix} S_x^i & S_y^i & S_z^i \end{pmatrix} \begin{pmatrix} J_{xx} & 0 & 0 \\ 0 & J_{yy} & 0 \\ 0 & 0 & J_{zz} \end{pmatrix} \begin{pmatrix} S_x^j \\ S_y^j \\ S_z^j \end{pmatrix},\end{aligned} \tag{5.8}$$

where j is the number of interaction with the neighbors which depends on the range of the cut-off r as mentioned above, J_{xx}, J_{yy}, J_{zz} are the elements of the isotropic tensor $J_{ij}(r)$ which are calculated according to equation (5.6) as:

$$\begin{cases} J_{xx} = J_x^0 \frac{cos(k_f r)}{r^3} \\ \\ J_{yy} = J_y^0 \frac{cos(k_f r)}{r^3} \\ \\ J_{zz} = J_z^0 \frac{cos(k_f r)}{r^3} \end{cases}. \tag{5.9}$$

$J_{x,y,z}^0$ represents the exchange value constants with the nearest neighbors (NN) which can be extracted from Mryasov data by fitting them shown in figure 5.2. We noted a slight difference between in-plane exchange value $J_{x,y}^0$ comparing with out of plane component J_z^0. Here, $J_x^0 = J_y^0 < J_z^0$ where $\frac{J_z^0 - J_{x,y}^0}{J_z^0} = 4.8\%$. This small difference generates an analogous

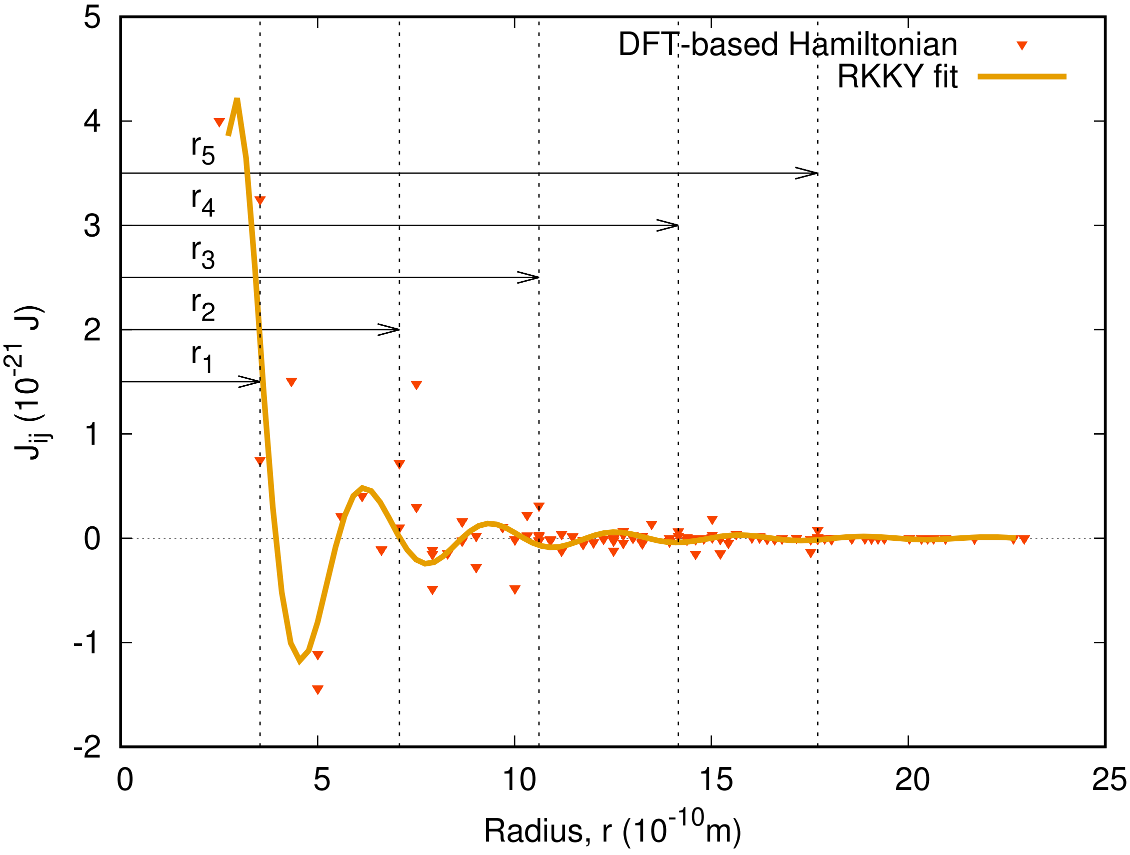

Fig. 5.2 The values of exchange constant as a function of distance for first principle calculations. The solid line represents the fit using equation (1) giving a value for k_f around $0.98\,\mathrm{nm}^{-1}$. We investigated 5 ranges of truncation for the full DFT-based Hamiltonian . Here $r_{1,2,5}$ sweeps 26, 130, and 1978 interactions.

of two-ion contribution given by Mryasov Hamiltonian, which is essentially an exchange anisotropy. This has a remarkable impact into the anisotropy rescaling shown later in this chapter. Beside this, Hinzke *et al.*[100] demonstrated different domain wall widths in-plane and perpendicular due to this special form of the Hamiltonian.

5.2 Comparison of Tc distributions

We modeled a cylindrical grain of L1_0 FePt with a lattice parameter of 2.5 Å. The magnetic moment has been set at $3.2\mu_B$ which gives a saturation magnetisation of $M_S = 2.127\times10^6\,\mathrm{JT}^{-1}/\mathrm{m}^3$. The simulations have been performed using Constrained Monte-Carlo method described in reference [59]. We performed 10,000 Monte-Carlo steps to equilibrate the system and another 10,000 steps at every 10 Kelvin temperature step in order to average the magnetic properties.

Our starting point is the determination of the period of the exchange oscillation. This was done by calculating a series of M vs. T curves varying k_f in order to obtain a reliable Curie temperature according to first principle calculations data. In figure 5.3 is plotted a series of M vs. T curves for three different values of Fermi wave vector in comparison with DFT values of the exchange. A reasonable agreement between RKKY function and DFT values is obtained for a value of $k_f = 1.0\,\mathrm{nm}^{-1}$ which is close to the value obtained from the fit shown in figure 5.2. An increased value of k_f leads to a decrease of T_C of FePt. Consequently, we can find numerically the value of the Fermi wave vector giving the best fit to the DFT results.

Another important topic in creating the neighbour list is to take into account a maximum cut-off range in order to maintain an optimal balance between accuracy and the speed of the calculations. Here, an extended list of neighbour implies longer time spent on calculations. Thus, we can tune the length of neighbours list by selecting a specific maximum range of interaction as it has been mentioned early in this chapter. Maximum accuracy will be obtained for a higher range such as 5 u.c. size but at lower ranges the accuracy might oscillate. This is illustrated in figure 5.4 where a series of M vs. T are plotted at different cut-off radii. There is a clear deviation of the third range in comparison with the full range whilst the second range gives more accurate shape of the curve. Another aim of these simulations is to give an explanation of the different truncations. Third order is an example of reducing the T_C due to the truncation of the neighbours list.

The understanding of how Curie temperature depends on the grain size is fundamental when we consider a realistic and feasible model of HAMR in simulations due to the requirement of small sizes of the grains. Early research by Fisher and Barber [123] demonstrated for the first time the scaling theory at finite thickness of a ferromagnet. A reduction of the Curie temperature is expected as the thickness of the film is reduced. A new scaling law is introduced in reference [123] in order to describe how the Curie temperature varies with the thickness of the film given by following the equation [123, 124]:

$$\frac{T_C(\infty) - T_C(t)}{T_C(\infty)} = (n/n_0)^{-\lambda}, \tag{5.10}$$

where $T_C(t)$ is the Curie temperature for a given thickness t of the film and $T_C(\infty)$ is the value of the Curie temperature. The shifting exponent $\lambda = 1/\nu$ describes the variation of T_C with the microscopic thickness t. The finite size effects in L1_0 FePt have been studied by Hovorka *et al.* [125] using the nearest neighbours approximation (NN) which implies to set an isotropic exchange value constant calculated and the full DFT Hamiltonian described

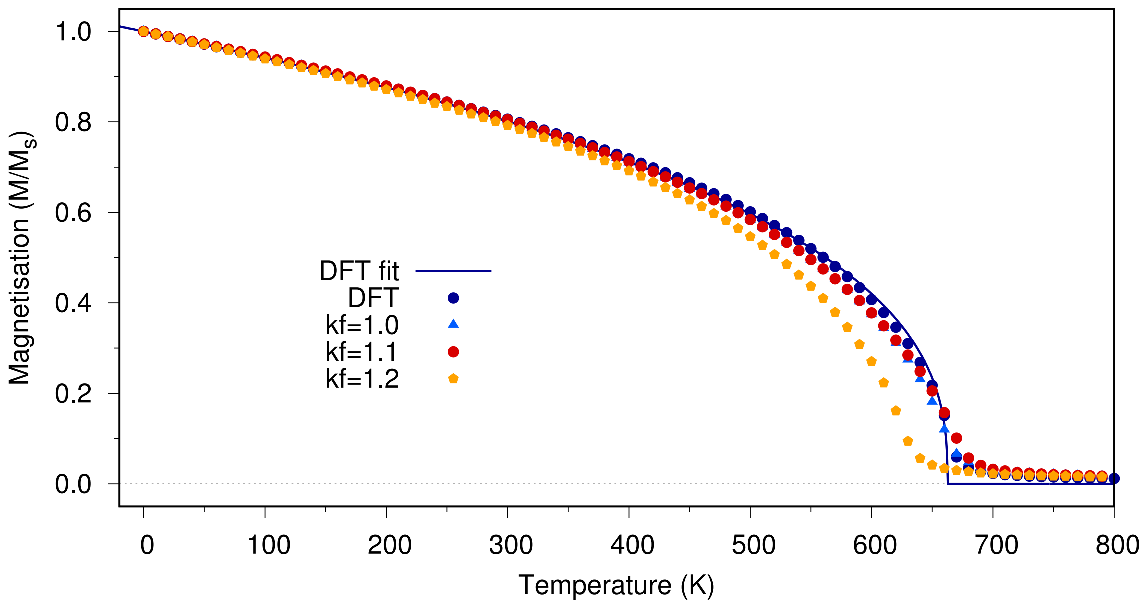

Fig. 5.3 The M vs. T curves of 10 nm height FePt cylinder for different values of k_f. The solid line represents the fit of DFT data using equation (5.11) giving an exponent $\beta \approx 0.37$.

above. The Mryasov Hamiltonian gives more accurate results of the shifting exponential than the NN approximation as confirmed by the experimental measurements done by Rong *et al.* [126].

In the following we describe a series of temperature magnetisation dependences with emphasis on the distribution of the Curie temperature at different sizes and truncation ranges. Here we model a 10 nm height FePt cylinder varying the basal diameter from 2 nm to 11 nm using both exchange interaction models described in the previous section of this chapter.

Figure 5.5 shows a series of temperature magnetisation curves for different diameters of the cylindrical system at different cut-off ranges using *ab-initio* values for exchange interactions. These curves are calculated with the Monte-Carlo (MC) method by performing 50,000 MC steps to equilibrate the system and another 100,000 MC steps in order to average the magnetic properties at each value of temperature with a step of 10 K. Larger radii of the particle will lead to an asymptotic decrease of the magnetisation once the temperature approaches the Curie point. This is demonstrated in figure 5.5(d) where the radius of the

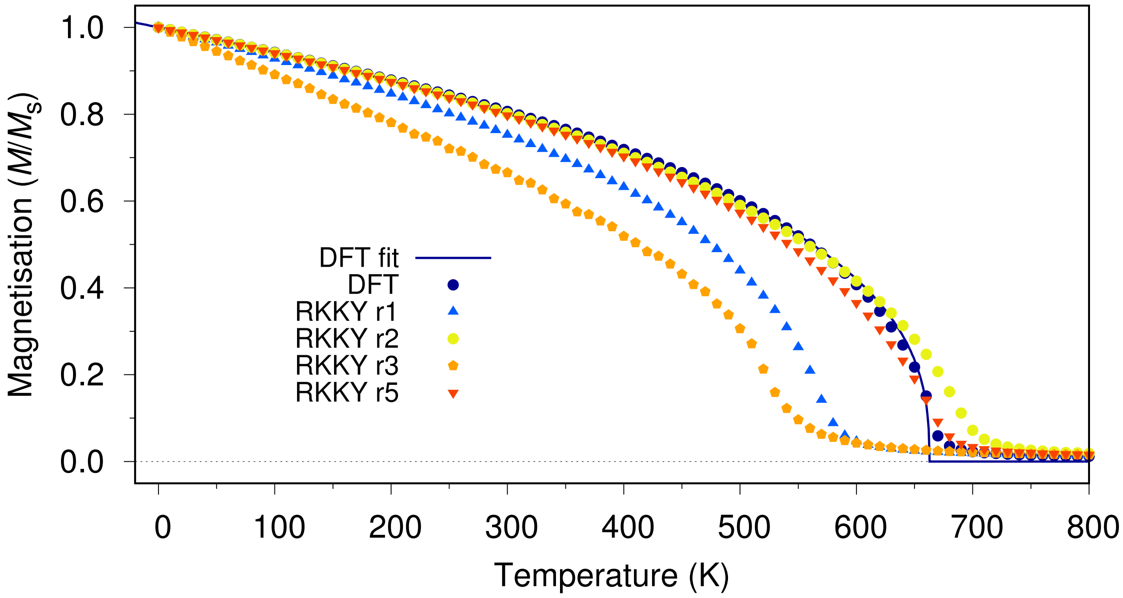

Fig. 5.4 The M vs. T curves of 10 nm height FePt cylinder for different radii of cut-off according to figure 5.2 using RKKY function and DFT values. The solid line represents the fit of DFT data using equation (5.11).

cylinder has been set 11 nm comparing with figure 5.5(a) where the radius of cylinder is 3 nm.

For all cases the different ranges of the cut-off give different shapes of M(T) dependence due to an overestimation or underestimation of the exchange values as a result of the balance between ferromagnetic and antiferromagnetic interactions. Here, the first order gives unrealistic shapes of the M(T) independently of the sizes. However, a reasonable agreement is obtained for the second being closer to the full range which gives a good advantage in terms of speeding-up the calculations.

Figure 5.6 shows the temperature magnetisation dependences M(T) for different ranges of cut-off at different sizes of the diameter using RKKY method for the exchange calculations. The simulations are performed in the same approach as in the previous case by splitting the interactions list from first range up to the fifth range. Again, the same unrealistic results are obtained for the first range as we obtained before. However, at an increased radius of the

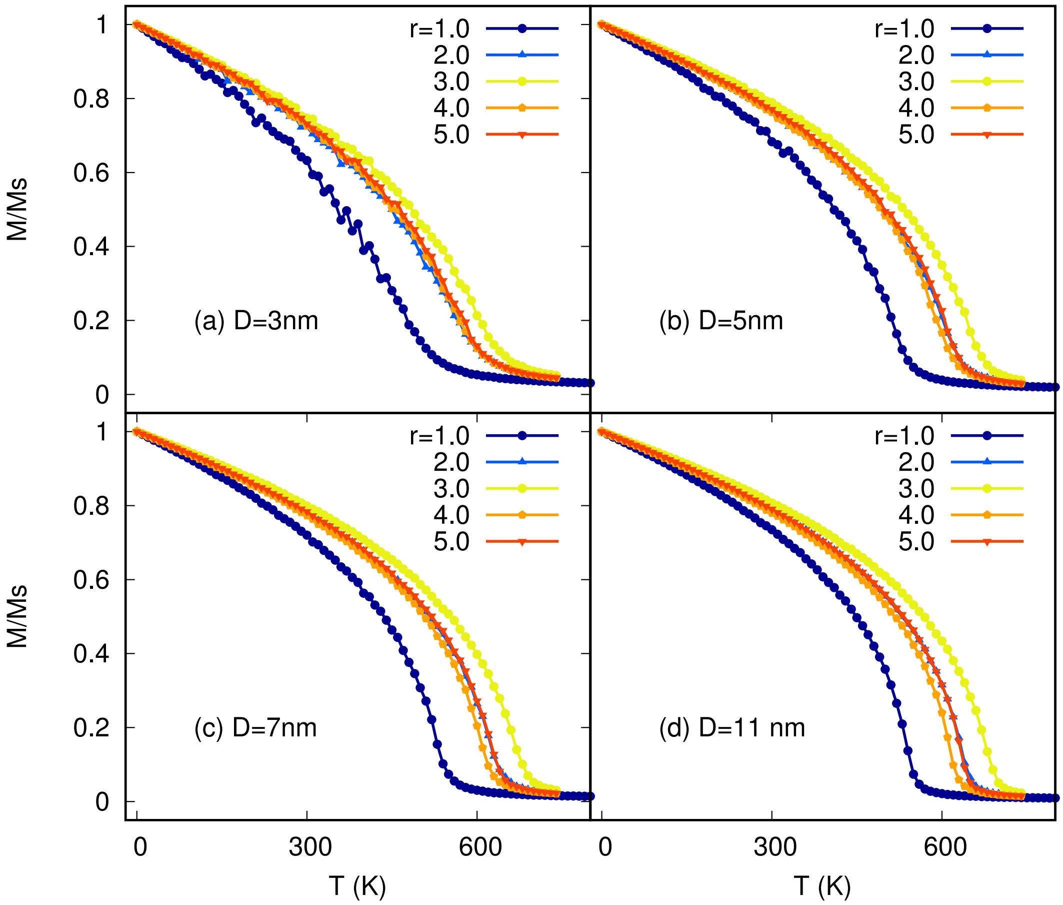

Fig. 5.5 Plotts of a series of M(T) curves for different truncations and radii of the 10 nm height FePt cylinder using Mryasov values for the exchange interaction list.

particles, the shape and the value of the Curie temperature converge giving an quantitative agreement between these two methods: RKKY and DFT case.

An elegant method to extract the Curie temperature is to fit the M(T) curves using classical fit expression given by following equation:

$$m(T) = (1 - T/T_c)^{\beta}, \tag{5.11}$$

where β is the classical exponent. This will give an accurate estimation of the Curie temperature for each M(T) dependence, therefore we performed the fitting for all cases of different sizes and radii.

Figure 5.7 shows the distribution of the Curie temperature dependence on the system diameter at different ranges. The distribution of Curie temperature using the DFT-based

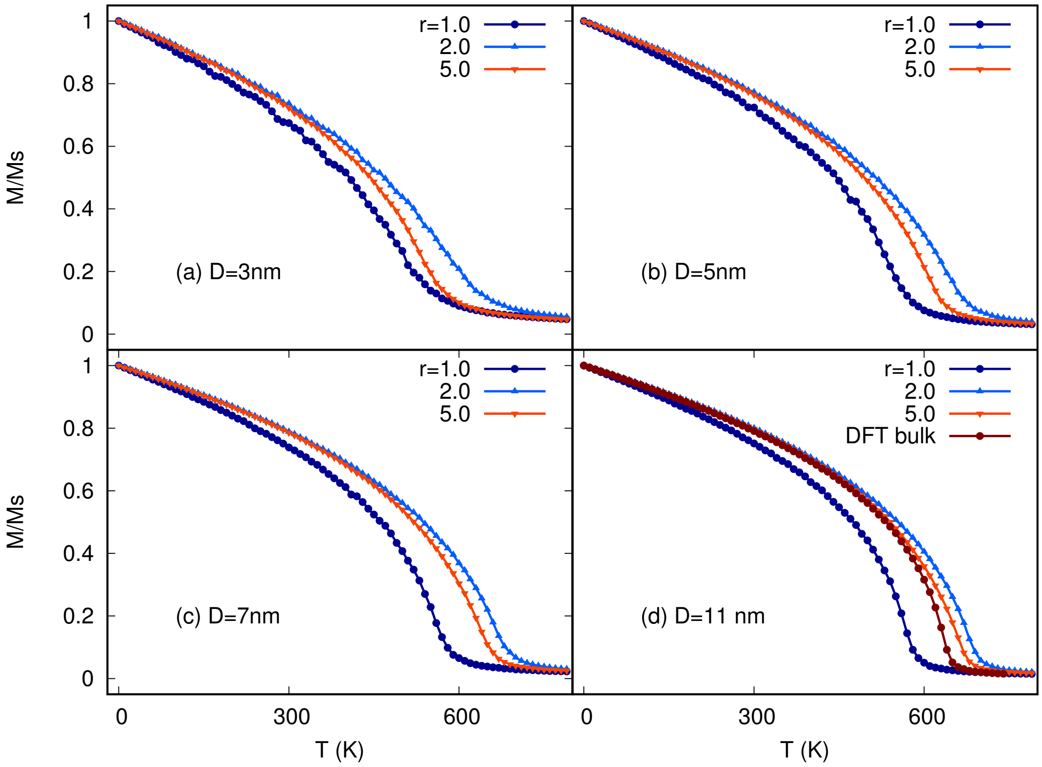

Fig. 5.6 Magnetisation as a function of temperature for different diameters of FePt cylinder and different cut-off ranges using RKKY model of exchange.

Hamiltonian can be seen in figure 5.7 (a) and for RKKY function is shown in figure 5.7 (b). Both models exhibit similar size variations of the Curie temperature as previous calculations done by Hovorka *et al.* [125].

In order to explore the magnetic behavior at lower sizes we fit each dependence of Curie temperature on diameter D using the following finite size scaling law [125, 123, 124]:

$$T_C(D) = T_C^{\mathrm{bulk}} \left[1 - \left(\frac{d_0}{D} \right)^{\nu} \right], \tag{5.12}$$

where ν is the phenomenological shift exponent and d_0 is the parameter related to unit cell size. For a better fitting we calculated the T_C^{bulk} by simulating a particle with 15 nm diameter using boundary conditions. This will give the bulk value for each range case which can be introduced in the fitting function (5.12). With this equation we proceed with the fitting of the size dependence in order to compare the critical exponents for both models. However, later research done by Waters *et al.* [127] demonstrated a strong dependence of ν with different factors such as the applied field for example. Another factor which might affect the size distribution of the Curie temperature can be related to the shape of the particle. However, further work is required in order to find a best fit by introducing new correction factors. For simplicity, in the absence of the applied field we used the equation (5.12) to extract the exponents which are summarized in the Table 5.1.

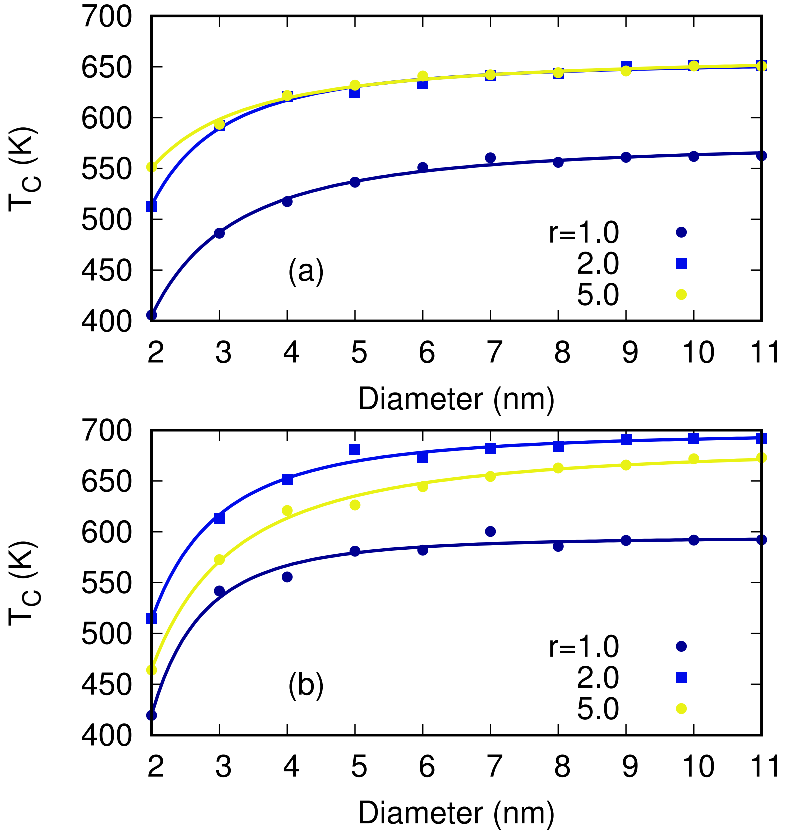

Fig. 5.7 The size distribution of Curie temperature for different ranges of cut-off. The solid lines stands for the fitting using equation (5.12). Graph (a) shows the size distribution using DFT-based Hamiltonian , respectively graph (b) corresponds to RKKY model.

Model	DFT-based			RKKY		
Range	r_1	r_2	r_5	r_1	r_2	r_5
T_C^{bulk} (K)	576.27	655.84	661.70	594.55	698.29	682.04
ν	0.62	0.53	0.71	0.37	0.49	0.61

Table 5.1 The bulk T_C and critical exponent ν for both model at different ranges of cut-off. The values have been obtained by fitting the graphs from figure 5.7 using equation (5.10)

We observed reasonable results for both model for higher range of cut-off (e.g. 5u.c.) giving a T_C^{bulk} close to experimental value of 775 K [126] and the exponent ν which experimentally has been found around 0.91 while the classical Heisenberg approach will give a value for the exponent at 0.71. However, the exponent ν and T_C^{bulk} decreases inconsistently with full range of the Hamiltonian for both cases which is essentially in the understanding of the demagnetisation processes at lower sizes where different truncations can appear due to the length of the particles. Therefore, a particle whose dimensions are below 3 nm cannot incorporate the full range Hamiltonian . Hence, the truncation can appear not only in computational model but also in reality.

5.3 RKKY finite size anisotropy scaling

Crucially in understanding of the highly ordered $L1_0$ FePt it is important to know the temperature behavior of the magnetic properties. Early theoretical studies done by Callen *et al.* [128] developed a theoretical framework to calculate the temperature dependence of different magnetocrystaline anisotropies suggesting a scaling of the anisotropy with the reduced magnetisation at sufficiently low temperatures following a power law as follows:

$$\frac{K(T)}{K(0)} = \left[\frac{M(T)}{M(0)}\right]^{l(l+1)/2} \tag{5.13}$$

Equation (5.13) clearly shows a faster reduction of the anisotropy energy than the magnetisation for a certain temperature given that most of the ferromagnets $l(l+1)/2 > 1$. Here, for the uniaxial anisotropy the exponent $n = l(l+1)/2 = 3$ while for the cubic anisotropy $n = 10$.

Extensive studies have been done on FePt thin films [129–131] aiming to understand the dependence of fundamental magnetic properties on the manufacturing factors such as temperature, doping, deposition rate and many others. Interestingly, $L1_0$ FePt presents some unexpected anisotropy temperature dependence due to the chemical ordering. Okamoto *et al.* [132] measured experimentally the dependence of the first order anisotropy K_1 with the temperature using Hall effect detailed in reference [98]. They reported an exponent for thin layer $L1_0$ FePt about $n = 2.1$ which it was suggested might be related to chemical ordering, lattice expansion due to the thermal fluctuations or higher order anisotropy.

Mryasov *et al.* showed that FePt has a dominant two-ion anisotropy arising from exchange anisotropy giving a scaling factor $n = 2.1$ which is close to the expected value from Callen and Callen of $n = 2$. Later, Asselin *et al.*[59] demonstrated the capability of the CMC method to reproduce the experimental anisotropy scaling results by using Mryasov[119] values for exchange interaction. The essential part of 2.1 scaling factor is the existence of the two-ion anisotropy part into the general Hamiltonian which gives unusual torque curves and free energy dependence during the switching mechanism.

In the following we investigate the anisotropy temperature scaling using the CMC method to calculate the restoring torque from 0° to 180° with a step of 5°. The torque curves enable determination of the free energy curves of the system by integrating the curve along the polar angle. This procedure is similar with the approach presented by Evans *et al.* in reference [102] where the free energy can be calculated via following equation:

$$\Delta F = \int_0^\theta \mathscr{T} d\theta, \tag{5.14}$$

where $\mathscr{T}$ is the restoring torque at a specific polar angle between magnetisation and easy axis denoted by θ.

A typical series of free energy curves with varying the temperature is illustrated in figure 5.8. Here, the DFT-based Hamiltonian exhibits some anomalies due to the two-ion anisotropy [119] term as shown in figure 5.8(a) where a deviation from classical $\sin(2\theta)$ can be observed. This is likely caused by elliptical domain wall propagation giving a null net torque when the axis of the magnetisation approaches the hard axis. The same unusual angular dependence of free energy, also can be accurately reproduced by the RKKY function if we introduce a small difference between in-plane component of exchange and z-component which brings in the two-ion contribution part in our Hamiltonian. In figure 5.8 is shown a similar dependence of the reduced free energy with the polar angle θ due the modified exchange. Here, we set a vectorial case for the exchange calculation discussed early on this chapter. Therefore, the z-component is $J_{zz} = 5.82 \times 10^{-21}$ J and in plane component $J_{xx,yy} = 5.6 \times 10^{-21}$ J. It both cases DFT and RKKY we can see the flattening of the free energy curve shape which denotes a lower energy barrier than expected for coherent rotation.

A series of snapshots can be seen in the figure 5.9 at different angles during the switching process using the RKKY mechanism for the exchange at a simulation temperature of 200 K. We observed a clear nucleation at $\theta = 90°$ suggested in figure 5.9 (c) by the different colors of the spins. Here blue color denotes a parallel orientation whereas the red color indicates an anti-parallel orientation. This behavior of nucleation has been previously identified by Hinzke *et al.* [100] using Mryasov data for the exchange. This will lead to incoherent reversal resulting in a decrease of the energy barrier as shown in figure 5.8.

With these results we can extract the anisotropy at each temperature value by calculating the energy barrier per volume. Figure 5.10 shows the scaling of the reduced anisotropy K/K_0 with reduced magnetisation M/M_S, where K_0 is the bulk anisotropy. Two cases are studied using the RKKY mechanism in order to understand the impact of the two-ion anisotropy

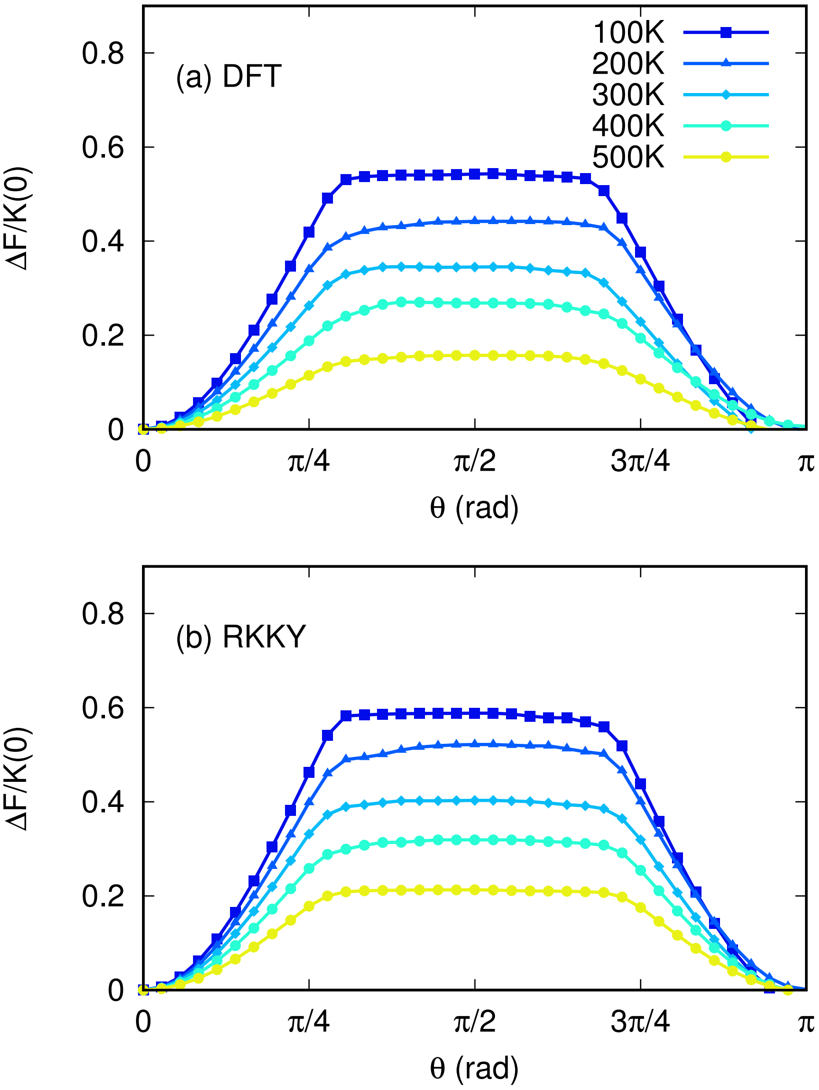

Fig. 5.8 Plot of the free energy curves for a 10 nm height FePt cylinder with a basal diameter of 10 nm as a function of the polar angle θ using full (a) DFT-Hamiltonian and (b) RKKY function up to 5 u.c. range at different temperatures.

on the anisotropy rescaling; the first case corresponds to single-ion anisotropy where all components of the exchange tensor are have the same value ($J_{xx} = J_{yy} = J_{zz}$) and in the second case is taken in account the two-ion anisotropy using the introduction of the anisotropic exchange mentioned above.

After the linear fitting we found a scaling factor of $2.53 \pm 1.67\%$ for RKKY single ion, respectively $2.2 \pm 0.97\%$ for two-ion RKKY which is in a reasonable agreement obtained experimentally [132] and theoretically [119, 59].

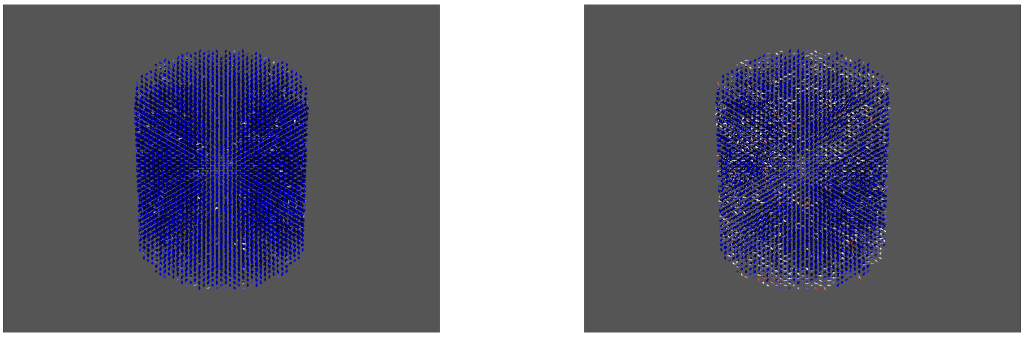

(a) $\theta = 0^\circ$

(b) $\theta = 45^\circ$

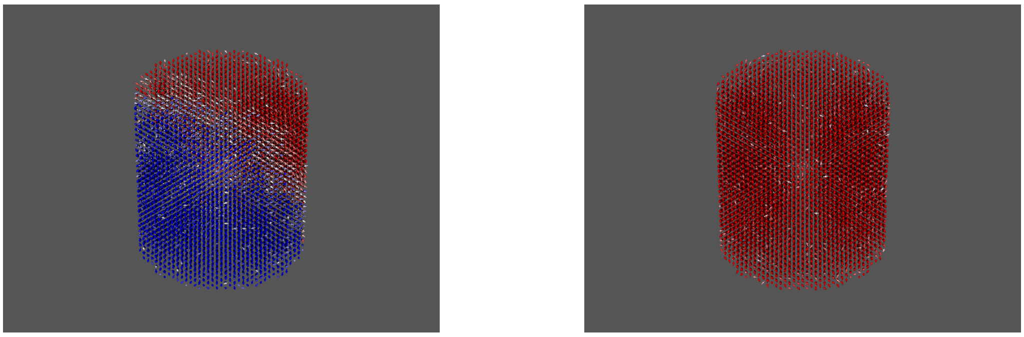

(c) $\theta = 90^\circ$

(d) $\theta = 180^\circ$

Fig. 5.9 Typical snapshots of the spins configuration during the switching mechanism at different polar angles θ for a cylindrical grain of FePt with 10nm height and 10nm basal diameter at a temperature of 200K.

The nucleation and propagation mechanism introduces a systematic error when is found using the method of extracting the anisotropy from the free energy path due to nucleation. We can, therefore design a new way of extracting the anisotropy energy of the system in the maximum torque value before the appearance of strong effects caused by the nucleation. In the following simulations, the magnetisation angle is set at $\theta = 45^\circ$ and the temperature varies in the interesting regime of HAMR from 0K. This is demonstrated in the inset of figure 5.11 where the linear fitting is shown for different diameters of the FePt.

However, the scaling factor can be influenced by the sizes, strength of the two-ion anisotropy and the shape of the particles will likely give a rise to an increase of the two-ion anisotropy with small sizes.

Figure 5.11 shows the variation of the scaling factor as a function of diameter. We fitted each log-log dependence at different diameters of the FePt cylinder extracting the scaling factor. Lower size will give a significant deviation comparing with bulk value which might be related to finite size effects.

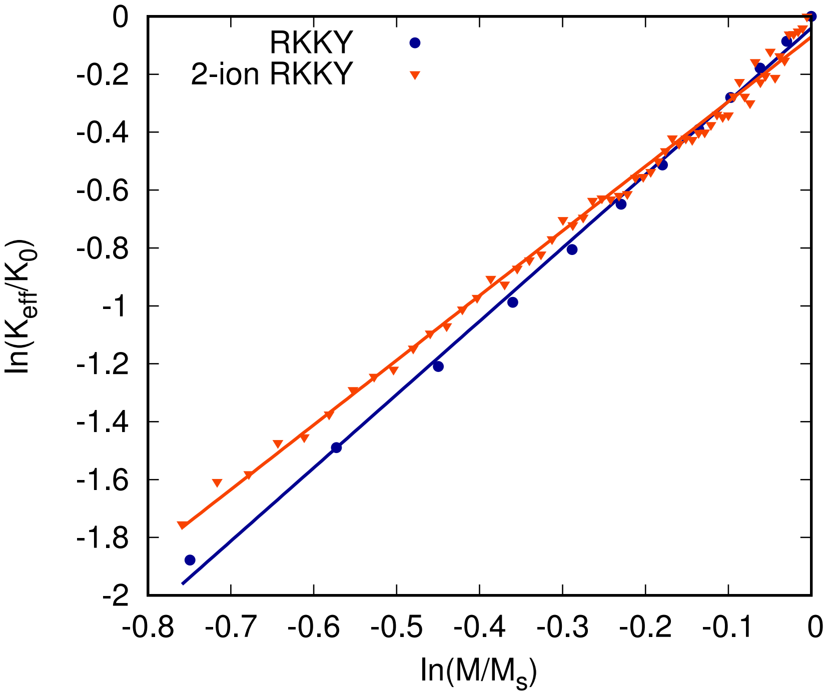

Fig. 5.10 In this graph is plotted the calculated temperature dependence of L1$_0$ FePt in log-log plot of the reduced anisotropy and magnetisation using RKKY function for two cases: single ion contribution and tow-ion contribution. The linear fit gives a slope $n = 2.2 \pm 0.97\%$ for two-ion contribution and $n = 2.53 \pm 1.67\%$ for single ion.

5.4 Computational performance and new perspectives

To find out the benefits of a short range Hamiltonian such as the first or second range the performance of each truncation at different system sizes has been evaluated. Three ranges of Hamiltonian have been simulated in figure 5.12 performing 100.000 Monte-Carlo steps for an arrangement of atoms in a fcc structure for a cubic particle of FePt. Here the 5th range is closer to full Hamiltonian list in terms of number of neighbouring atoms which should be similar in terms of calculation speed. A clear increase of time can be observed with an increased number of atoms for all ranges. However, the time for the fifth range is considerably longer at larger size of the particle where the second range can be accurate and fast as well.

For lower number of atoms, the running time converge for all cases due to the reduced list of interactions for the fifth range. Similar behaviour has been noted at different system truncations where the system cannot provide enough atoms to fill the entire list of the interactions.

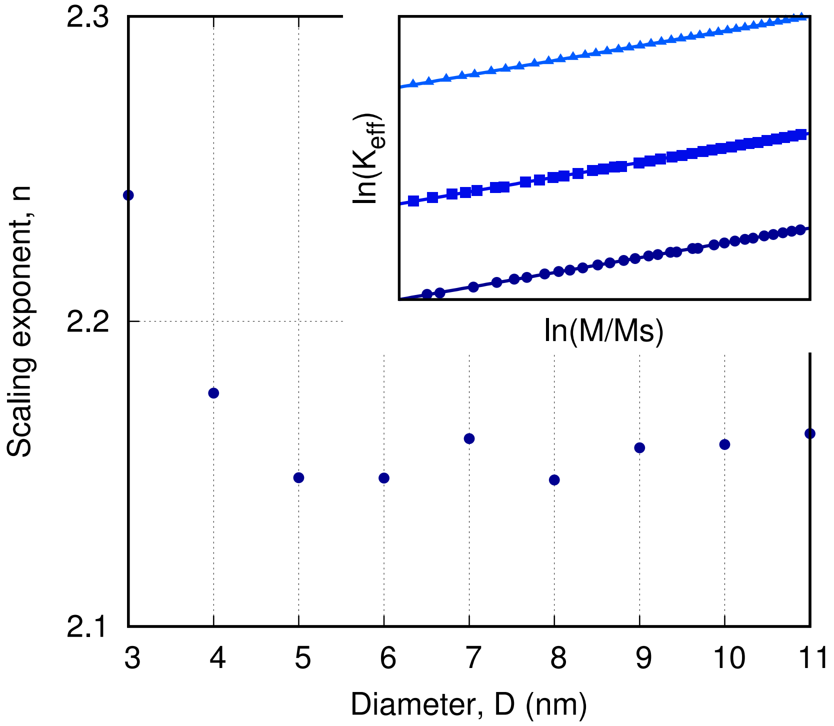

Fig. 5.11 In this graph is plotted the scaling factor n as a function of diameter of $L1_0$ FePt cylinder using RKKY function with two-ion contribution. The inset graph shows the scaling of K with M/M_S for three different values of the diameter.

Beside speeding up the calculations the implementation of RKKY function can be an useful tool to simulate magnetic properties of ferromagnets which exhibit anomalous crystal structures or oscillatory exchange interaction. This method allows to tune the specific parameters in order to compensate the lack of insight about the materials. For example, an expanded investigation can be done to understand how the strength of two-ion anisotropy which can be controlled by tuning the exchange interaction components can affect the anisotropy scaling.

5.5 Conclusions and further work

To summarize, we have investigated two models of exchange interactions employing atomistic spin model. Both model predict a reasonable temperature dependence which might be useful for developing the new models for magnetic materials aiming to describe the magnetisation processes involved in recording media. We noted an advantage of DFT model over RKKY model due to the extra term of anisotropy which gives reliable results in agreement with the experiment. However, the full Hamiltonian can be painful to use and as an alternative the

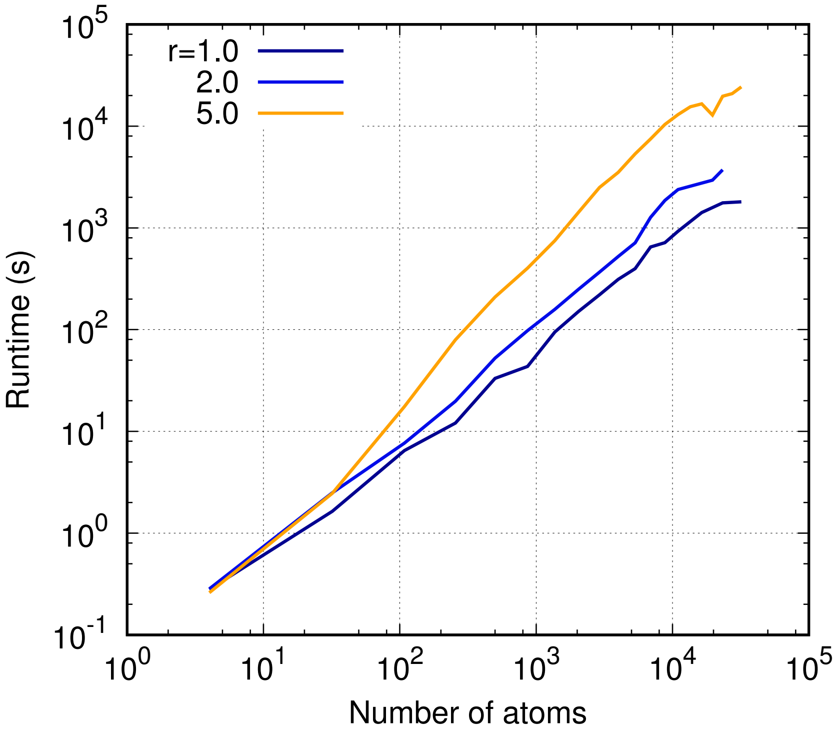

Fig. 5.12 Runtime for different ranges of RKKY function as a function of number of atoms. The time has been measured for each simulation which perform 100000 Monte-Carlo steps at each system size.

RKKY model can be used in order to increase the speed of simulations mantaing the accurate physical properties of FePt.

Secondly, the magnetic behaviour at lower sizes can be related to truncation of the Hamiltonian. Here, both model predicted a reduction of T_C when the range of the interaction is less than 3 unit cell sizes. We found a good agreement between RKKY two-ion and DFT-based for calculation of the anisotropy scaling factor which provide a better insight of $L1_0$ FePt toward heat assisted recording media (HAMR). RKKY mechanism of the exchange interaction provides a reasonable description of the anisotropy scaling with magnetisation showing a scaling factor close to the experimental measurements in the same way that Mryasov model works showing the contribution of the two-ion anisotropy term.

We conclude that FePt is a unusual ferromagnet where anisotropic exchange interactions occur giving a rise to an additional term in the general Hamiltonian called two-ion contribution. Here, we need to explore how the strength of the two-ion anisotropy can affect the scaling factor remaining as further work.

Chapter 6

Conclusions and further work

Atomistic Spin Dynamics model

In this final chapter of the thesis, we briefly draw the main conclusions of this thesis pointing out the main results we found. Throughout the three topics we approached in this work we employed the ASD model to simulate the magnetic properties proved as an useful and reliable model being successfully implemented in VAMPIRE atomistic package. The importance of ASD is given by the capability of reproducing thermal bahaviour of magnetic nano-materials in a strong agreement with the experimental measurements by using Langevin dynamics. Two techniques of solving the dynamics of the spins have been presented such as: stochastic LLG equation and MC methods. Both methods give a correct thermal dependence of the magnetisation under different simulations conditions standing up for the simulations of HAMR processes.

Inter-granular exchange

In the third chapter, the inter-granular exchange interaction is studied in detail by simulating two different granular systems: the tri-layer and multi-granular system arranged in a hexagonal distribution. CMC simulations show an exponential decrease of the inter-granular exchange constant on separation distance between the grains on both cases according to Sokalski measurements. In the tri-layer system we observed a decrease of the exchange interaction energy with the temperature and low magnetic impurities density of the segregant layer.

The multi-grain simulations reveal a slight different form of the inter-granular exchange unlike trilayer system where the normal Heisenberg exchange is enough to depict the behaviour of exchange during a switching mechanism of the top grain. On the other hand in hexagonal distribution of the grains, the switching of the central grain does not respect the Heisenberg form of the exchange where an additional term must be included in order to appropriately describe the angular dependence of the exchange energy. This term is a higher order exchange usually called biquadratic term due to $\sin^2$ dependence demonstrated theoretically and experimentally by Sloncweski *et al.* The strength of the bilinear and biquadratic term have been found to decay exponentially on temperature and separation distance for anisotropy and non-anisotropy grains. Also, the doping concentration affects the strength of the inter-granular exchange influencing the exponent of power law decreasing on temperature. All these results can contribute to a better understanding of the long-term stability of recording media, particularly for heat assisted magnetic recording.

As a further work we are interested to investigate the same inter-granular exchange energy by replacing the Co grains with ECC grains. This can complicate the simulations and reveal unexpected effects due to particular nucleation processes which can alter the inter-granular exchange.

ECC media

In the fourth chapter, a new design of recording medium has been proposed for investigations being a solution to overcome some thermal limitations of HAMR. ECC media has been studied both using MC simulations and sLLG equation. Special interest has been dedicated to find out the benefits of ECC design which suppose to be feasible for HAMR due to the exchange spring effect which might "help" the switching at conventional parameters. The atomistic simulations show a good qualitative temperature dependence of the coercivity compared with the experimental results revealing a decrease of the writing field at elevated temperatures due to the reduction of the energy barrier at high thermal fluctuations.

The CMC simulations predict a diminution of the energy barrier with an increased temperature making the ECC media suitable for HAMR temperature regime. However, CMC simulations do not predict a realistic decrease of the energy barrier with an increased applied field on the low-temperature regime due to a coherent rotation of the magnetisation of the atomic layers in the system. We expected the nucleation to occur during the reversal mechanism according to dynamical simulations where the nucleation field alters energy barrier. It has been found that the nucleation appears at elevated temperature using CMC simulations, where the spins are allowed to fluctuate randomly in a wider angular cone of the magnetisation favouring the non-coherent rotation of the system. As further work, we can improve the energy barrier calculations by considering a new model of energy barrier calculations. This model is a semi-analytical model based on a set of Lagrange constraints which can be applied on magnetisation components.

The sLLG simulations give us a more detailed description of the exchange spring behaviour of ECC media. We found that the domain wall formation during the hysteresis loops effects the switching mechanism. Further observations have been done by studying the reversal mechanism. It has been noted an anomalous damping dependence in heating/cooling processes under external magnetic fields around the coercivity at different damping constant values of Fe. Here lower damping of the soft phase (Fe) is found to accelerate the switching in the low-field regime, whereas higher fields will give an expected dependence of the reversal time on damping denoting minimal effects of the nucleation caused by a faster propagation of the domain wall. Moreover, the nucleation effects in ECC media need to be considered in a further implementation of complex HAMR process and are determined by several factors including the strength of the applied field, temperature, exchange coupling at the interface and thickness of the soft layer. We conclude that the damping constant plays a crucial role in determining the speed of the domain wall propagation, explaining the unexpected results at conventional fields.

RKKY interaction

In the fifth chapter, two ways to parametrize the exchange interaction between the magnetic spins have been proposed: first principle calculations and RKKY function toward ASD simulations. Both methods predict a good agreement of the temperature dependence which is useful for developing new models for the magnetic materials aiming to describe the magnetisation processes involved in recording media. However, the full set of DFT calculations can be painful to use in order to create the interactions list and as an alternative RKKY model can be used in order to increase the speed of simulations by choosing an optimal range of truncation which ensures the reliable physical properties of the material.

Secondly, the magnetic behaviour at lower size can be related to natural truncation of the interactions list. Here, both models predicted a reduction of T_C when the range of interaction is less than three unit cell sizes. We found a good agreement between RKKY two-ion and DFT-based for calculations of the anisotropy scaling factor giving a better description of L1_0 FePt with great importance for HAMR as decreasing of the anisotropy on temperature is a fundamental factor prior to chose writing parameters. RKKY mechanism of the interactions provides a reasonable description of the anisotropy scaling with magnetisation showing a scaling factor close to the experimental measurements, 2.1, in the same way that Mryasov model works showing the influence of the two-ion anisotropy term.

We conclude that FePt is a complex ferromagnet where the unexpected exchange interactions occur giving rise to an additional term in the general Hamiltonian called two-ion contribution. Here, we need to explore how the strength of the two-ion anisotropy can affect the scaling factor remaining as further work.

Nomenclature

AD	Areal density
ASD	Atomistic spin dynamics
BCC	Body centred cubic
BER	Bit error rate
BPM	Bit patterned media
CDF	Constrained density functional
CGC	Coupled granular continuous
CLSDA	Constrained local-spin-density approximation
CMC	Constrained Monte-Carlo
DFT	Density functional theory
DM	Dzyaloshinskii-Moriya
EB	Electron beam
ECC	Exchange coupled composite
FCC	Faced centred cubic
FMR	Ferromagnetic resonance
FP	Fokker-Planck
GPGPU	General-Purpose Computing on Graphics Processing Units
HAMR	Heat-assisted magnetic recording

HDD	Hard disk drive
KKR	Korringa-Kohn-Rostoker
LD	Langevin dynamics
LLB	Landau-Lifshitz-Bloch
LLG	Landau-Lifshitz-Gilbert
MAMR	Microwave-assisted magnetic recording
MC	Monte-Carlo
MMC	Metropolis Monte-Carlo
MPI	Message-Passing-Interface
NN	Nearest neighbours
PMR	Perpendicular magnetic recording
RE	Rare earth
RKKY	Ruderman-Kittel-Kasuya-Yosida
SI	International system of units
sLLG	stochastic Landau-Lifshitz-Gilbert
SNR	Signal noise ratio
SQUID	Superconducting quantum interference device
SW	Stoner-Wohlfarth

References

[1] R F L Evans, W J Fan, P Chureemart, T A Ostler, M O A Ellis, and R W Chantrell. Atomistic spin model simulations of magnetic nanomaterials. *Journal of Physics: Condensed Matter*, 26(10):103202, 2014.

[2] Vincent Sokalski, David E. Laughlin, and Jian-Gang Zhu. Experimental modeling of intergranular exchange coupling for perpendicular thin film media. *Applied Physics Letters*, 95(10):102507, 2009.

[3] R F L Evans, U Atxitia, and R W Chantrell. Quantitative simulation of temperature-dependent magnetization dynamics and equilibrium properties of elemental ferromagnets. *Phys. Rev. B Condens. Matter*, 91(14):144425, April 2015.

[4] N. Ida. Engineering electromagnetics. *Berlin Heidelberg New York: Springer-Verlag*, 2004.

[5] K.J. Thurlow. Chemical nomenclature. *Berlin Heidelberg New York:Springer–Verlag*, 1998.

[6] C. D. Mee. *The physics of magnetic recording*, volume 2. North-Holland, 1964.

[7] Friedrich K Engel. 1888-1988: A hundred years of magnetic sound recording. *Journal of the Audio Engineering Society*, 36(3):170–178, 1988.

[8] Eric D Daniel, C Denis Mee, and Mark H Clark. *Magnetic recording: the first 100 years*. John Wiley & Sons, 1999.

[9] HJ Richter and A Yu Dobin. Angle effects at high-density magnetic recording. *Journal of magnetism and magnetic materials*, 287:41–50, 2005.

[10] D. Weller and A. Moser. Thermal effect limits in ultrahigh-density magnetic recording. *IEEE Transactions on Magnetics*, 35(6):4423–4439, Nov 1999.

[11] M. P. Sharrock. Time-dependent magnetic phenomena and particle-size effects in recording media. *IEEE Transactions on Magnetics*, 26(1):193–197, Jan 1990.

[12] D. Suess, S. Eder, J. Lee, R. Dittrich, J. Fidler, J. W. Harrell, T. Schrefl, G. Hrkac, M. Schabes, N. Supper, and A. Berger. Reliability of sharrocks equation for exchange spring bilayers. *Phys. Rev. B*, 75:174430, May 2007.

[13] Roger Wood. Future hard disk drive systems. *Journal of Magnetism and Magnetic Materials*, 321(6):555 – 561, 2009. Current Perspectives: Perpendicular Recording.

[14] M Mallary, A Torabi, and M Benakli. One terabit per square inch perpendicular recording conceptual design. *IEEE Transactions on Magnetics*, 38(4):1719–1724, 2002.

[15] Tadashi Yogi, Grace L Gorman, Cherngye Hwang, Michael A Kakalec, and Steven E Lambert. Dependence of magnetics, microstructures and recording properties on underlayer thickness in conicr/cr media. *Magnetics, IEEE Transactions on*, 24(6):2727–2729, 1988.

[16] SN Piramanayagam and K Srinivasan. Recording media research for future hard disk drives. *Journal of Magnetism and Magnetic Materials*, 321(6):485–494, 2009.

[17] RE MacDonald and JW Beck. Magneto-optical recording. *Journal of Applied Physics*, 40(3):1429–1435, 1969.

[18] Robert E Rottmayer, Sharat Batra, Dorothea Buechel, William A Challener, Julius Hohlfeld, Yukiko Kubota, Lei Li, Bin Lu, Christophe Mihalcea, Keith Mountfield, et al. Heat-assisted magnetic recording. *Magnetics, IEEE Transactions on*, 42(10):2417–2421, 2006.

[19] Christoph Vogler, Claas Abert, Florian Bruckner, and Dieter Suess. Landau-lifshitz-bloch equation for exchange-coupled grains. *Phys. Rev. B*, 90:214431, Dec 2014.

[20] Richard F.L. Evans. Hamr illustration, 2019.

[21] J. Zhu, X. Zhu, and Y. Tang. Microwave assisted magnetic recording. *IEEE Transactions on Magnetics*, 44(1):125–131, Jan 2008.

[22] H. J. Richter, A. Y. Dobin, R. T. Lynch, D. Weller, R. M. Brockie, O. Heinonen, K. Z. Gao, J. Xue, R. J. M. v. d. Veerdonk, P. Asselin, and M. F. Erden. Recording potential of bit-patterned media. *Applied Physics Letters*, 88(22):222512, 2006.

[23] H. J. Richter, A. Y. Dobin, O. Heinonen, K. Z. Gao, R. J. M. v.d. Veerdonk, R. T. Lynch, J. Xue, D. Weller, P. Asselin, M. F. Erden, and R. M. Brockie. Recording on bit-patterned media at densities of 1 tb/in^{2}and beyond. *IEEE Transactions on Magnetics*, 42(10):2255–2260, Oct 2006.

[24] R. L. White, R. M. H. Newt, and R. F. W. Pease. Patterned media: a viable route to 50 gbit/in/sup 2/ and up for magnetic recording? *IEEE Transactions on Magnetics*, 33(1):990–995, Jan 1997.

[25] B D Terris and T Thomson. Nanofabricated and self-assembled magnetic structures as data storage media. *Journal of Physics D: Applied Physics*, 38(12):R199–R222, jun 2005.

[26] Yasuhiko Tada, Satoshi Akasaka, Hiroshi Yoshida, Hirokazu Hasegawa, Elizabeth Dobisz, Dan Kercher, and Mikihito Takenaka. Directed self-assembly of diblock copolymer thin films on chemically-patterned substrates for defect-free nano-patterning. *Macromolecules*, 41(23):9267–9276, 2008.

[27] S. J. Greaves, Y. Kanai, and H. Muraoka. Magnetic recording in patterned media at 5–10 tb/in^2. *IEEE Transactions on Magnetics*, 44(11):3430–3433, Nov 2008.

[28] R F L Evans, R W Chantrell, U Nowak, A Lyberatos, and H-J Richter. Thermally induced error: Density limit for magnetic data storage. *Appl. Phys. Lett.*, 100(10):102402, March 2012.

[29] Y. Sonobe, D. Weller, Y. Ikeda, M. Schabes, K. Takano, G. Zeltzer, B. K. Yen, M. E. Best, S. J. Greaves, H. Muraoka, and Y. Nakamura. Thermal stability and snr of coupled granular/continuous media. *IEEE Transactions on Magnetics*, 37(4):1667–1670, July 2001.

[30] Y. Y. Zou, J. P. Wang, C. H. Hee, and T. C. Chong. Tilted media in a perpendicular recording system for high areal density recording. *Applied Physics Letters*, 82(15):2473–2475, 2003.

[31] Dieter Suess and Thomas Schrefl. Breaking the thermally induced write error in heat assisted recording by using low and high tc materials. *Applied Physics Letters*, 102(16):162405, 2013.

[32] D. Weller, A. Moser, L. Folks, M. E. Best, Wen Lee, M. F. Toney, M. Schwickert, J. . Thiele, and M. F. Doerner. High k/sub u/ materials approach to 100 gbits/in/sup 2/. *IEEE Transactions on Magnetics*, 36(1):10–15, Jan 2000.

[33] Shouheng Sun, C. B. Murray, Dieter Weller, Liesl Folks, and Andreas Moser. Monodisperse fept nanoparticles and ferromagnetic fept nanocrystal superlattices. *Science*, 287(5460):1989–1992, 2000.

[34] Sonja Stappert, Bernd Rellinghaus, Mehmet Acet, and Eberhard F. Wassermann. Gas-phase preparation of l10 ordered fept nanoparticles. *Journal of Crystal Growth*, 252(1):440 – 450, 2003.

[35] Stephen Blundell. *Magnetism in condensed matter*. Oxford Univ. Press, 2001.

[36] David Jiles. *Magnetism and Magnetic Materials*. CRC Press, 2016.

[37] Amikam Aharoni. *Introduction to the Theory of Ferromagnetism*, volume 109. Clarendon Press, 2000.

[38] W Heisenberg. Zur theorie des ferromagnetismus. In Walter Blum, Helmut Rechenberg, and Hans-Peter Dürr, editors, *Original Scientific Papers Wissenschaftliche Originalarbeiten*, pages 580–597. Springer Berlin Heidelberg, Berlin, Heidelberg, 1985.

[39] S Chikazumi and C D Graham. Physics of ferromagnetism 2e. 2009.

[40] Eberhard Engel and Reiner M Dreizler. *Density Functional Theory: An Advanced Course*. Springer, Berlin, Heidelberg, 2011.

[41] O. N. Mryasov, U. Nowak, K. Y. Guslienko, and R. W. Chantrell. Temperature-dependent magnetic properties of fept: Effective spin hamiltonian model. *EPL (Europhysics Letters)*, 69:805–811, mar 2005.

[42] David J Griffiths. Introduction to electrodynamics. *Am. J. Phys.*, 73(6):574–574, June 2005.

[43] H W Babcock. Zeeman effect in stellar spectra. *Astrophys. J.*, 1947.

[44] G. Kresse and J. Furthmüller. Efficient iterative schemes for ab initio total-energy calculations using a plane-wave basis set. *Phys. Rev. B*, 54:11169–11186, Oct 1996.

[45] M D Segall, Philip J D Lindan, M J Probert, C J Pickard, P J Hasnip, S J Clark, and M C Payne. First-principles simulation: ideas, illustrations and the CASTEP code. *Journal of Physics: Condensed Matter*, 14(11):2717–2744, mar 2002.

[46] N. Kazantseva, D. Hinzke, U. Nowak, R. W. Chantrell, U. Atxitia, and O. Chubykalo-Fesenko. Towards multiscale modeling of magnetic materials: Simulations of fept. *Phys. Rev. B*, 77:184428, May 2008.

[47] E. Lifshits L.Landau. On the theory of the dispersion of magnetic permeability in ferromagnetic bodies. 1935.

[48] T. L. Gilbert. A phenomenological theory of damping in ferromagnetic materials. *IEEE Transactions on Magnetics*, 40(6):3443–3449, Nov 2004.

[49] Hannay J D. *Computational simulations of thermally activated magnetisation dynamics at high frequencies PhD Thesis*. 2001.

[50] William Fuller Brown Jr. Thermal fluctuations of fine ferromagnetic particles. 1979.

[51] José Luis García-Palacios and Francisco J. Lázaro. Langevin-dynamics study of the dynamical properties of small magnetic particles. *Phys. Rev. B*, 58:14937–14958, Dec 1998.

[52] Hannes Risken. *Fokker-Planck Equation*, pages 63–95. Springer Berlin Heidelberg, Berlin, Heidelberg, 1996.

[53] J H Mentink, M V Tretyakov, A Fasolino, M I Katsnelson, and Th Rasing. Stable and fast semi-implicit integration of the stochastic landau–lifshitz equation. *Journal of Physics: Condensed Matter*, 22(17):176001, apr 2010.

[54] M. O. A. Ellis, T. A. Ostler, and R. W. Chantrell. Classical spin model of the relaxation dynamics of rare-earth doped permalloy. *Phys. Rev. B*, 86:174418, Nov 2012.

[55] O. Bottauscio and A. Manzin. Efficiency of the geometric integration of landau–lifshitz–gilbert equation based on cayley transform. *IEEE Transactions on Magnetics*, 47(5):1154–1157, May 2011.

[56] D. A. Garanin. Self-consistent gaussian approximation for classical spin systems: Thermodynamics. *Phys. Rev. B*, 53:11593–11605, May 1996.

[57] Nicholas Metropolis and S. Ulam. The monte carlo method. *Journal of the American Statistical Association*, 44(247):335–341, 1949. PMID: 18139350.

[58] D. Hinzke and U. Nowak. Monte carlo simulation of magnetization switching in a heisenberg model for small ferromagnetic particles. *Computer Physics Communications*, 121-122:334 – 337, 1999. Proceedings of the Europhysics Conference on Computational Physics CCP 1998.

[59] Pierre Asselin, Richard Francis L Evans, Joe Barker, Roy W Chantrell, Rocio Yanes, Oksana Chubykalo-Fesenko, Denise Hinzke, and Ulrich Nowak. Constrained monte carlo method and calculation of the temperature dependence of magnetic anisotropy. *Physical Review B*, 82(5):054415, 2010.

[60] D. A. Garanin and H. Kachkachi. Surface contribution to the anisotropy of magnetic nanoparticles. *Phys. Rev. Lett.*, 90:065504, Feb 2003.

[61] S. Pisana, O. Mosendz, G. J. Parker, J. W. Reiner, T. S. Santos, A. T. McCallum, H. J. Richter, and D. Weller. Effects of grain microstructure on magnetic properties in feptag-c media for heat assisted magnetic recording. *Journal of Applied Physics*, 113(4):043910, 2013.

[62] C. L. Platt, K. W. Wierman, E. B. Svedberg, R. van de Veerdonk, J. K. Howard, A. G. Roy, and D. E. Laughlin. L–10 ordering and microstructure of fept thin films with cu, ag, and au additive. *Journal of Applied Physics*, 92(10):6104–6109, 2002.

[63] Y. Shao, M. L. Yan, and D. J. Sellmyer. Effects of rapid thermal annealing on nanostructure, texture and magnetic properties of granular fept:ag films for perpendicular recording (invited). *Journal of Applied Physics*, 93(10):8152–8154, 2003.

[64] V. M. Sokalski, J. Zhu, and D. E. Laughlin. Characterization of oxide materials for exchange decoupling in perpendicular thin film media. *IEEE Transactions on Magnetics*, 46(6):2260–2263, June 2010.

[65] P.J. van der Zaag, P.J.H. Bloemen, J.M. Gaines, R.M. Wolf, P.A.A. van der Heijden, R.J.M. van de Veerdonk, and W.J.M. de Jonge. On the construction of an fe3o4-based all-oxide spin valve. *Journal of Magnetism and Magnetic Materials*, 211(1):301 – 308, 2000.

[66] P. A. A. van der Heijden, P. J. H. Bloemen, J. M. Metselaar, R. M. Wolf, J. M. Gaines, J. T. W. M. van Eemeren, P. J. van der Zaag, and W. J. M. de Jonge. Interlayer coupling between fe$_3$o$_4$ layers separated by an insulating nonmagnetic mgo layer. *Phys. Rev. B*, 55:11569–11575, May 1997.

[67] C. L. Platt, M. R. McCartney, F. T. Parker, and A. E. Berkowitz. Magnetic interlayer coupling in ferromagnet/insulator/ferromagnet structures. *Phys. Rev. B*, 61:9633–9641, Apr 2000.

[68] J. C. Slonczewski. Conductance and exchange coupling of two ferromagnets separated by a tunneling barrier. *Phys. Rev. B*, 39:6995–7002, Apr 1989.

[69] S. D. Granz and M. H. Kryder. Intergranular exchange coupling in fept:x:fept ($x = b$, c,sio_x, cr andtao$_x$) thin films for heat assisted magnetic recording. *IEEE Transactions on Magnetics*, 48(11):2746–2748, Nov 2012.

[70] Efrem Y. Huang and Mark H. Kryder. Effects of temperature on intergranular exchange coupling in l10 fept thin films. *Journal of Applied Physics*, 115(21):213906, 2014.

[71] Y. Peng, X. W. Wu, J. Pressesky, G. P. Ju, W. Scholz, and R. W. Chantrell. Cluster size and exchange dispersion in perpendicular magnetic media. *Journal of Applied Physics*, 109(12):123907, 2011.

[72] Lewis J. Atkinson, Thomas A. Ostler, O. Hovorka, K. K. Wang, B. Lu, G. P. Ju, J. Hohlfeld, B. Bergman, B. Koopmans, and Roy W. Chantrell. Effects of interactions on the relaxation processes in magnetic nanostructures. *Phys. Rev. B*, 94:134431, Oct 2016.

[73] Amikam Aharoni and Richard Kronstein Professor of Theoretical Magnetism Amikam Aharoni. *Introduction to the Theory of Ferromagnetism*. Oxford University Press, 2000.

[74] M. Rührig, R. Schäfer, A. Hubert, R. Mosler, J. A. Wolf, S. Demokritov, and P. Grünberg. Domain observations on fe layered structures. evidence for a biquadratic coupling effect. *physica status solidi (a)*, 125(2):635–656, 6 1991.

[75] C.J. Gutierrez, J.J. Krebs, M.E. Filipkowski, and G.A. Prinz. Strong temperature dependence of the 90° coupling in fe/al/fe(001) magnetic trilayers. *Journal of Magnetism and Magnetic Materials*, 116(3):L305 – L310, 1992.

[76] J. C. Slonczewski. Fluctuation mechanism for biquadratic exchange coupling in magnetic multilayers. *Phys. Rev. Lett.*, 67:3172–3175, Nov 1991.

[77] J. C. Slonczewski. Origin of biquadratic exchange in magnetic multilayers (invited). *Journal of Applied Physics*, 73(10):5957–5962, 1993.

[78] R F L Evans, Q Coopman, S Devos, W J Fan, O Hovorka, and R W Chantrell. Atomistic calculation of the thickness and temperature dependence of exchange coupling through a dilute magnetic oxide. *Journal of Physics D: Applied Physics*, 47(50):502001, nov 2014.

[79] I. Tamai, R. Araki, and K. Tanahashi. Magnetic and recording characteristics of cocrpt-oxide media with a mixture of sio_2 and tio_2. *IEEE Transactions on Magnetics*, 44(11):3492–3495, Nov 2008.

[80] Kenneth E. Johnson. Magnetic materials and structures for thin-film recording media (invited). *Journal of Applied Physics*, 87(9):5365–5370, 2000.

[81] H.J. Richter and A.Yu. Dobin. Angle effects at high-density magnetic recording. *Journal of Magnetism and Magnetic Materials*, 287:41 – 50, 2005. Selected papers from the seventh Perpendicular Magnetic Recording Conference (PMRC 2004).

[82] R. H. Victora and Xiao Shen. Composite media for perpendicular magnetic recording. *IEEE Transactions on Magnetics*, 41(2):537–542, Feb 2005.

[83] R. E. MacDonald and J. W. Beck. Magneto-optical recording. *Journal of Applied Physics*, 40(3):1429–1435, 1969.

[84] S.J. Greaves, H. Muraoka, and Y. Kanai. Simulations of recording media for 1tb/in2. *Journal of Magnetism and Magnetic Materials*, 320(22):2889 – 2893, 2008. Eighth Perpendicular Magnetic Recording Conference.

[85] D Suess, C Vogler, C Abert, F Bruckner, R Windl, L Breth, and J Fidler. Fundamental limits in heat-assisted magnetic recording and methods to overcome it with exchange spring structures. *J. Appl. Phys.*, 117(16):163913, April 2015.

[86] HJ Richter, Andreas Lyberatos, Ulrich Nowak, Richard Francis L Evans, and Roy W Chantrell. The thermodynamic limits of magnetic recording. *Journal of Applied Physics*, 111(3):033909, 2012.

[87] D Suess and T Schrefl. Breaking the thermally induced write error in heat assisted recording by using low and high tc materials. *Appl. Phys. Lett.*, 102(16):162405, April 2013.

[88] E F Kneller and R Hawig. The exchange-spring magnet: a new material principle for permanent magnets. *IEEE Trans. Magn.*, 27(4):3588–3560, July 1991.

[89] O. Hellwig, J. B. Kortright, K. Takano, and Eric E. Fullerton. Switching behavior of fe-pt/ni-fe exchange-spring films studied by resonant soft-x-ray magneto-optical kerr effect. *Phys. Rev. B*, 62:11694–11698, Nov 2000.

[90] Jan-Ulrich Thiele, Stefan Maat, and Eric E Fullerton. FeRh/FePt exchange spring films for thermally assisted magnetic recording media. *Appl. Phys. Lett.*, 82(17):2859–2861, April 2003.

[91] D. Suess, J. Lee, J. Fidler, and T. Schrefl. Exchange-coupled perpendicular media. *Journal of Magnetism and Magnetic Materials*, 321(6):545 – 554, 2009. Current Perspectives: Perpendicular Recording.

[92] C. J. Aas, P. J. Hasnip, R. Cuadrado, E. M. Plotnikova, L. Szunyogh, L. Udvardi, and R. W. Chantrell. Exchange coupling and magnetic anisotropy at fe/fept interfaces. *Phys. Rev. B*, 88:174409, Nov 2013.

[93] K. Barmak, J. Kim, D. C. Berry, K. W. Wierman, E. B. Svedberg, and J. K. Howard. Calorimetric studies of the a1 to l10 transformation in fept and related ternary alloy thin films. *Journal of Applied Physics*, 95(11):7486–7488, 2004.

[94] O N Mryasov, U Nowak, K Y Guslienko, and R W Chantrell. Temperature-dependent magnetic properties of FePt: Effective spin hamiltonian model. *EPL*, 69(5):805, February 2005.

[95] D Weller and A Moser. Thermal effect limits in ultrahigh-density magnetic recording. *IEEE Trans. Magn.*, 35(6):4423–4439, November 1999.

[96] Earl Callen and Herbert Callen. Ferromagnetic transitions and the one-third-power law. *Journal of Applied Physics*, 36(3):1140–1142, 1965.

[97] M. D. Kuz'min. Shape of temperature dependence of spontaneous magnetization of ferromagnets: Quantitative analysis. *Phys. Rev. Lett.*, 94:107204, Mar 2005.

[98] Yasushi Endo, Osamu Kitakami, Satoshi Okamoto, and Yutaka Shimada. Determination of first and second magnetic anisotropy constants of magnetic recording media. *Applied Physics Letters*, 77(11):1689–1691, 2000.

[99] C Tannous and J Gieraltowski. The Stoner–Wohlfarth model of ferromagnetism. *Eur. J. Phys.*, 29(3):475, March 2008.

[100] D. Hinzke, N. Kazantseva, U. Nowak, O. N. Mryasov, P. Asselin, and R. W. Chantrell. Domain wall properties of fept: From bloch to linear walls. *Phys. Rev. B*, 77:094407, Mar 2008.

[101] N. Kazantseva, R. Wieser, and U. Nowak. Transition to linear domain walls in nanoconstrictions. *Phys. Rev. Lett.*, 94:037206, Jan 2005.

[102] R F L Evans, Q Coopman, S Devos, W J Fan, O Hovorka, and R W Chantrell. Atomistic calculation of the thickness and temperature dependence of exchange

coupling through a dilute magnetic oxide. *Journal of Physics D: Applied Physics*, 47(50):502001, 2014.

[103] H Kronmüller and D Goll. Micromagnetic theory of the pinning of domain walls at phase boundaries. *Physica B: Condensed Matter*, 319(1):122 – 126, 2002.

[104] D. Suess. Multilayer exchange spring media for magnetic recording. *Applied Physics Letters*, 89(11):113105, 2006.

[105] D. Hinzke, N. Kazantseva, U. Nowak, O. N. Mryasov, P. Asselin, and R. W. Chantrell. Domain wall properties of fept: From bloch to linear walls. *Phys. Rev. B*, 77:094407, Mar 2008.

[106] D. Goll and A. Breitling. Coercivity of ledge-type l10-fept/fe nanocomposites with perpendicular magnetization. *Applied Physics Letters*, 94(5):052502, 2009.

[107] Liwang "Liu, Wei Sheng, Jianmin Bai, Jiangwei Cao, Yuanfu Lou, Ying Wang, Fulin Wei, and Jia" Lu. "magnetic properties and magnetization reversal process of L10 FePt/Fe bilayers magnetic thin films". *"Appl. Surf. Sci."*, 258(20):"8124–8127", aug 2012.

[108] Y Liu and D J Sellmyer. Exchange-coupling behavior in nanostructured FePt/Fe bilayer films. *AIP Adv.*, 6(5):056010, May 2016.

[109] D. Makarov, J. Lee, C. Brombacher, C. Schubert, M. Fuger, D. Suess, J. Fidler, and M. Albrecht. Perpendicular fept-based exchange-coupled composite media. *Applied Physics Letters*, 96(6):062501, 2010.

[110] L.S. Huang, J.F. Hu, and J.S. Chen. Critical fe thickness for effective coercivity reduction in fept/fe exchange-coupled bilayer. *Journal of Magnetism and Magnetic Materials*, 324(6):1242 – 1247, 2012.

[111] Ryoichi Kikuchi. On the minimum of magnetization reversal time. *Journal of Applied Physics*, 27(11):1352–1357, 1956.

[112] J. Barker, R. F. L. Evans, R. W. Chantrell, D. Hinzke, and U. Nowak. Atomistic spin model simulation of magnetic reversal modes near the curie point. *Applied Physics Letters*, 97(19):192504, 2010.

[113] Christoph Vogler, Claas Abert, Florian Bruckner, Dieter Suess, and Dirk Praetorius. Areal density optimizations for heat-assisted magnetic recording of high-density media. *Journal of Applied Physics*, 119(22):223903, 2016.

[114] J. Becker, O. Mosendz, D. Weller, A. Kirilyuk, J. C. Maan, P. C. M. Christianen, Th. Rasing, and A. Kimel. Laser induced spin precession in highly anisotropic granular l10 fept. *Applied Physics Letters*, 104(15):152412, 2014.

[115] G. Woltersdorf, M. Kiessling, G. Meyer, J.-U. Thiele, and C. H. Back. Damping by slow relaxing rare earth impurities in $\mathrm{ni}_{80}\mathrm{fe}_{20}$. *Phys. Rev. Lett.*, 102:257602, Jun 2009.

[116] Christoph Vogler, Claas Abert, Florian Bruckner, and Dieter Suess. Landau-lifshitz-bloch equation for exchange-coupled grains. *Phys. Rev. B*, 90:214431, Dec 2014.

[117] Simon John Greaves, Hiroaki Muraoka, and Yasushi Kanai. Optimisation of applied field pulses for microwave assisted magnetic recording. *AIP Advances*, 7(5):056517, 2017.

[118] O. N. Mryasov, V. A. Gubanov, and A. I. Liechtenstein. Spiral-spin-density-wave states in fcc iron: Linear-muffin-tin-orbitals band-structure approach. *Phys. Rev. B*, 45:12330–12336, Jun 1992.

[119] Oleg N. Mryasov. Magnetic interactions in 3d–5d layered ferromagnets. *Journal of Magnetism and Magnetic Materials*, 272-276:800 – 801, 2004. Proceedings of the International Conference on Magnetism (ICM 2003).

[120] Stephen Blundell. *Magnetism in Condensed Matter*. Oxford University Press, 2001.

[121] P. Bruno and C. Chappert. Oscillatory coupling between ferromagnetic layers separated by a nonmagnetic metal spacer. *Phys. Rev. Lett.*, 67:1602–1605, Sep 1991.

[122] M. A. Ruderman and C. Kittel. Indirect exchange coupling of nuclear magnetic moments by conduction electrons. *Phys. Rev.*, 96:99–102, Oct 1954.

[123] Michael E. Fisher and Michael N. Barber. Scaling theory for finite-size effects in the critical region. *Phys. Rev. Lett.*, 28:1516–1519, Jun 1972.

[124] F. Huang, G. J. Mankey, M. T. Kief, and R. F. Willis. Finite-size scaling behavior of ferromagnetic thin films. *Journal of Applied Physics*, 73(10):6760–6762, 1993.

[125] O. Hovorka, S. Devos, Q. Coopman, W. J. Fan, C. J. Aas, R. F. L. Evans, Xi Chen, G. Ju, and R. W. Chantrell. The curie temperature distribution of fept granular magnetic recording media. *Applied Physics Letters*, 101(5):052406, 2012.

[126] C.-b. Rong, D. Li, V. Nandwana, N. Poudyal, Y. Ding, Z.L. Wang, H. Zeng, and J.P. Liu. Size-dependent chemical and magnetic ordering in l10-fept nanoparticles. *Advanced Materials*, 18(22):2984–2988, 11 2006.

[127] Jonathon Waters, Denis Kramer, Timothy J Sluckin, and Ondrej Hovorka. Resolving anomalies in the critical exponents of FePt using finite-size scaling in magnetic fields. October 2018.

[128] Earl R. Callen and Herbert B. Callen. Static magnetoelastic coupling in cubic crystals. *Phys. Rev.*, 129:578–593, Jan 1963.

[129] Jiao-Ming Qiu and Jian-Ping Wang. Monodispersed and highly ordered l10 fept nanoparticles prepared in the gas phase. *Applied Physics Letters*, 88(19):192505, 2006.

[130] D. S. Chuang, C. A. Ballentine, and R. C. O'Handley. Surface and step magnetic anisotropy. *Phys. Rev. B*, 49:15084–15095, Jun 1994.

[131] A. Enders, D. Peterka, D. Repetto, N. Lin, A. Dmitriev, and K. Kern. Temperature dependence of the surface anisotropy of fe ultrathin films on cu(001). *Phys. Rev. Lett.*, 90:217203, May 2003.

[132] S. Okamoto, N. Kikuchi, O. Kitakami, T. Miyazaki, Y. Shimada, and K. Fukamichi. Chemical-order-dependent magnetic anisotropy and exchange stiffness constant of fept (001) epitaxial films. *Phys. Rev. B*, 66:024413, Jul 2002.

Appendix A

Landau-Lifshitz-Gilbert equation

For an electron precessing around the nucleu with a radius r_0 and an angular speed ω, the kinetic moment can be written as $|\vec{L}| = m_0 \omega r_0^2$. Also, the motion of the electron around the nucleu produces an electrical current having the intensity equal to νe, where ν is the frequency and e is elementary electrical charge. According to electromagnetism theory, a loop current creates a magnetic moment following next formula:

$$|\vec{M}| = |I\vec{S}| = e\nu\pi r_0^2 = \frac{e\omega r_0^2}{2} = \frac{e}{2m_0}L \tag{A.1}$$

In a general form the equation 1 can be written as:

$$\vec{M} = -g\frac{e\omega r_0^2}{2} = \frac{e}{2m_0}\vec{L} = -\gamma\vec{L} \tag{A.2}$$

where γ is called gyromagnetic factor, having two values: 1 for orbital momentum and 2 for spin. In Electrodynamics the variation of kinetic momentum of the electrical charge in time it is described by the theory of variation of kinetic momentum:

$$\vec{\Gamma} = \frac{d\vec{L}}{dt} \tag{A.3}$$

where Γ is the torque. This one can be expressed like:

$$\vec{\Gamma} = \vec{M} \times \vec{B} \tag{A.4}$$

$\vec{B}$ is the magnetic field. For simplicity, we introduce a new notation for the direction of the magnetic moment $\vec{S}$, which is equal to $\vec{S} = \frac{\vec{M}}{|\vec{M}|}$. Therefore, equation (3) can be written as:

$$\frac{d\vec{S}}{dt} = -\gamma\left(\vec{S}\times\vec{B}\right) \tag{A.5}$$

Experimental measurements reveal a damping magnetic field which is proportional with the variation of the direction of magnetisation, being always opposite to the magnetic field.

$$\vec{B}_f = -\alpha\frac{d\vec{S}}{dt} \tag{A.6}$$

α coefficient is called Gilbert damping. Introducing the damping magnetic field in equation (6), we get the first form of LLG equation which describes the variation in time of the direction of magnetisation:

$$\frac{d\vec{S}}{dt} = -\gamma\left[\vec{S}\times\left(\vec{B}-\alpha\frac{d\vec{S}}{dt}\right)\right] \tag{A.7}$$

Taking into account equation (A.6), in the the equation (A.5), we obtain:

$$\vec{S}\times\frac{d\vec{S}}{dt} = -\vec{S}\times\left(\vec{S}\times\vec{B}\right)+\gamma\alpha\left[\vec{S}\times\left(\vec{S}\times\frac{d\vec{S}}{dt}\right)\right] \tag{A.8}$$

$$\vec{S}\times\frac{d\vec{S}}{dt} = -\vec{S}\times\left(\vec{S}\times\vec{B}\right)+\gamma\alpha\left[\vec{S}\left(\vec{S}\cdot\frac{d\vec{S}}{dt}-\vec{S}^2\frac{d\vec{S}}{dt}\right)\right] \tag{A.9}$$

Due to the magnitude of $\vec{S}$ is constant and $|\vec{S}|^2 = 1$, equation (A.9) becomes:

$$\frac{d\vec{S}}{dt} = -\frac{\gamma}{1+\gamma^2\alpha^2}\left(\vec{S}\times\vec{B}\right)-\frac{\gamma^2\alpha}{1+\gamma^2\alpha^2}\left[\vec{S}\times\left(\vec{S}\times\vec{B}\right)\right] \tag{A.10}$$

If $\lambda = \gamma\alpha$, then eq. (7) is:

$$\frac{d\vec{S}}{dt} = -\frac{\gamma}{1+\lambda^2}\left(\vec{S}\times\vec{B}\right)-\frac{\gamma\lambda}{1+\lambda^2}\left[\vec{S}\times\left(\vec{S}\times\vec{B}\right)\right] \tag{A.11}$$

Appendix B

The formalism of RKKY interaction

The paramagnetic susceptibility is a q-dependent which can be decomposed into a sum of all possible spatial frequencies:

$$\mathbf{H}(\mathbf{r}) = \delta(\mathbf{r})\mathbf{H} = \frac{1}{(2\pi)^3}\int \mathbf{H}_\mathbf{q} e^{i\mathbf{q}\cdot\mathbf{r}} d^3q \tag{B.1}$$

where $\mathbf{H}_\mathbf{q} = \mathbf{H}$. Thus delta function can be considered as a sum over all frequencies, comprising both very long wevelength and short wavelength oscillations. If $\chi_q = \chi$ is inependent of q, then $\mathbf{M}_\mathbf{q} = \chi\mathbf{H}$ and:

$$\mathbf{M} = \frac{1}{(2\pi)^3}\int \mathbf{M}_\mathbf{q} e^{i\mathbf{q}\cdot\mathbf{r}} d^3q = \chi\delta(\mathbf{r})\mathbf{H}, \tag{B.2}$$

The real space susceptibility is:

$$\begin{aligned}\chi(\mathbf{r}) &= \frac{1}{(2\pi)^3}\int d^3\mathbf{q}\chi_\mathbf{q} e^{i\mathbf{q}\cdot\mathbf{r}} \\ &= \frac{1}{(2\pi)^3}\int d^3\frac{\chi P}{2}\left(1+\frac{4k_f^2-q^2}{4k_f q}\log\frac{|q+2k_f|}{|q-2k_f|}\right)e^{i\mathbf{q}\cdot\mathbf{r}}\end{aligned} \tag{B.3}$$

The integral (B.3) is very hard to evaluate. First we need to show that:

$$\int d^3\mathbf{q}\chi_\mathbf{q} e^{i\mathbf{q}\cdot\mathbf{r}} = \frac{2\pi}{ir}\int_{-\infty}^{\infty} q e^{iqr}\phi(q)dq, \tag{B.4}$$

where $\phi(q) = \phi(-q)$ is a function of variable q. Hence equation (B.3) can be expanded as:

$$\frac{1}{(2\pi)^3}\int d^3\mathbf{q}\frac{\chi P}{2}\left(1+\frac{4k_f^2-q^2}{4k_f q}\log\frac{|q+2k_f|}{|q-2k_f|}\right)e^{i\mathbf{q}\cdot\mathbf{r}}$$
$$=\frac{\chi P k_f^2}{i\pi^2 r}\int_{-\infty}^{\infty}xe^{iyx}f(x)dx, \tag{B.5}$$

where $x=q/2k_f$, $y=2k_f r$ and $f(x)$ is:

$$f(x)=\frac{1}{2}\left(1+\frac{1-x^2}{2x}\log\frac{|x+1|}{|x-1|}\right) \tag{B.6}$$

If we consider following integrals:

$$I_1=\frac{1}{ir}\int_{-\infty}^{\infty}\frac{xe^{iyx}}{2}\left(1+\frac{1-x^2}{2x}\log\frac{|x+1|}{|x-1|}\right)dx$$
$$I_2=\frac{1}{ir}\int_{-\infty}^{\infty}\frac{xe^{iyx}}{2}\left(1+\frac{1-x^2}{2x}\log\frac{x+1}{x-1}\right)dx. \tag{B.7}$$

These to integrals are equated when $|x|>1$ Prove that I_2 is zero by completing the contour with an infinite semicircle in the upper half of the x plane and using Jordan's lemma . Therefore, using this result and a contour for I_1 that displaced infinitesimally above the real axis from $x=-1$ to $x=1$, show that:

$$I_1=\frac{1}{ir}\int_{-\infty}^{\infty}\frac{xe^{iyx}(1-x^2)}{4}\left(\log\frac{|x+1|}{|x-1|}-\log\frac{x+1}{x-1}\right)dx$$
$$=\frac{\pi}{r}\int_{-\infty}^{\infty}\frac{xe^{iyx}(1-x^2)}{4}$$
$$=\frac{\pi}{r}\left[\frac{\sin x-y\cos y}{y^3}\right] \tag{B.8}$$

At larger distance $k_f^{-1}\ll r$ equation (B.8) can be approximated with $\cos(2k_f r)/r^3$.